Development characterization and performance evaluation of thermoplastic-graphite based plate heat exchangers

Vom Fachbereich Maschinenbau und Verfahrenstechnik
der Rheinland-Pfälzischen Technischen Universität Kaiserslautern-Landau
zur Erlangung des akademischen Grades

Doktor-Ingenieur (Dr.-Ing.)

genehmigte

Dissertation

vorgelegt von

M.Sc. Hendrik Kiepfer
aus St. Ingbert

Dekan:	Prof. Dr. rer. nat. Roland Ulber
Prüfungskommission:	
Prüfungsvorsitzender:	Prof. Dr.-Ing. Erik von Harbou
1. Berichterstatter:	Prof. Dipl.-Ing. Dr. techn. Hans-Jörg Bart
2. Berichterstatter	Prof. Dipl.-Ing. Dr. techn. Matthäus Siebenhofer
Tag der mündlichen Prüfung:	13. Juli 2023

Kaiserslautern 2023

D386

Vorwort

Die vorliegende Dissertation entstand im Rahmen meiner Tätigkeit als wissenschaftlicher Mitarbeiter am Lehrstuhl für Thermische Verfahrenstechnik (ab 2021 Laboratory of Reaction and Fluid Process Engineering). Der Großteil dieser Arbeit ist das Ergebnis intensiver Forschung im Rahmen des IGF-Projekts mit dem Titel "Entwicklung von hochgefüllten dünnwandigen Kunststoffelementen mit verbesserten Wärmetransporteigenschaften im Korrosionsbereich" (Projektnummer: 20999 N). Dieses Projekt wurde durch die Arbeitsgemeinschaft industrieller Forschungsvereinigungen (AiF) im Rahmen des Programms zur Förderung der industriellen Gemeinschaftsforschung und -entwicklung (IGF) des Bundesministeriums für Wirtschaft und Klimaschutz gefördert.

Mein besonderer Dank gilt meinem Doktorvater, Herrn Prof. Dipl.-Ing. Dr. techn. Hans-Jörg Bart, für das spannende Forschungsthema, sowie die Bereitstellung der technischen und finanziellen Möglichkeiten. Insbesondere möchte ich mich bei ihm für die wissenschaftlichen Freiheiten und das entgegengebrachte Vertrauen bedanken. Beides hat dazu beigetragen diese Arbeit zu einem erfolgreichen Abschluss zu führen. Weiterhin möchte ich mich bei Herrn Prof. Dr.-Ing. Erik von Harbou für den Vorsitz der Promotionskommission und bei Herrn Prof. Dipl.-Ing. Dr. techn. Matthäus Siebenhofer für die Übernahme der Mitberichterstattung bedanken.

Zusätzlich möchte ich mich bei meinen Partnern am ZBT, allen voran Paul Stannek und Marco Grundler, bedanken, die durch ihre Expertise und engagierte Zusammenarbeit einen essentiellen Beitrag zu den Ergebnissen dieser Dissertation geleistet haben.

Ferner möchte ich mich bei allen Mitarbeiterinnen und Mitarbeitern des Lehrstuhls für Thermische Verfahrenstechnik bedanken, die mich während meiner Tätigkeit in vielfältiger Weise unterstützt haben. Ein Dank gebührt auch meinen wissenschaftlichen Hilfskräften, sowie allen Studierenden, die mir das Vertrauen entgegengebracht haben unter meiner Betreuung eine wissenschaftliche Arbeit anzufertigen. Ihre Mithilfe hat dazu beigetragen das dieser Dissertation zugrundeliegende Forschungsprojekt vollumfänglich zu bearbeiten.

Ein weiterer wichtiger Aspekt, den ich nicht unerwähnt lassen möchte, ist die entscheidende Rolle meiner Frau, die mich stets mental unterstützt hat, und mir half schwierige Phasen zu meistern. Mein herzlicher Dank geht ebenso an meine Schwiegereltern, die sich so häufig liebevoll um meine Tochter gekümmert haben, was mir die Möglichkeit gab, mich stärker auf die Ausfertigung dieser Arbeit zu konzentrieren. Schließlich möchte ich meinen Eltern meine aufrichtige Dankbarkeit aussprechen, deren kontinuierliche Unterstützung mir großen Rückhalt gab.

Diese Arbeit widme ich all jenen, die mich auf meinem wissenschaftlichen Weg begleitet und unterstützt haben.

Abstract

This thesis outlines the development of thermoplastic-graphite based plate heat exchangers from material screening to operation including performance evaluation and fouling investigations. Polypropylene and polyphenylene sulfide as matrix and graphite as filler were chosen as feedstock materials, as they possess a low density and excellent corrosion resistance at a comparatively low price.

For the purpose of material screening, custom-made polymer composite plates with a plate thickness of 1-2 mm and a filler content of up to 80 wt.% were investigated for their thermal and mechanical suitability with regard to their use in plate heat exchangers. Three-point flexural tests show that the loading of polypropylene with graphite leads to mechanical properties that allow the composites to be applied as corrugated heat exchanger plates. The simulated maximum overpressure is greater than 7 bar, depending on the wall thickness. The thermal conductivity of the composites was increased by a factor of 12.5 compared to pure polypropylene, resulting in thermal conductivities of up to 2.74 W/mK.

The fabrication of the developed corrugated heat exchanger plates, with a thickness between 0.85 mm and 2.5 mm and a heat transfer surface area of $11.13 \cdot 10^{-3}$ m² was carried out via processes that can be automized, namely extrusion and embossing. With the manufactured plate heat exchanger, overall heat transfer coefficients are determined over a wide range of operating conditions (Re = 200 - 1600), which are used to validate a plate heat exchanger model and consequently to compare the composites with conventional materials. The embossing, which seems to result in a shift of the internal graphite structure, leads to a further improvement of the thermal conductivity by 7-20 %, in addition to the impact of the filler. With low plate thicknesses, overall heat transfer coefficients of up to 1850 W/m²K could be obtained. Considering the low density of the manufactured thermal plates, this ensures comparable performance with metallic materials over a wide range of process conditions (Re = 200 - 4000).

The fouling kinetics and amount of calcium sulfate and calcium carbonate, respectively, on different polypropylene/graphite composites in a flat plate heat exchanger and the developed chevron type plate heat exchanger are determined and compared to the reference material stainless steel. For a straight evaluation of the fouling susceptibility of the materials the formation of bubbles on the materials is considered by optical imaging or excluded by a degasser. The results are interpreted using surface free energy and roughness of the surfaces. The results show that if bubble formation is avoided, the polymer composites have a very low fouling tendency compared to stainless steel, which is attributed to the low surface free energies of approximately

25 mN/m. This is particularly the case when turbulent flows are present, as is in plate heat exchangers or when sandblasted specimen are used. Sandblasting also continues to increase heat transfer compared to untreated samples by increasing thermal conductivity and creating local turbulences. Depending on the test conditions, the fouling resistance formed on the stainless steel surface is an order of magnitude greater than on the flat plate polymer composites. In addition, the fouling layers adhere only weakly to the composites, which indicates an easy cleaning in place after the formation of deposits. The fouling investigations in the plate heat exchanger reveal sensitivity to calcium sulfate fouling, however, CFD simulations indicate that this is due to flow maldistribution and not the actual polymer composite materials.

Kurzfassung

Diese Arbeit beschreibt die Entwicklung von Thermoplast-Graphit basierten Plattenwärmeübertragern von der Materialauswahl bis zum Betrieb, einschließlich Leistungsbewertung und Fouling-Untersuchungen. Als Ausgangsmaterialien wurden Polypropylen und Polyphenylensulfid als Matrix und Graphit als Füllstoff gewählt, da sie eine geringe Dichte und eine ausgezeichnete Korrosionsbeständigkeit zu einem vergleichsweise niedrigen Preis aufweisen.

Im Rahmen eines Materialscreenings wurden maßgeschneiderte Polymerkompositplatten mit einer Plattenstärke von 1-2 mm und einem Füllstoffgehalt von bis zu 80 Gew.-% auf ihre thermische und mechanische Eignung im Hinblick auf den Einsatz in Plattenwärmeübertragern untersucht. Drei-Punkt-Biegeversuche zeigen, dass die Beladung von Polypropylen mit Graphit zu mechanischen Eigenschaften führt, die den Einsatz der Komposite als strukturierte Wärmeübertragerplatten ermöglichen. Der simulierte maximale Überdruck liegt je nach Wanddicke bei über 7 bar. Die Wärmeleitfähigkeit der Verbundwerkstoffe konnte im Vergleich zu reinem Polypropylen um den Faktor 12,5 erhöht werden, was zu Wärmeleitfähigkeiten von bis zu 2,74 W/mK führt.

Die Herstellung der entwickelten strukturierten Wärmeübertragerplatten mit einer Dicke zwischen 0,85 mm und 2,5 mm und einer Wärmeübertragungsfläche von $11{,}13 \cdot 10^{-3}$ m² erfolgte mittels automatisierbarer Verfahren, nämlich Extrusion und Prägung. Mit dem hergestellten Plattenwärmeübertrager werden Wärmedurchgangskoeffizienten über einen weiten Bereich an Betriebsbedingungen (Re = 200 - 1600) bestimmt, die zur Validierung eines Plattenwärmeübertrager-Modells und folglich zum Vergleich der Kompositmaterialien mit herkömmlichen Materialien verwendet werden. Die Prägung, die zu einer Verschiebung der inneren Graphitstruktur führt, bewirkt eine weitere Verbesserung der Wärmeleitfähigkeit um 7-20 %, zusätzlich zu den positiven Auswirkungen des Füllstoffs. Bei geringen Plattenstärken konnten Wärmedurchgangskoeffizienten von bis zu 1850 W/m²K erzielt werden. In Anbetracht der geringen Dichte der hergestellten Wärmeübertragerplatten gewährleistet dies eine mit metallischen Werkstoffen vergleichbare Leistung über einen breiten Bereich an Prozessbedingungen (Re = 200 - 4000).

Die Foulingkinetik und die Menge an Calciumsulfat bzw. Calciumcarbonat auf verschiedenen Polypropylen/Graphit-Verbundwerkstoffen in einem Flachplattenwärmetauscher und dem entwickelten Plattenwärmeübertrager mit Chevronmuster wurden bestimmt und mit dem Referenzmaterial Edelstahl verglichen. Zur eindeutigen Bewertung der Foulinganfälligkeit der Materialien wird die Blasenbildung auf den Materialien durch optische Erfassung berücksichtigt

bzw. durch einen Entgaser ausgeschlossen. Die Ergebnisse werden mit Hilfe der freien Oberflächenenergie und der Rauheit der Oberflächen interpretiert. Die Ergebnisse zeigen, dass bei Vermeidung von Blasenbildung die Polymerkomposite im Vergleich zu Edelstahl eine sehr geringe Foulingneigung aufweisen, was u.a. auf die geringen freien Oberflächenenergien von ca. 25 mN/m zurückzuführen ist. Dies ist insbesondere dann der Fall, wenn turbulente Strömungen vorhanden sind, wie dies bei Plattenwärmetauschern der Fall ist, oder wenn sandgestrahlte Probekörper verwendet werden. Sandstrahlen erhöht zusätzlich den Wärmeübergang im Vergleich zu unbehandelten Proben, indem es die Wärmeleitfähigkeit erhöht und lokale Turbulenzen erzeugt. Je nach Prüfbedingungen ist der auf der Edelstahloberfläche gebildete Foulingwiderstand um eine Größenordnung höher als auf den ebenen Platten aus Polymerverbundwerkstoffen. Darüber hinaus haften die Foulingschichten nur schwach an den Verbundwerkstoffen, was auf eine leichte Reinigung nach der Bildung von Belägen hinweist. Die Fouling-Untersuchungen im Plattenwärmetauscher zeigen eine Anfälligkeit für Calciumsulfat-Fouling. CFD-Simulationen deuten jedoch darauf hin, dass dies auf eine Fehlverteilung der Strömung und nicht auf die eigentlichen Polymerverbundwerkstoffe zurückzuführen ist.

Table of Contents

Nomenclature

Latin symbols

Symbol	Description	Unit
A	Heat transfer surface	m
a	Corrugation amplitude	m
B	Bias uncertainty	
b	Molality	mol/kg
C	Heat capacity flow rate	W/K
D_e	Equivalent diameter	m
D_h	Hydraulic diameter	m
E	Elastic modulus	GPa
f	Fraction of projected area of solid surface wetted by liquid	-
h	Convective heat transfer coefficient	W/m²K
L	Heat exchanger length	m
$\dot{m}$	Mass flow rate	kg/s
N_{tp}	Number of thermal plates	-
Nu	Nusselt number	-
P	Corrugation pitch	m
p	Pressure	bar
Pr	Prandtl number	-
$\dot{Q}$	Heat transfer rate	W
$\dot{q}$	Heat flux	W/m²
r	Roughness ratio	-
r_f	Wet area roughness ratio	-
r_{xy}	Correlation coefficients	-
R	Thermal resistance	m²K/W
Re	Reynolds number	-
s	Wall thickness	m
s_p	Inter plate spacing	m
S_a	Mean arithmetic roughness	µm
t	Time	h
T	Temperature	°C
T_i	Temperature in channel i	°C
T_n	Temperature in channel n	°C

U	Overall heat transfer coefficient	W/m²K
w	Heat exchanger width	m
x, y, z	Rectangular coordinates	m
$y+$	Dimensionless wall distance	

Greek Symbols

Symbol	Description	Unit
α	Aspect ratio	-
β	Chevron angle	°
γ	Surface free energy	mN/m
γ_i	Surface free energy of species i	mN/m
ΔT_{lm}	Mean log temperature difference	K
ε	Strain	%, mm
λ	Thermal conductivity	W/mK
μ	Dynamic viscosity	Pa s
ϕ	Enlargement factor	-
σ	Stress	MPa
Θ	Contact angle	°

Subscripts

Symbol	Description
0	Initial conditions
1	Fluid stream 1
2	Fluid stream 2
b	Break
bub	Bubble
c	Cold
cr	Creep
CB	Cassie and Baxter
exp	Experiment
f	Fouled surface
flex	Flexural
h	Hot

i	General species designation
in	Inlet conditions
lv	Liquid-vapor
out	Outlet conditions
ref	Reference
sim	Simulation
sl	Solid-liquid
sv	Solid-vapor
tot	Total
w	Conditions at the wall
W	Wenzel
Y	Young

Superscripts

Symbol	**Description**
d	Disperse
p	Polar

Abbreviations

Symbol	**Description**
CA	Contact angle
CT	Computed tomography
cond	Conditioned
dg	Degassed
exp	Expanded graphite
HX1	Heat exchanger test cell 1
HX2	Heat exchanger test cell 2
im	Injection molded
OWRK	Owens Wendt Rabel and Kaelble method
PEEK	Polyether ether ketone
PE-RT	Polyethylene-raised temperature
PHE	Plate heat exchanger
PP	Polypropylene

PPS	Polyphenylene sulfide
PP-G	Polypropylene graphite-composite
PPS-G	Polyphenylene sulfide-graphite composite
RSME	Root mean square error
sb	Sandblasted
SEM	Scanning electron microscope
SS	Stainless steel
uc	Uncalendered

1 Introduction

Increasing the efficiency of industrial processes is an important element regarding the global climate targets. Particularly in the supply of industrial process heat, heat recovery on an industrial scale could be a key to increase efficiency. Especially critical are metal free processes or recovery measures from corrosive fluids, such as brines, sea water, flue gases, acids, bases, electroplating and pickling baths, as they occur in a wide range of industrial applications [1]. According to the state of the art heat exchangers made of expensive nonferrous and semi-precious metals or high-quality or high-priced stainless steels have to be used for these applications [2]. Alternatively, polymers that are insensitive to corrosive media can also be used in these fields of application. Due to their low thermal conductivity (less than 0.5 W/mK [3]), attempts are usually made to achieve a high degree of compactness (high heat transfer surface per volume) for polymer heat exchangers, e.g. by manufacturing hollow-fiber heat exchangers with the smallest possible wall thicknesses [4,5]. A compact heat exchanger design, mainly used for metals, are plate heat exchangers (PHEs) with patterned surfaces. The use PHEs compared to shell and tube heat exchangers has advantages as shown by many authors [6,7]. There is also a big footprint with regard to energy savings and CO_2 reduction. With PHEs, for example, higher heat recovery rates can be achieved at low temperature differences compared to tubular heat exchangers. In addition, due to the thin plates used, they have a lower weight than tubular heat exchangers, which is also associated with lower material and production costs. Especially in the environment of corrosive liquids, much energy can be saved, since corrosion-resistant alloys are associated with energy-intensive production and high material costs [8].

Furthermore, major savings could be achieved using materials whose fabrication is associated with a low-energy consumption, like polymers. As to that, the interest in polymer materials for heat exchanger applications has been driven by their high chemical stability and corrosion resistance [3]. For a broader application of polymers in heat transfer applications it is essential to increase the otherwise low thermal conductivity. But numerous authors have already shown that the production of polymeric composites can largely compensate for this disadvantage [9–12]. However, the examinations are mostly of a fundamental nature and focus often on thermal management in batteries, electronic and photovoltaic devices [10]. There are not many studies on polymer composites with respect to their use in heat exchangers and are mainly related to the production of polymer composite tubes for application in seawater desalination [13,14]. Studies of polymer composites for the application in PHEs are rare. However, graphite impregnated with synthetic resin is meanwhile used by manufacturers, such as SGL Carbon, to produce graphite heat exchangers under the DIABON® brand. Although they are corrosion resistant,

the high manufacturing and processing costs of these artificial graphite heat exchangers are a significant barrier to their widespread use. A cost effective innovative approach based on natural graphite sheets has recently been proposed by Jamzad et al. [15]. Although this approach also requires impregnation with resin and a realization of large heat exchangers with the presented technique seems to be unlikely.

The usual approach to exploit the corrosion resistance and low fouling susceptibility of polymers in the operation of PHEs is to coat inexpensive, well-conductive metallic plates, which can lead to considerable advantages over metallic surfaces in environments prone to fouling [16–18]. However, a thin polymer layer alone provides high thermal resistance, and the durability of the coatings can be a problem, as even minor damage to the coatings can lead to corrosive pitting [19]. To profitably combine the advantages of plate heat exchangers with those of polymers, the use of thermally conductive polymer composites is proposed and evaluated in this thesis. The extrusion of conductive thermoplastic-graphite composite sheets provides the basis to produce conductive thermal plates for plate heat exchangers, which can then be embossed with the desired pattern. To achieve the maximum possible heat transfer, the most widely used pattern, namely the chevron pattern, is used. This provides an increase in the effective heat transfer area, promotes swirl or vortex flows and the disruption and reattachment of boundary layers [20]. In terms of thermal performance, mechanical stability and manufacturing feasibility, the geometric design parameters of PHEs must be optimized. In particular, the parameters chevron angle (β), corrugation pitch (P) and corrugation amplitude (a) have a major influence on heat transfer and pressure drop.

In general, the heat transfer coefficient as well as the friction losses increases with increasing chevron angle β (0-90 °) as well as with the severity of corrugation waviness α (also called aspect ratio: $\alpha = 4a/P$) [21,22]. However, both values cannot be chosen arbitrarily. Regarding the polymer composites used, the presence of contact points is of great importance to ensure sufficient mechanical stability (necessary condition: $\beta < 90°$). Increasing aspect ratios ($\alpha > 0.5$), on the other hand, lead to an exponential increase in flow friction loss, with a simultaneous flattening of the thermal performance. In addition, there is a limit to the depth of the corrugations that can still be safely pressed and manufactured without compromising the structural integrity of the plates [20]. A limit that is probably even lower using polymer composites.

Based on the findings in the literature, a polymer composite plate heat exchanger was fabricated from polypropylene or polyphenylene sulfide and graphite particles as filler with an aspect ratio of 0.5 and a chevron angle of 60°. The selected manufacturing steps and raw materials ensure cost-effectiveness and mass production. The supplementation of the generated experimental

data with a model for the predictive calculation of the heat transfer should provide the basis for the effective use of the developed PHEs.

Chapter 2 highlights the fabrication of extruded thermoplastic-graphite composite plates with enhanced thermal conductivity and examines their suitability for use in corrugated PHEs. This includes the study of mechanical stability, thermal conductivity, and surface properties such as roughness and surface free energy. Based on the studies in Chapter 2, a polymer composite PHE could be developed, being addressed in Chapter 3. It presents the manufacturing process and evaluates the thermal performance of the developed PHE. Using the experimental data, a model for calculating the heat transfer could be validated, with the help of which the novel materials are compared with conventional materials. Since most heat exchangers are affected by fouling, which can lead to significant problems in heat exchanger operation [23], Chapter 4 presents studies on crystallization fouling on the developed polymer composites to evaluate their suitability in this type of heat exchanger with respect to fouling susceptibility. Besides the influence of different salt species and wall temperatures, the influence of air bubbles on the surface is also discussed as they strongly influence fouling processes. The Chapters 5 and 6 summarize the main findings of the present thesis regarding fundamental research and its industrial application and points out future perspectives.

2 Material Characterization

2.1 Theory

Various types of polymer heat exchangers are used in solar energy, air conditioning and refrigeration, automotive, computer, desalination, pharmaceutical, food, and energy recovery applications. Due to their resistance to fouling and corrosion, the use of polymers in some applications offers significant reductions in weight, cost, water consumption, volume, space requirements, and maintenance costs, which can make these heat exchangers more competitive with metallic heat exchangers in some applications. Due to their low thermal conductivity, polymers are generally not considered as a material for heat exchanger construction except for specific applications. Yet, by fabricating heat exchangers with very low wall thickness, both tubular and plate heat exchangers can achieve similar performance to their metallic alternative while being lighter in weight. However, the application range of such polymer heat exchangers can be extended through the fabrication of polymer matrix composites, giving polymer materials significant potential for the construction of heat exchangers in various applications [24]. An overview of the current research on polymer heat exchangers and thermally conductive polymer composites is given by Chen et al. [25] and Burger et al. [9], respectively. In the following, only a brief overview on the properties of polymer composite materials is given.

2.1.1 Thermally conductive polymer composites

The thermal conductivity of polymer composites is subject to various influencing factors, including the thermal conductivity of the polymer and the filler, as well as the volume fraction of the filler. However, the type, size and shape of the filler, the filler morphology, anisotropy (especially for non-spherical filler particles), adhesion between filler and matrix, properties of the filler-matrix interfaces and the effects of processing history also have a strong influence on the thermal conductivity of polymer composites [10]. Fig. 2.1 shows the relationship between the properties of polymer composites and the filler content, which contributes significantly to their thermal conductivity.

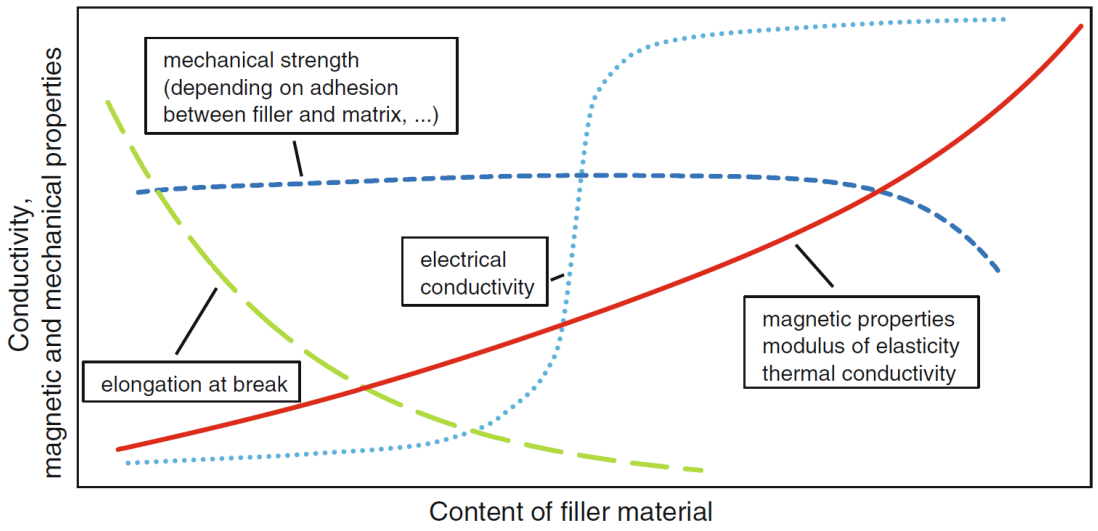

Fig. 2.1: Relationship between properties of polymer composites and filler content (based on Amesöder and Heinle [26,27]).

In general, the thermal conductivity of composites increases with the increase in the volume fraction of the thermally conductive filler, and high thermal conductivities can only be achieved at high filler contents because the formation of thermally conductive paths due to filler-filler bonding begins. However, if the filler content exceeds a certain level, the mechanical properties may decrease, e.g. due to embrittlement [10]. In addition, high filler loadings may cause manufacturing problems since the viscosity of the melt increases with filler content.

A wide variety of materials are available for both the underlying polymer matrix and the filler material used to improve thermal conductivity. For use in polymer composite heat exchangers, only thermoplastics are suitable, as they allow high filler contents and are ductile enough to satisfy the mechanical requirements in heat exchangers [13]. In addition, they allow alignment of the filler particles and mass production via manufacturing processes such as extrusion. Among the thermoplastics themselves, the selection regarding thermal, chemical, and mechanical requirements as well as specific requirements such as feasibility of manufacturing or wettability must be made. For example, commodity plastics such as polypropylene (PP), which can be used at temperatures up to 100 °C (long term), can be used for low requirements, and high-performance plastics such as polyether ether ketone (PEEK) or polyphenylene sulfide (PPS), which can withstand temperatures up to 250 °C, can be used for demanding applications [28].

For efficient use of polymer composites in heat exchangers, the filler must possess primarily high thermal conductivity. Thus, metallic, carbon-based and ceramic fillers can be considered. An overview of some common fillers is given by Chen et al [10]. Graphite has proved to be a popular filler because of its high thermal conductivity (100 - 400 W/mK), low cost, low density, good availability, and chemical inertness. However, due to its chemical structure (it forms

stacked layers of continuous hexagons) it has an anisotropic thermal conductivity, as shown schematically in Fig. 2.2. Thus, the thermal conductivity of the composite significantly depends on the orientation of the graphite particles in the matrix.

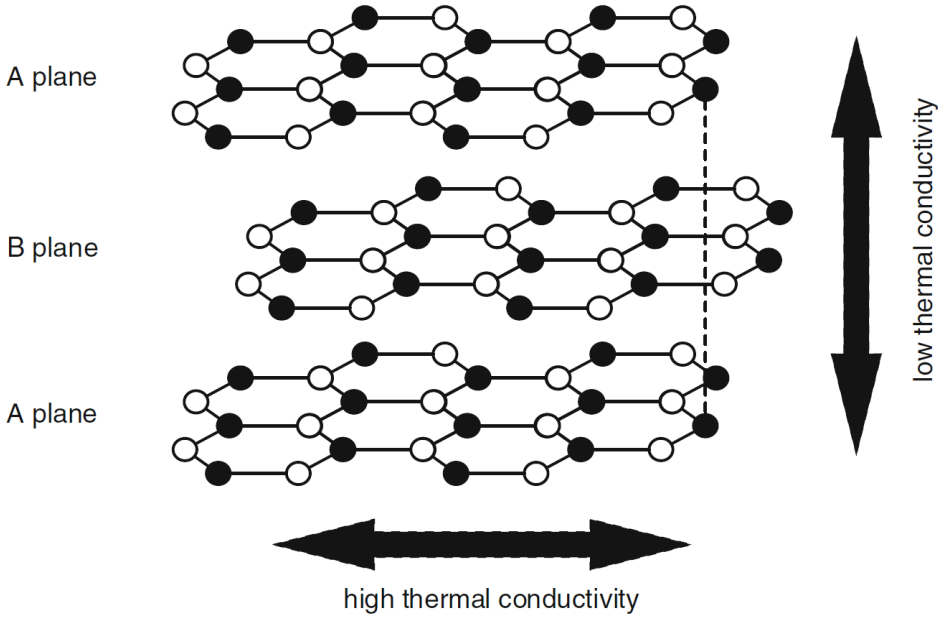

Fig. 2.2: Crystal structure of graphite (in accordance with Pierson [29]).

2.2 Materials and Methods

2.2.1 Materials and preparation

For the production of the heat exchanger components, highly filled graphite polymer compounds are prepared at the Zentrum für BrennstoffzellenTechnik (ZBT) GmbH (Duisburg) on a twin-screw or ring extruder. Subsequently, these compounds are further processed in a mill to a homogeneous granulate of < 4 mm. The compound pellets can then be transferred into a single-screw extruder which is the basis of the film extrusion line. There, the compounds melt again and pass through a wide slot die (width 250 mm) with variable gap dimensions to the calender, which smoothes the surface of the melt. The gap dimension of the calender can be variably adjusted between 0.2 mm and 25 mm. The resulting flat plates are used for the majority of the material characterizations. Only for the investigations of the bursting pressure, structured plates were used as well. Therefore, the composite plates were imprinted by means of a chevron die, with the corresponding embossing in a hot-pressing process. The embossing die applied is based on a chevron plate and is shown in Fig. 2.3. Both the embossing pressure and the embossing temperature were varied in this regard to evaluate the optimum properties.

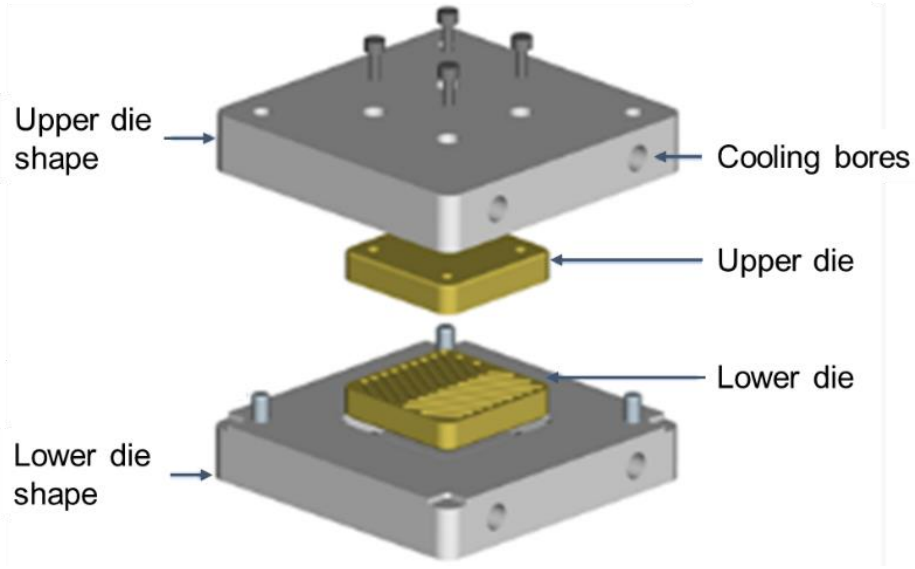

Fig. 2.3: Construction of the embossing tool.

In order to achieve the best possible properties of the manufactured materials with regard to their application in PHEs, all conceivable influencing factors were investigated and evaluated. In this context, the graphite content and the material thickness were investigated in addition to the polymer and graphite grades. The naming of the developed composites is composed as follows: polymer grade (e.g. C143) - filler content in wt.% (e.g. 75) - thickness in mm (if relevant) - additional characteristic of the material. The polymer grades used were mainly PP grades, but

also PPS grades were used in part. If important for understanding, the polymer grade behind the abbreviation is mentioned in the respective text passage. The additional characteristics are listed in Tab. 2.1 and are intended for further modification of the material properties. The complete naming may look like: C143-75-exp.

Tab. 2.1: Additional characteristics of the materials developed.

Description	Intention
Uncalendered plate (uc)	Influence on thermal conductivity
Sandblasted surface (sb)	Influence on thermal conductivity and modification of surface properties
Sample conditioned in water (cond)	Increase of wettability
Use of expanded graphite particles (exp)	Influence on thermal conductivity
Injection molded sample (im)	Influence on thermal conductivity
Particle size: small (s), medium (m) large (l)	Influence on thermal conductivity
Embossing pressure (*Numerical value* bar)	Influence on burst pressure

If the graphite grade is not specified, graphite with a D90 value of 45 µm (90 wt.% of the particles are smaller than 45 µm) is used. Moreover, the stainless steel AISI 316Ti (hereafter referred to as SS) as a standard material in corrosion resistant apparatus design is used as a comparative material. To ensure the reproducibility and comparability of the surface characterizations, a cleaning procedure is performed before the samples are examined. For this purpose, the sample is first cleaned with isopropanol, followed by demineralized water, and then dried with pressurized air. This procedure ensures that the surfaces can be measured free of fatty residues and particles.

2.2.2 Experimental methods

To develop a conceptual design of heat exchangers based on the investigated composite materials, a detailed knowledge of the material properties is required. These properties can basically be divided into three subareas: mechanical, thermal, and surface properties.

Mechanical characterization

Experimental stress tests were carried out to investigate the mechanical strength of the samples and consequently to be able to evaluate under which conditions mechanical failure occurs. These were supplemented with simulations to transfer the geometry for scale up and design of

PHEs. In addition, a permanent mechanical exposure (e.g., pressure), as it occurs in heat exchangers, can cause creeping of the material. To take this into account, tensile creeping tests are performed.

To evaluate the maximum mechanical strength and the elastic modulus of the materials, three-point flexural tests were performed according to ISO 178 under variation of the material thickness. The load applied to the specimens by this test method is more in line with the actual stress on the material in the PHE, which occurs not only along the tensile direction of the material. Therefore, this method was preferred over the classical tensile test. The three-point flexural test was complemented by a destructive pressure test, whose setup is shown schematically in Fig. 2.4.

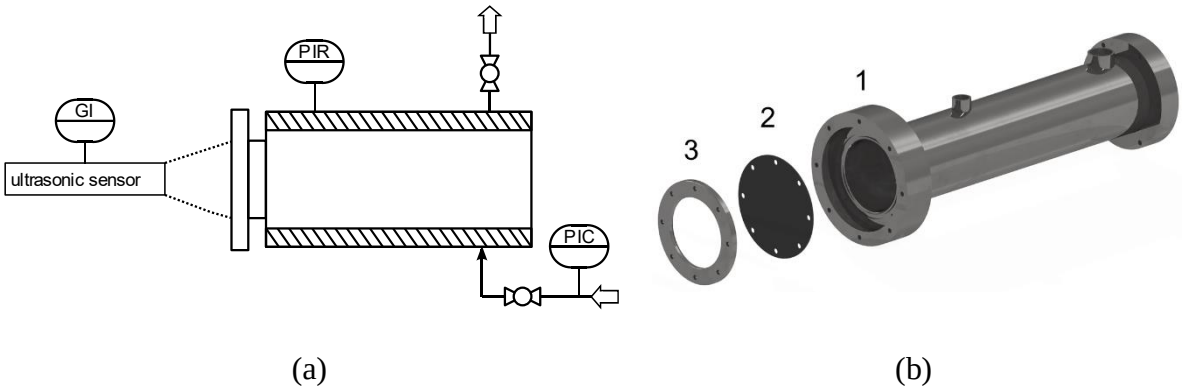

(a) (b)

Fig. 2.4: Pressure test set-up. (a) Schematic view. (b) Exploded view of the assembly.

The set-up consists of a pressure stable SS tube (1 in Fig. 2.4b) with an inner diameter of 70 mm into which a specimen (2) can be fixed by means of a clamping ring (3). The closed chamber is then flooded with water at ambient temperature and the pressure on the sample to be tested is gradually increased until it bursts. The pressure is continuously recorded with the pressure transducer FDA 602 L (Ahlborn GmbH; accuracy: 1 % of final value). The test setup also allows the sample expansion to be determined as a function of pressure using the ultrasonic sensor mic+25 (microsonic GmbH). For more reliable results, several specimens per material were tested.

With an apparatus for the determination of the creep behavior of polymers, shown in Fig. 2.5, creep tests were carried out with the pure polymers as well as selected polymer composites in a temperature-controlled water bath. The temperature selected was 80 °C, which corresponds to the requirement profile of the polypropylene composites. For this purpose, specimens according to DIN EN ISO 899 were provided by the ZBT. The measurement routine was also carried out according to the specifications of the standard mentioned. To ensure a constant tensile stress throughout the test, the specimens are loaded by constant force springs. To determine

the strain, two markings are made on the specimens, whose distance (L_0 = 100 mm) is measured with a caliper at predefined times. The specimens are conditioned for at least 24 hours without mechanical stress at the test conditions before starting the experiment to eliminate the influence of swelling (water absorption) and thermal expansion of the materials on the measurement result.

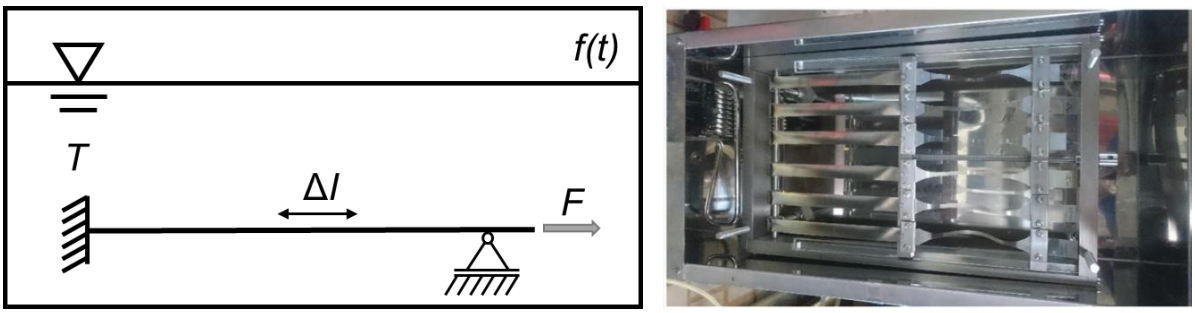

(a) (b)

Fig. 2.5: Test apparatus for the determination of creep strain. (a) Schematic. (b) Real view from above.

Surface characterization

The surface properties of materials have only a marginal influence on the performance of PHEs. However, they contribute significantly to fouling processes, which can greatly reduce the performance of heat exchangers during operation. For the interpretation and evaluation of the results of the fouling experiments, the knowledge of surface properties such as surface free energy and surface roughness is essential. Using the confocal microscope µsurf Explorer (Nanofocus AG) and the associated software, 3D surface profiles are monitored from which various roughness parameters can be extracted and quantified according to EN ISO 25178. The optical and thus non-invasive measuring device allows a very precise measurement of the sample surfaces. The measuring lenses used enable a resolution of the height values (z) of 20 nm or smaller and a resolution of the measured plane (x, y) of 3.1 µm. The mean arithmetic surface roughness S_a (Eq. 2.1) is used as a representative for the topographic 2D characterizations since it contains more information and though gives more significant results compared to a 1D line roughness parameter.

$$S_a = \frac{1}{A}\iint |z(x,y)|dxdy \tag{2.1}$$

In Eq. 2.1 A represents the measuring area z the ordinate.

Widely used approaches to calculate the surface free energy especially for polymer surfaces were published by Owens Wendt Rabel and Kaelble (OWRK method) and Wu (Wu method)

[30–33]. The calculations are based on Young's equation shown in Eq. 2.2, which describes the mechanical equilibrium of a droplet on an ideal surface [34].

$$\gamma_{\mathrm{lv}}\cos\theta = \gamma_{\mathrm{sv}} - \gamma_{\mathrm{sl}} \tag{2.2}$$

The contact angle is therefore dependent on the measurable liquid-vapor surface tension γ_{lv} and the non-measurable solid-liquid and solid-vapor surface tensions γ_{sl} and γ_{sv}, respectively. The latter can be substituted, for example, by use of the above-mentioned models. The surface tension γ_{sv} or surface free energy is thus determined by calculating the geometric mean (OWRK method, Eq. 2.3) or harmonic mean (WU method, Eq. 2.4) of the disperse ($\gamma_{\mathrm{sv}}^{\mathrm{d}}$) and polar ($\gamma_{\mathrm{sv}}^{\mathrm{p}}$) components of the surface free energy.

$$(1+\cos\theta)\gamma_{\mathrm{lv}} = 2\left(\sqrt{\gamma_{\mathrm{sv}}^{\mathrm{p}}\cdot\gamma_{\mathrm{lv}}^{\mathrm{p}}} + \sqrt{\gamma_{\mathrm{sv}}^{\mathrm{d}}\cdot\gamma_{\mathrm{lv}}^{\mathrm{d}}}\right) \tag{2.3}$$

$$(1+\cos\theta)\gamma_{\mathrm{lv}} = 4\left(\frac{\gamma_{\mathrm{sv}}^{\mathrm{p}}\cdot\gamma_{\mathrm{lv}}^{\mathrm{p}}}{\gamma_{\mathrm{sv}}^{\mathrm{p}}+\gamma_{\mathrm{lv}}^{\mathrm{p}}} + \frac{\gamma_{\mathrm{sv}}^{\mathrm{d}}\cdot\gamma_{\mathrm{lv}}^{\mathrm{d}}}{\gamma_{\mathrm{sv}}^{\mathrm{d}}+\gamma_{\mathrm{lv}}^{\mathrm{d}}}\right) \tag{2.4}$$

Whereby the total surface free energy results from the sum of the polar and disperse fractions according to Fowkes [35].

$$\gamma_{\mathrm{i}} = \gamma_{\mathrm{i}}^{\mathrm{p}} + \gamma_{\mathrm{i}}^{\mathrm{d}} \tag{2.5}$$

The methods mentioned require the knowledge of contact angles of at least two liquids with known polar and disperse fractions of surface tension on the sample investigated. To ensure a high accuracy of the determined surface free energies, static contact angle measurements with four reference liquids with different polarities (deionized water, ethylene glycol, dimethylsulfoxide and diiodomethane) were performed using the video-based optical contact angle measuring setup OCA 15 EC (Dataphysics Instruments GmbH). The left and right contact angles of at least 15 droplets are analyzed using the ellipse fitting method. Depending on the wetting liquid, the droplet volumes range from 4 to 14 µL. To ensure reproducibility, the contact angle measurements are performed at constant air temperature (20°C) and humidity (50% relative humidity).

The above equations are only valid for ideal surfaces (very low roughness), since the underlying Young's equation is only valid for this type of surface [36]. However, especially with very rough material surfaces, the apparent contact angle can differ greatly from the ideal Young contact angle. Pioneering work by Wenzel [37] and Cassie and Baxter [38] formulated the first

relationships linking the apparent contact angle to the Young contact angle. The authors' findings distinguish between homogeneous wetting (Wenzel) and heterogeneous wetting (Cassie and Baxter), illustrated in Fig. 2.6.

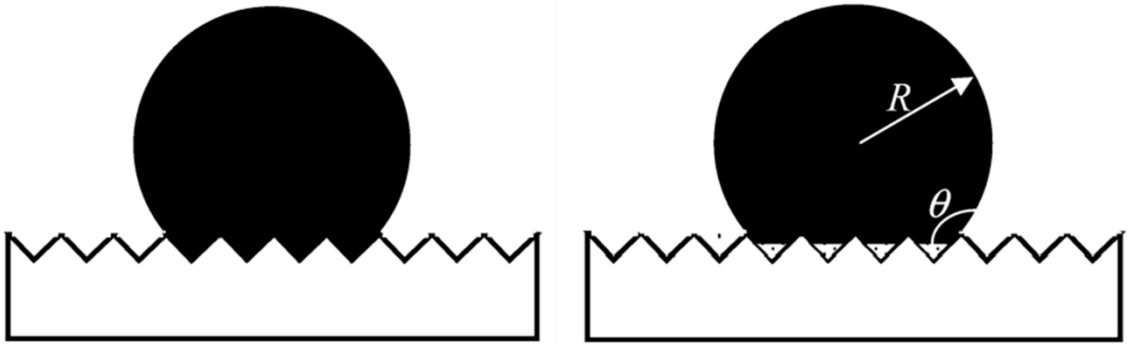

(a) (b)

Fig. 2.6: (a) Homogeneous wetting on a hydrophobic, rough surface. (b) Heterogeneous wetting on a hydrophobic, rough surface [39].

The following Wenzel equation refers to the homogeneous wetting and calculates the apparent Wenzel contact angle θ_W as a function of the Young contact angle θ_Y and roughness ratio r. Where the roughness ratio corresponds to the ratio of the actual area of the solid surface to its projected area.

$$\cos\theta_W = r\cos\theta_Y \tag{2.6}$$

For surfaces used in technical applications, the roughness factor is always greater than one. According to equation (2.6), it is therefore assumed that $\theta_W < \theta_Y$ for $\theta_Y < 90°$ and $\theta_W > \theta_Y$ for $\theta_Y > 90°$. Trends that could be confirmed experimentally [40,41]. The relationship according to Cassie and Baxter (heterogeneous wetting) includes, in addition to the roughness ratio for the wet area r_f, the parameter f, corresponding to the fraction of the projected area of the solid surface that is wetted by the liquid.

$$\cos\theta_{CB} = r_f f\cos\theta_Y + f - 1 \tag{2.7}$$

Determining which regime is explicit, however, is a sophisticated task. A detailed procedure is described by Marmur [39]. In addition, the procedure of droplet settling in the contact angle measurements can lead to a different wetting state than is the case in real condensation processes.

Thermal Characterization

The measurement of thermal diffusivity, through-plane thermal conductivity and specific heat capacity of the flat plate material was conducted on the Laser Flash Apparatus 457 (Netzsch). The sample to be analyzed is exposed to a laser flash from the bottom side and the time-dependent temperature increase on the opposite side is recorded by an infrared detector. By means of a mathematical model, the thermal diffusivity is determined, which, multiplied by the density and the specific heat capacity, results in the thermal conductivity. Using this measurement method, the specific heat capacity is determined by means of a comparative measurement with a reference of known thermal behavior, which sometimes leads to greater fluctuations in the determination of the heat capacity. Since this has a proportional effect on the calculated thermal conductivity, a theoretical approach was used to calculate the heat capacity and thus eliminate the uncertainty in the calculation of the thermal conductivity. The heat capacity of the composites is therefore calculated using a linear model based on the known heat capacities of the underlying raw materials.

2.2.3 Mechanical simulations

The pressure tests mentioned above are used to verify whether the flexural tests are representative enough to evaluate the stability of the materials in PHEs. However, mechanical simulations are needed to enable this. These provide the correlation between the maximum pressure (measured in the experiment) and maximum stress (determined by the simulations) leading to material failure. The mechanical simulations are therefore used, firstly, to determine the maximum stress in the material from the measured burst pressure. Secondly, they are used to simulate the stresses occurring in a PHE at a given pressure. Overall, it is thus possible to estimate how pressure-stable the developed materials are in a PHE.

Static simulations with Ansys Mechanical™ [42] were performed to evaluate the mechanical properties. Images used courtesy of ANSYS, Inc. The computational domain for the simulation of the burst pressure tests was taken over unchanged. For the simulation of the stresses in a PHE, the domain was considerably reduced compared to the original due to its size and complexity, as shown in Fig. 2.7. The developed plate heat exchanger, which is addressed in Chapter 3, served as the basis for the CFD simulations.

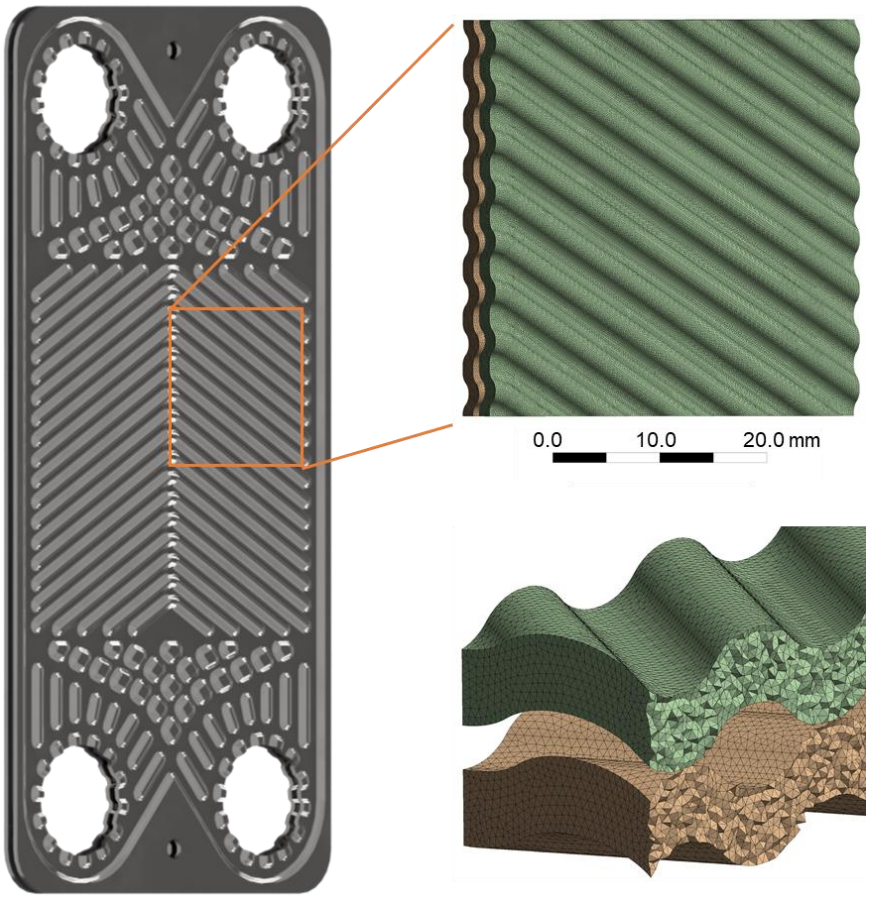

Fig. 2.7: Computational domain for the static simulation of the PHE. (l) Heat exchanger plate geometry. (r) PHE section and illustration of mesh and contact points in the PHE.

Already the reduced computational domain consists of at least 3.3 million elements, with a maximum element size of 0.2 mm. The mechanical simulation of a complete heat exchanger would require extreme computing resources. In contrast, experimental data would be preferable. A corrugated PHE with a chevron angle of 60° and a corrugation pitch of 4 mm was chosen as the model for the geometry. However, due to the symmetry of the structure, only a representative section was chosen (41 mm x 37 mm). This in turn requires two plates as domain. One serves as the end plate, which is assumed to be fixed in position. The other corresponds to an overflowed thermal plate, which can be loaded with a pressure (corresponding to a hydrodynamic pressure by the overflowing fluid). PP from the Ansys material library was selected as the material for the simulation, with the elastic modulus adjusted according to the three-point flexural tests carried out (see Fig. 2.8). For a worst-case scenario, the lowest measured elastic modulus was selected accordingly. The computational grids were created as unstructured grids due to the complexity of the PHE geometry. To achieve mesh independence, the maximum deformation of the materials in the simulation was set as a convergence criterion. The mesh is automatically and selectively refined by Ansys Mechanical until the convergence criterion is

reached. The simulations were considered to be convergent as soon as the deformation changes by less than 4 % in the iterative procedure.

2.3 Results and Discussion

2.3.1 Mechanical stability

Pure PP is not perfect suitable for use in PHEs because of its low thermal conductivity, acting as an insulator, but also because of its mechanical properties, like the high ductility (at least at temperatures above the glass transition temperature of max. 0 °C). The high elongation at break of at least 50 % [28,43] can cause a displacement and blocking of channels and consequently lead to flow maldistributions and a performance loss when operating PHEs in the presence of high pressure differences. However, due to its good mechanical (higher strength at lower densities compared to polyethylene) and thermal stability (up to 100 °C long term [43]) compared to other commodity plastics, it represents a sound and cost-effective polymer matrix for composite materials for heat exchangers. The production of composites based on PP and graphite not only increases the thermal conductivity, but also leads to an improvement in the mechanical properties, which makes the use in PHEs conceivable. Thus, as shown in Fig. 2.8, the E-modulus increases to at least 7.6 GPa, with a tendency for lower material thicknesses to result in higher elastic moduli. For comparison, pure PP has an E-modulus of approx. 1.5 GPa [43]. This increase in the elastic modulus is also accompanied by an extreme reduction in elongation at break. In the case of the composite shown in Fig. 2.8, the elongation at break is reduced to max. 0.97 %. Since the investigated materials are extruded, slightly different material properties are obtained in the extrusion and orthogonal to the extrusion direction. However, in Fig. 2.8 only the results orthogonally to the extrusion direction are shown, where material failure occurred more quickly.

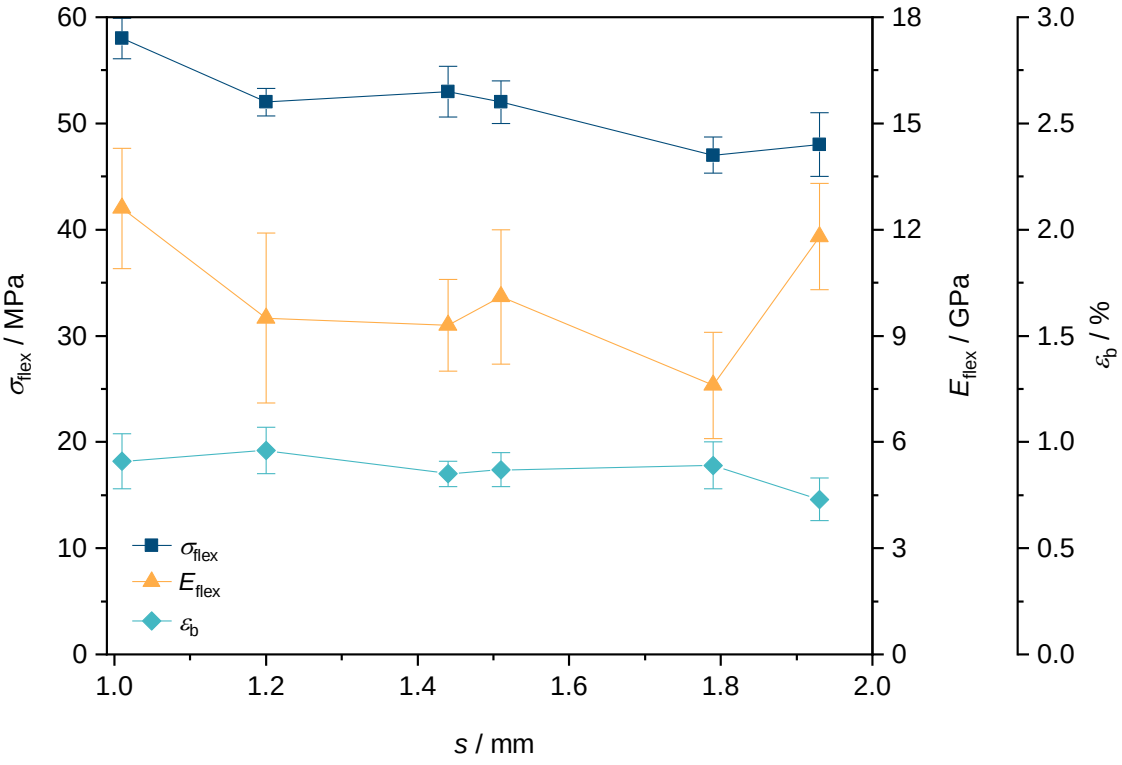

Fig. 2.8: Flexural modulus, flexural strength, and elongation at break as a function of the thickness of C143-75. Measurement orthogonally to the extrusion direction.

Distortion of the channels can thus be excluded when the materials investigated are used in PHEs, but mechanical failure during operation cannot. Compared to pure PP, the strength at break increases from 25-40 MPa [28] to 47-63 MPa, with thinner wall thicknesses also tending to provide higher values. If the plates are thinner extruded, the graphite particles become more stretched or aligned in the extrusion plane, which could lead to the observed better mechanical stability. Thinner wall thicknesses in the heat exchanger would in turn have a positive effect on its performance due to a lower thermal resistance. However, the small increase in flexural strength (known to be related to the cross-sectional area) is not sufficient to compensate for the advantage of larger wall thicknesses. This can be concluded from Fig. 2.9, showing the burst pressures measured in the pressure test set-up as a function of wall thickness for the same material (C143-75). Consequently, an increase in wall thickness leads to a linear increase in burst pressure. By doubling the wall thickness from 1 to 2 mm, the burst pressure can be increased from 1.3 to 3 bar for the test setup shown in Fig. 2.4.

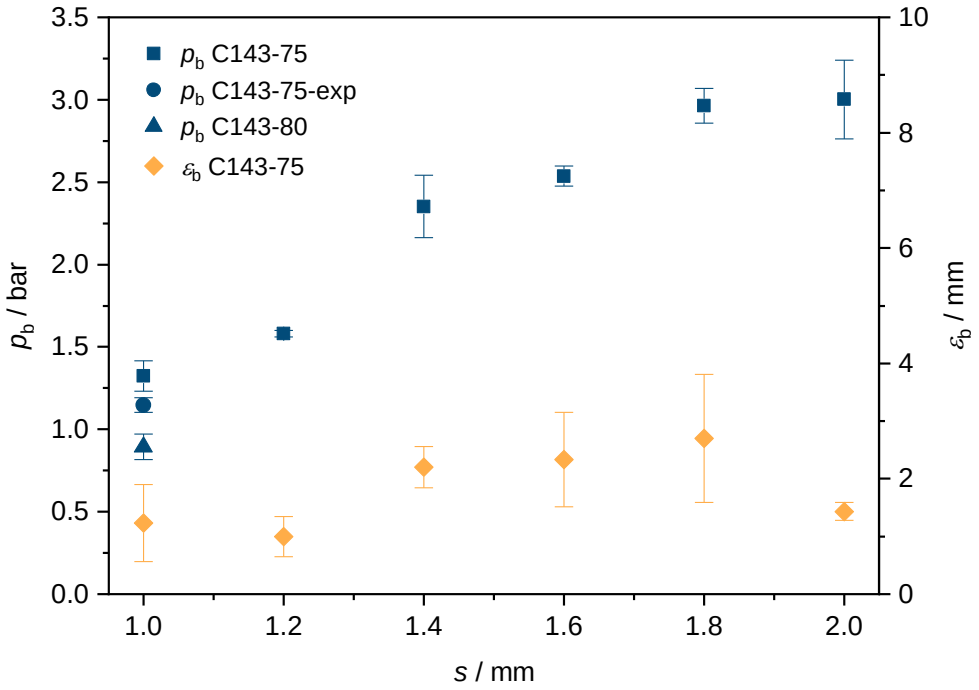

Fig. 2.9: Burst pressure and strain of unembossed composites as a function of thickness.

Furthermore, Fig. 2.9 shows the influence of a variation of the graphite content or graphite grade. It was observed that the mechanical stability of the composites increases up to a filling level of 75 wt.% but drops steeply thereafter. The same applies to the use of expanded graphite particles, although the influence appears to be lower here. In contrast, no significant differences can be observed for specimen expansion under load (also shown in Figure 2) across specimen thickness. The maximum strain ε_b leading to breakage is in the range 1-3 mm, although the large relative uncertainty does not allow a more detailed statement. Nevertheless, the expansions can be used to validate the mechanical simulations. A comparable result is obtained by examining the specimens embossed with the die shown in Fig. 2.3. The results of the burst pressure tests of the composite C143-80, embossed under different compression forces, are depicted in Fig. 2.10. Again, a linear behavior of the burst pressure with the wall thickness is shown, indicated by the dotted trend line. Comparison of measured data from specimens of the same thickness shows good agreement regardless of specimen embossing. The analysis of the data also shows that the embossing pressure and calendering carried out before embossing have no influence on the burst pressure. Regarding the burst pressure, the processing steps are therefore not decisive, but the wall thicknesses and filler grades used. In addition, the polymer matrix has a strong influence on the bursting pressure and thus the mechanical stability. Figure 2.7 shows two measuring points taken with PPS as the polymer. Compared to PP, PPS has an E-modulus that is about twice as large and a tensile strength that is about 50% higher [28]. Consequently, the two measurement points mentioned lie significantly above the regression line of

the PP composites. However, more detailed investigations regarding PPS composites proved to be difficult due to the demanding manufacturing process. This is due to the higher viscosity of the melt compared to the PP composites, which makes extrusion more difficult.

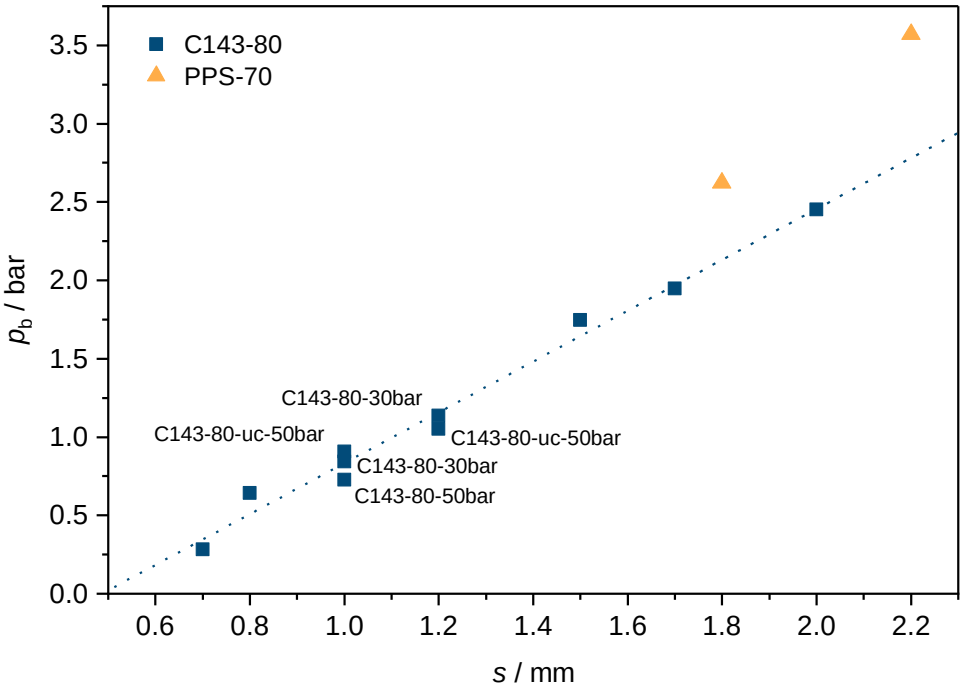

Fig. 2.10: Burst pressure of embossed composites as a function of thickness.

In order to verify whether the results of the three-point flexural test and the burst pressure test are consistent, simulations of the mechanical behavior were carried out. These provide a correlation between applied load and resulting mechanical stress in the material. For the final evaluation, a material failure theory suitable for the material must be used in the simulations. Since the materials are brittle (elongation at break less than 1%), the maximum principal stress is used as a criterion for material failure. The resulting maximum stresses in the material that lead to breakage of the specimens vary according to the simulations between 103 and 58 MPa. The results are therefore only partially within the range of the measurements of the three-point flexural tests (between 63 and 47 MPa). Here, the trend of greater strength at break with decreasing wall thickness is also much more pronounced. Thus, the specimens with 1 mm wall thickness broke on average at 103 MPa and with 2 mm wall thickness on average at 58 MPa. Nevertheless, the results of the three-point flexural test can be reliably used as a worst-case scenario for more realistic geometries, i.e. of a PHE section (see Fig. 2.11b and Fig. 2.13). Consequently, material failure is not expected before a maximum stress of 47 MPa or 55 MPa is reached, respectively. The case distinction refers to the lowest measured stress along (55 MPa) or orthogonal (47 MPa, see Fig. 2.8) to the extrusion direction. Fig. 2.11 shows that this criterion can be satisfied for a wide range of pressure loads, depending on the geometry. For a pressure

of 5 bar and a material thickness of 1 mm, the PHE would resist, whereas the specimen would have to fail in the burst pressure test already.

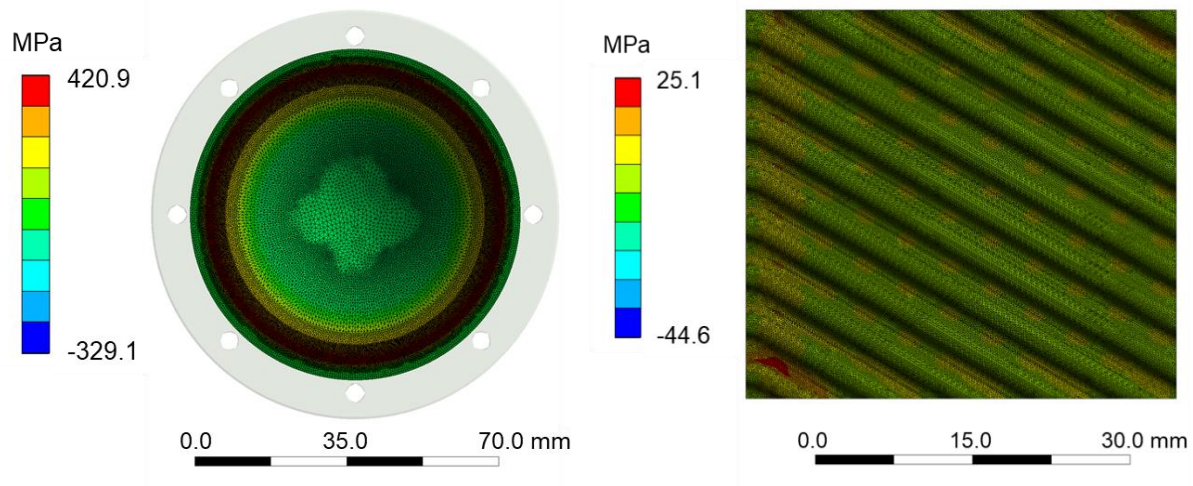

(a) (b)

Fig. 2.11: Computational domain and resulting stresses in the material at a load of 5 bar. (a) Pressure test set-up. (b) PHE section.

For a better understanding Fig. 2.12 shows the loadings that would lead to material failure as a function of the wall thickness and the case distinction made above. It is clear that the local geometry can lead a decisive contribution to the material stability in the final application. For example, the material under investigation should withstand pressures of more than 5 bar even at low wall thicknesses of 1 mm. The reason for this lies in the angled corrugations of PHEs. At minimum plate spacing, single wave peaks come into contact with each other. Contact points therefore occur, which lead to stabilization. This can also be seen in the visualization of the stresses in the material (Fig. 2.11). At the contact points, stronger loads occur in the material, which reduce the load on the surrounding areas. However, the strongest stresses in the material occur at the edges. The actual edges of the thermal plates, where the screw connections are located, are not explicitly considered here.

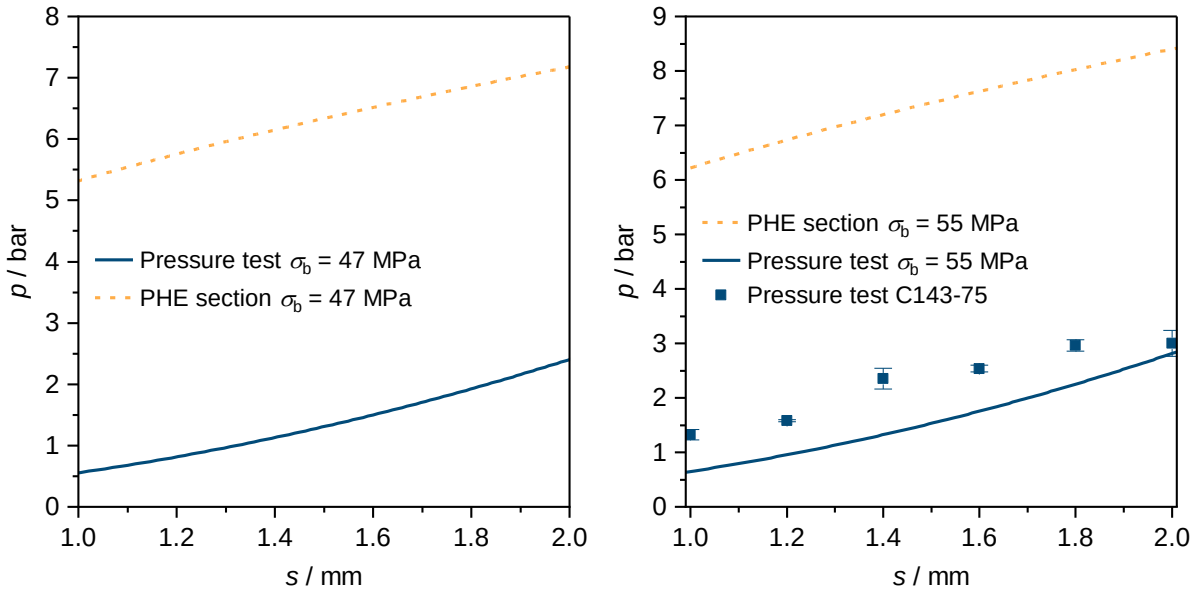

(a) (b)

Fig. 2.12: Simulated material failure loads for different material thicknesses and geometries.

On the other hand, the material could withstand even higher pressures in reality, since firstly a worst-case scenario is considered and secondly the maximum stresses in the material occur only in discrete elements of the computational grid and not over large areas. It is possible that the maximum stresses, which are locally limited to very small areas, are not sufficient for a material failure. The first statement is confirmed by considering Fig. 2.12b. This already takes into account the more positive scenario (σ_b = 55 MPa), and yet almost all the measurement points exceed the simulations. The reason for this is, as mentioned before, the higher mechanical strengths of the developed composites at low wall thicknesses. The second statement is confirmed by considering Fig. 2.13. Visualized is the zone of the domain where the highest stresses occur in the material. These are, especially in the case of minimum stress, limited to single elements, which, as already mentioned, have a maximum size of 0.2 mm. However, whether this locally strongly limited stress peak leads to material failure can only be confirmed experimentally.

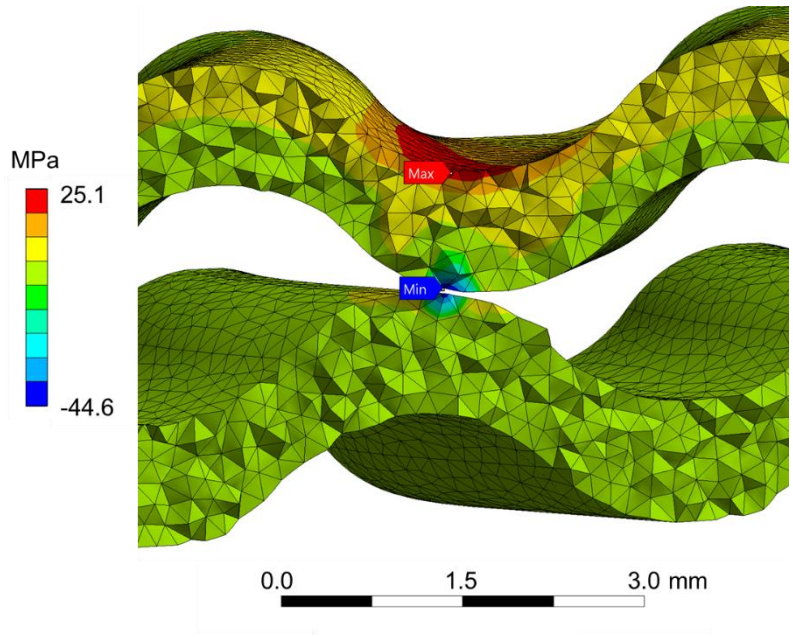

Fig. 2.13: Visualization of the minimum and maximum principal stress in the material.

In order to put this into a correct perspective it must be added that the simulations alone are not sufficient for the dimensioning of PHEs with the materials examined in this thesis. The first reason is that, as explained earlier, not the complete geometry was considered. In fact, a review of the literature shows that it is the inlet areas of plate heat exchangers (also called flow distributors) that are susceptible to material failure [44]. The second reason is that so far only experiments and simulations at ambient temperature were considered. However, polymers in particular have mechanical properties that are strongly dependent on temperature. At the temperature studied, for example, they may tend to brittle failure (fracture), but at higher temperatures they may tend to ductile failure (yield). In addition, many plate heat exchangers fail not by high loads alone but by creep or material fatigue [45,46].

The creep tests carried out, shown in Fig. 2.14, demonstrate that the material behavior of polymers is extremely dependent on the type of load and the temperature. As in the pressure tests, the mechanical stability of the materials decreases above a graphite loading of 75 wt.% (see Fig. 38). Thus, the composite C143-75 resists a tensile force of 12.3 MPa for one hundred times longer than the C143-80 loaded 5 % higher. Compared to the pure polymer (Fig. 2.14a), there is a slight improvement with respect to the resistance to a tensile force by loading with graphite, but a significant reduction in the elongation at break. This consequently more rigid material behavior is desirable with respect to the application in PHE as described previously. However, the elongation at break also appears to have increased greatly with temperature or continuous loading, confirming the statement made earlier.

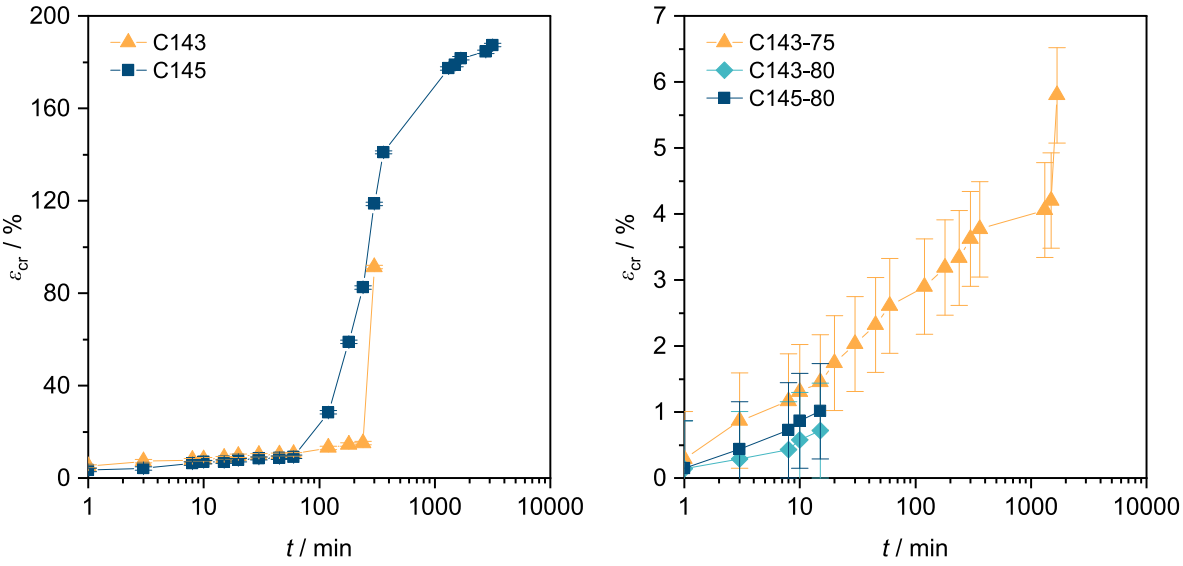

(a) (b)

Fig. 2.14: Creep behavior of the tested materials under a tensile load of 12.3 MPa. (a) Pure PP. (b) PP-graphite composites.

Overall, representative experiments with the PP-graphite composites over a wide range of operating conditions thus remain to be conducted. To provide a brief classification of the state of the art, the simulated worst-case material loads are used as a basis. Gasketed PHEs have a maximum operating pressure of 25 bar [20]. With wall thicknesses of 2 mm overpressures of over 7 bar could be realized. This would probably cover a significant number of applications. Of course, it should also be noted here that both process fluids usually flow into the heat exchanger at an overpressure. The highest relative pressure is therefore decisive.

2.3.2 Thermal conductivity

The thermal performance characteristics of a heat exchanger is usually indicated by the overall heat transfer coefficient *U* (see Eq. 4) or *UA*, the overall heat transfer coefficient multiplied by the heat exchanging surface. The thermal resistances limiting *U* are the convective heat transfer coefficients *h*, the wall thickness and thermal conductivity of the heat transferring wall. In a material comparison, mainly the latter is important. The wall thickness of thermal plates in PHEs is usually in the range of 0.4 and 1.2 mm [20] and cannot be arbitrarily adjusted, since otherwise the functionality and stability of the heat exchanger will be lost. As shown in the previous section, smaller wall thicknesses are not feasible with regard to PP-graphite PHEs. On the contrary, wall thicknesses are more likely to be in the upper application range. Pure PP is therefore completely excluded for use in PHEs, not only because of its mechanical properties. With the thermal conductivity of PP (see Fig. 2.15Fig. 2.15:), a wall thickness of 1.2 mm results

in maximum *U* values of 183 W/m²K. Similar values would be obtained with the other two polymers processed into composites, polyethylene (PE-RT) and polyphenylene sulfide (PPS). Metallic PHEs, in contrast, can achieve *U* values up to 7500 W/m²K [20]. However, the production of PP-graphite composites, which have been studied in particular, has increased the thermal conductivity of the materials up to about 1250 % (see Fig. 2.15).

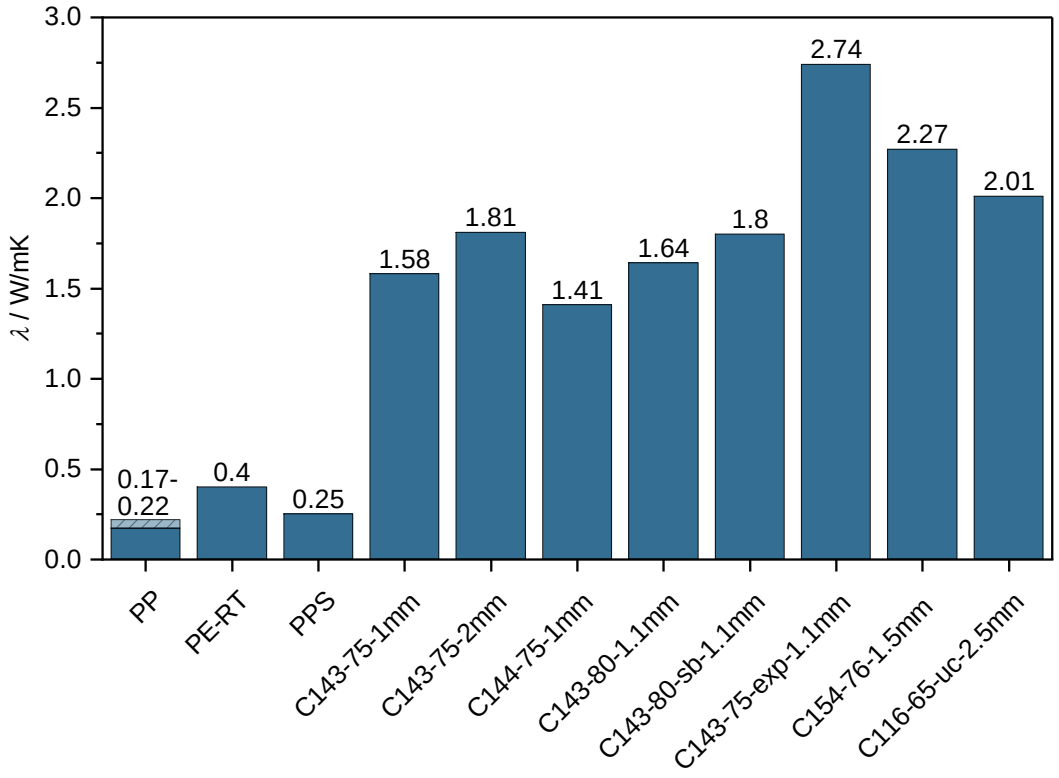

Fig. 2.15: Through-plane thermal conductivities of developed polymer-graphite composites and the pure polymers [43,47]. C143 and C144 correspond to PP types. C154 to PE-RT. C116 to PPS.

In addition to the thermal conductivities of the pure polymers, Fig. 2.15 shows the thermal conductivities of selected composites. It illustrates all manufacturing-relevant effects that lead to an improvement of the thermal conductivity. Here, the greatest effect on thermal conductivity is achieved by using expanded graphite particles. Further positive properties on the thermal conductivity of the composites produced are a higher wall thickness and an increase in the graphite content, whereby at 80 wt.% the manufacturing limits regarding the PP composites was almost reached. For the PPS composites (C116), a graphite mass fraction of 65% was already critical. Calendering was already impossible at this mass fraction. The PP grade used has only a very slight influence on the thermal conductivity of the composites, since the intrinsic thermal conductivities of the various PP grades differ only slightly. The use of different polymer types, on the other hand, partly has a stronger effect, depending on the differences in the thermal conductivity of the polymers. These appear to behave linearly with the thermal conductivity of

the composites, hence only small improvements can be achieved by polymer type adjustment. The use of PE-RT (C154) does lead to a significant improvement in thermal conductivity (due to the higher thermal conductivity of PE-RT compared to PP). However, it is not considered in the development of heat exchanger plates because of its poorer mechanical stability. The increase in thermal conductivity does not seem sufficient to compensate for the poorer mechanical stability.

Interesting non-self-explanatory results are the increase of thermal conductivity by sandblasting of the surfaces and by an increase in wall thickness, which is attributed to the manufacturing process. Due to the highly anisotropic thermal conductivity of graphite [29], the graphite-based composites are also anisotropic materials. Especially the through-plane thermal conductivity (i.e., the thermal conductivities perpendicular to the heat transfer surface) of the developed materials is crucial, since this significantly determines the heat flux in a heat exchanger. However, it could be shown by scanning electron microscope (SEM) images of sample cross sections (see Fig. 2.16:) that the graphite particles align themselves in plane through extrusion, which in turn leads to much higher thermal conductivities in plane compared to through plane. Consequently, the influence of the film thickness on the thermal conductivity can also be explained. The fillers align themselves within the melt in the slot die and are additionally stretched in the calender. The melt exits the die at variable thickness (approx. 1.8 mm) and high pressure (>100 bar), where wall friction causes initial alignment of the fillers. The melt is then processed in the calender to the adjustable target thickness of the film. The fillers in the melt are further oriented in the flow direction. As a result, they transfer their anisotropic thermal conductivity to the composite sample. Thereby, the degree of stretching or particle orientation depends on the manufactured wall thickness. The alignment of the filler particles is illustrated in Fig. 2.16: based on SEM images.

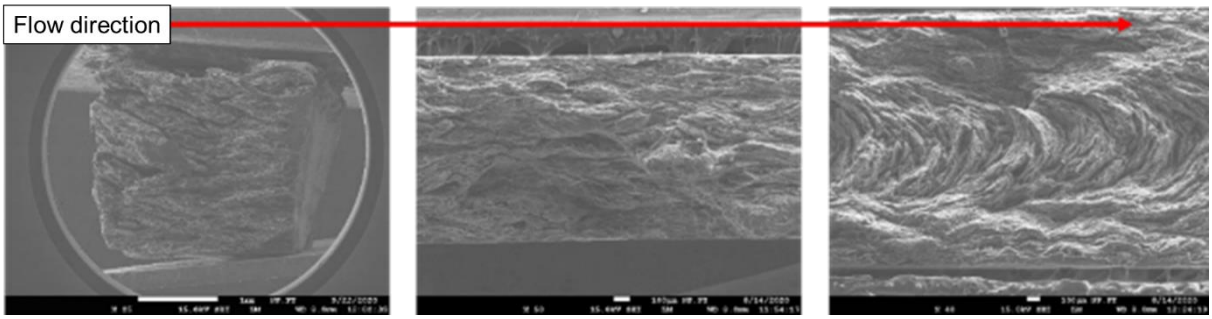

(a) (b) (c)

Fig. 2.16: Influence of the composite manufacturing method on particle alignment. (a) Uncalendered melt. (b) Calendered sample. (c) Injection molded sample.

Comparison of the SEM images shows that the fillers in the uncalandered and calendered film tend to be aligned in the flow direction over the entire thickness, although the alignment within the calendered film seems to be slightly more pronounced. The fillers in an injection molded specimen, on the other hand, are aligned almost orthogonally to the injection molding direction in the core. The orthogonal orientation of the filler particles favors the through plane thermal conductivity, which is confirmed by the determined thermal conductivities shown in Fig. 2.17. It can be seen that the injection molded samples have a factor of 6 higher through plane thermal conductivity than the extruded films of the same material. In addition, Fig. 2.17 shows, for further confirmation of the SEM images, the thermal conductivity of a sample that was measured through plane as well as in plane. As expected, the in plane thermal conductivity of the sample exceeds the through plane thermal conductivity by a multiple corresponding to the orientation of the graphite particles.

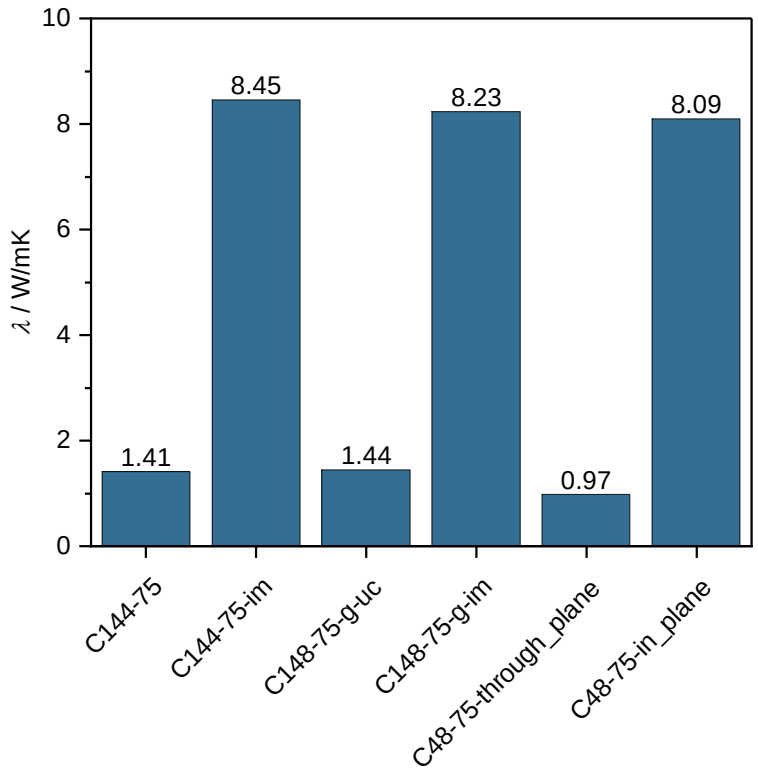

Fig. 2.17: Influence of manufacturing method and measurement plane on thermal conductivity.

Thus, it becomes apparent that the full potential of graphite as a filler has not been exploited. The low through plane thermal conductivities, inhibit the overall heat transfer rate in heat exchanger applications. Unfortunately, the particles cannot be oriented in plane by simple means. Approaches are the orientation of the diamagnetic graphite particles by means of strong magnetic fields [48], which, however, would negate the cost advantage of the otherwise inexpensive materials and production. Injection molding of materials also has its limitations. The feasible

size of heat transfer elements is the limiting factor when using this fabrication method. In addition, the production time is significantly longer since continuous production is not possible as with extrusion. Consequently, the focus remains on the extrusion of polymer composites. The evaluation of the thermal performance of the materials in the PHE application, i.e., taking all parameters into account, is given in Chapter 3. By sandblasting the surfaces, the thermal conductivity (through-plane) can in turn be easily increased by a factor of 10%. After manufacturing, the materials have a thin polymer layer on the surface, which has a lower thermal conductivity than the core. Sandblasting removes this layer, which increases the overall thermal conductivity as shown in Fig. 2.15.

2.3.3 Surface properties

The contact angle measurements were carried out with regard to the wettability of the materials and to evaluate the fouling susceptibility of the materials. In the case of single-phase heat transfer of two fluids, the wettability of the surfaces is negligible, whereas in the presence of a phase change it is not. Thus, the heat transfer in dropwise condensation (which can be achieved by superhydrophobic surfaces) is many times higher than in film condensation [49]. In the case of evaporation, on the other hand, surfaces with good wetting properties are preferred to produce a covering fill (film evaporation). The results of the static contact angle measurements are shown in compact form in Fig. 2.18. In addition to the static contact angles with water, the polar and disperse fractions of the surface free energy, calculated by the OWRK (Fig. 2.18) and the Wu method (Fig. 2.19) are shown, respectively.

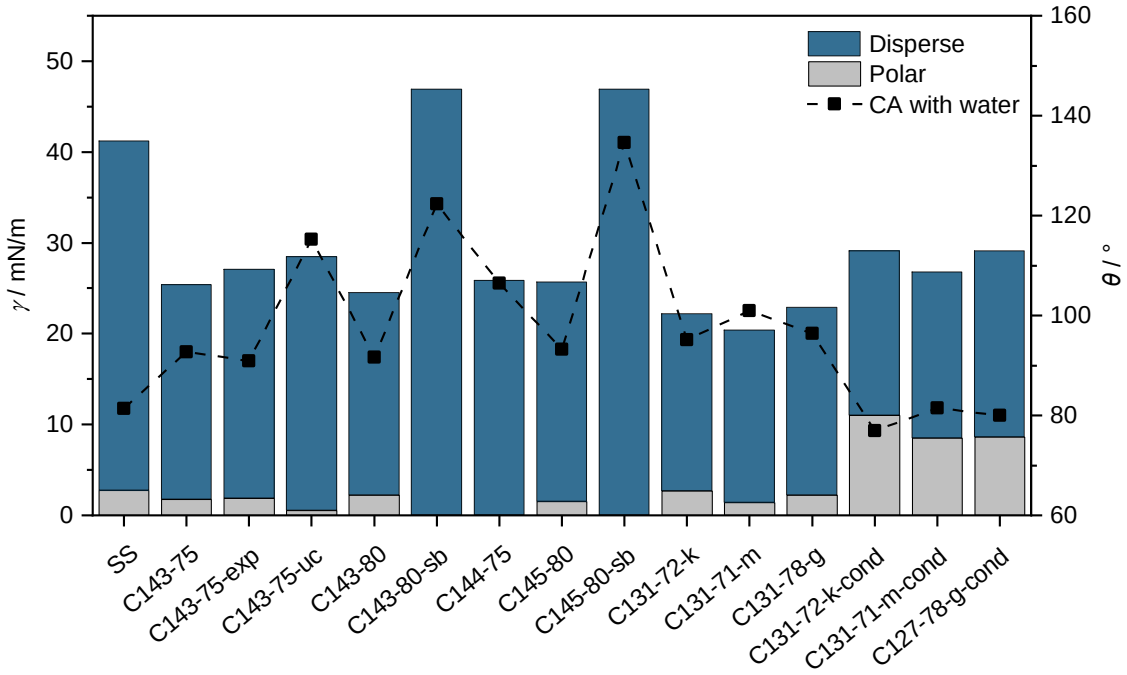

Fig. 2.18: Surface free energies calculated by the OWRK method and static contact angles with water of the materials developed.

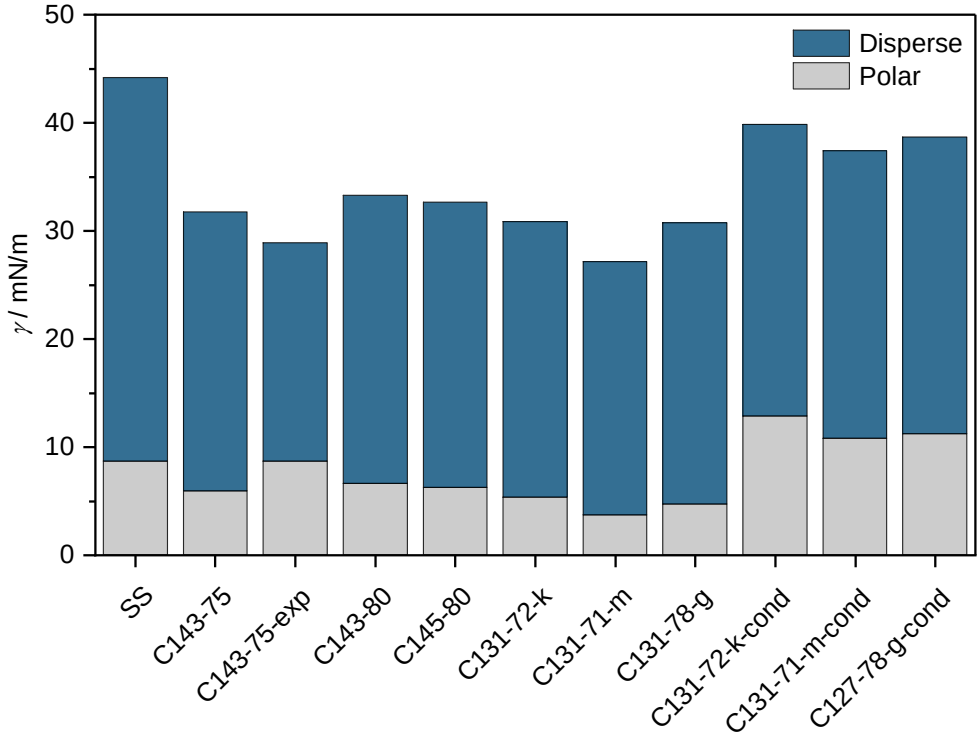

Fig. 2.19: Surface free energies calculated by the WU method of the materials developed.

The materials developed were examined with different graphite filler contents, graphite particle sizes and polymer grades, as well as material post-treatments. Since the polymer grade has no significant influence on the wettability and consequently also on the surface free energy, only PP composites are shown in the corresponding figures. In addition to the polymer grade, the

particle size does not seem to have a major influence on the wettability. With increasing graphite content, however, a slight tendency towards poorer wettability with water and thus a lower polar fraction of the surface free energy can be observed. Overall, the materials in the unconditioned state have a hydrophobic surface (contact angle with water > 90 °). Hence, the materials are significantly less wettable than SS (81.4 °). However, conditioning in water (by immersing the samples in water for at least 24 h) leads to a significant increase in the polar fraction of the surface free energy of the polymer composites. The hydrophobicity of the materials decreases and, consequently, the contact angle with water is reduced (by 11.8 ° on average). Consequently, the materials are found to be more wettable than the reference material after conditioning. The reason for this is probably the water absorption of the materials, which in turn leads to a reversible increase in polarity. Although the water absorption of the selected materials (PP and PPS) is less than 0.1 % [3], this seems to lead to a significant effect. Sandblasting, on the other hand, results in a strong increase in surface energy according to the OWRK method and a significant reduction in wettability. The contact angles with water increase by approx. 30 ° compared to the untreated sample. The reason for this finding has already been mentioned in Section 2.2.2. As shown below, sandblasting increases the roughness of the sample surfaces, which leads to an increase in the apparent contact angle for hydrophobic materials according to Eq. 2.6. However, this also makes the calculation of the surface energy difficult, since the Young contact angle should be used for this purpose. Probably, the surface free energy of the sandblasted surfaces is within the range of the untreated ones, which can be concluded by the findings in Chapter 4. However, the influence of the removal of the upper polymer layer on the surface free energy of the composites could not be investigated in this work, since the focus was on the development and operation of the PHE. The increase of roughness by the use of expanded graphite particles, on the other hand, does not seem to have a significant influence on the wettability or the surface energy. It can therefore be concluded that the surface energies (except for the sandblasted surfaces) are reliably calculated.

Depending on the requirements, a simple increase or decrease of the hydrophobicity can be achieved. Conditioning with water increases the wettability with water, sandblasting reduces it. The resulting influence on the technically relevant fouling behavior is discussed in Chapter 4.

The differences between the OWRK and the Wu method can be seen mainly in the comparison of the polar fractions of the surface free energy, which vary by up to 6.8 mN/m. The surface energies are calculated larger according to the method of Wu as a whole, but especially for the polymer composites. As a result, the differences between the surface energies of the polymer composites and the reference material (SS) are smaller. According to the literature, surfaces

with a generally low surface free energy and polymers can be calculated more accurately using the Wu method [33,50]. However, this method does not cope with surfaces that deviate strongly from ideal surfaces (high roughness) either. Therefore, the calculation of the surface free energies of the sandblasted surfaces with this method does not lead to any result.

Supplementary assessments of fouling susceptibility can be made by knowing the surface roughness of the materials. In general, the fouling induction phase increases with increasing roughness [51,52]. Fig. 2.20 shows the mean arithmetic roughness of selected samples.

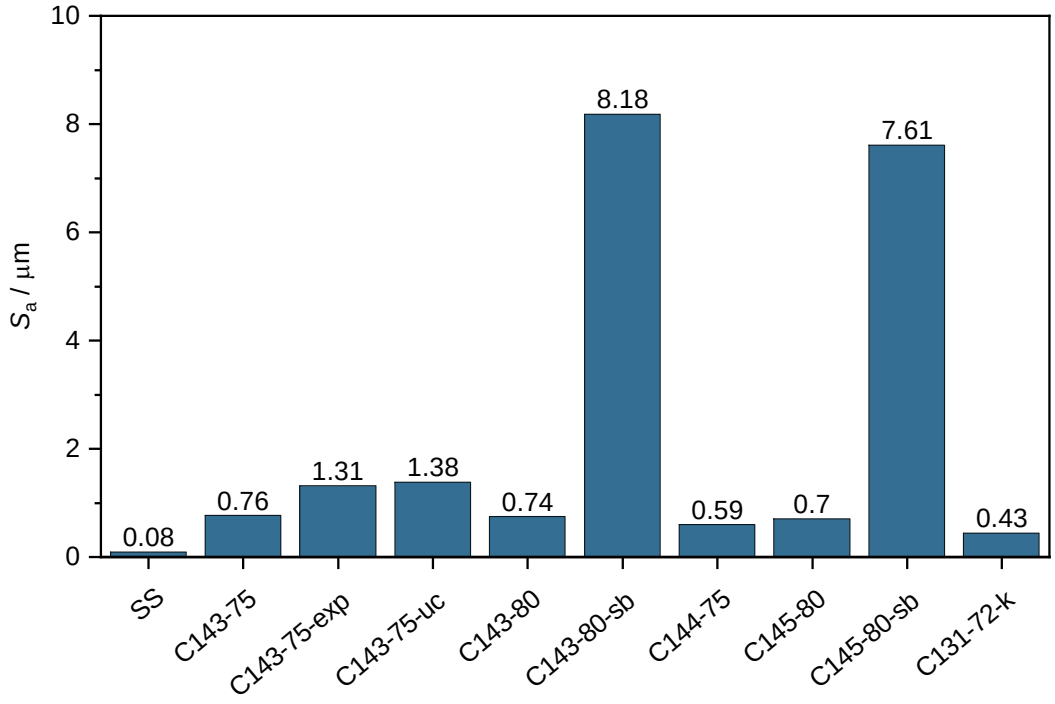

Fig. 2.20: Mean arithmetic roughness of the materials developed.

All samples show higher roughness than the reference material SS. The PP grade and the filler content have no significant influence on the roughness of the samples. The graphite particle size in the polymer composites and the sandblasting of the specimens have the greatest influence. Other factors influencing high roughness are the use of expanded graphite and production without a calender. The extent of the roughness increase due to sandblasting also makes the strong influence on the contact angle seem logical. For a better understanding of the magnitude, it is illustrated in the form of 3D surface plots in Fig. 2.21. The magnitudes of the roughness peaks for the sandblasted sample are a factor of 30 higher than for the untreated sample. Although this may accelerate fouling processes, it may also contribute to the generation of local turbulence and consequently to an increase of the convective heat transfer coefficient [53,54], which will be discussed in the following chapters.

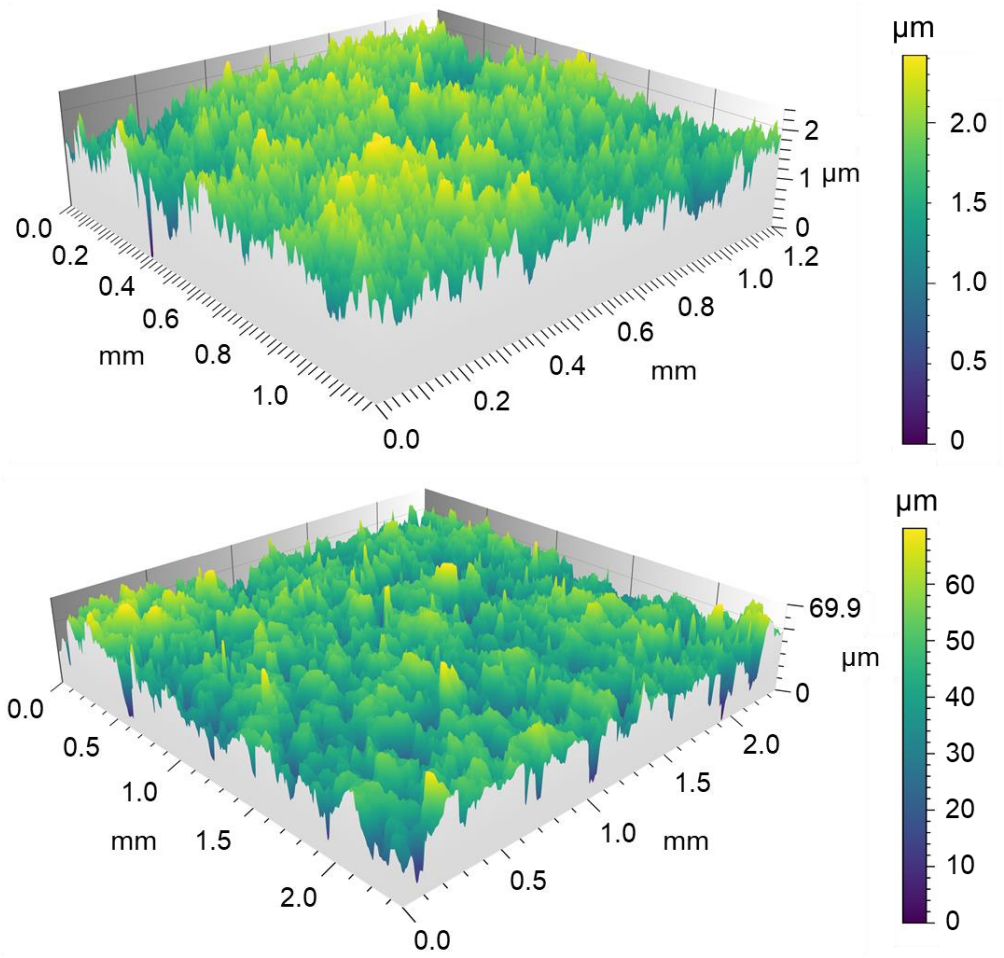

Fig. 2.21: 3D surface profiles of calendered C143-75 (top) and C143-75-sb (bottom).

3 Polymer Composite Plate Heat Exchanger

3.1 Theory

Plate heat exchangers are generally divided into three types: Gasketed (plate and frame), brazed and welded. For the use of polymers and polymer composites, only the design of gasketed plate heat exchangers can be considered. Therefore, the design and fundamental characteristics of these are briefly described below. Detailed information on the plate heat exchanger types not described here, design methods, etc. may be found in the relevant literature [20,24,55,56].

3.1.1 Construction and operation of gasketed heat exchangers

An exploded view sketch highlighting the major structural components of a typical gasketed plate heat exchanger (PHE) is given in Fig. 3.1. The main elements of a PHE include the heat transfer and flow separation plates, gaskets, the supporting end plates that contain the fluid inlet and outlet ports, horizontal guiding bars, and tightening bolts.

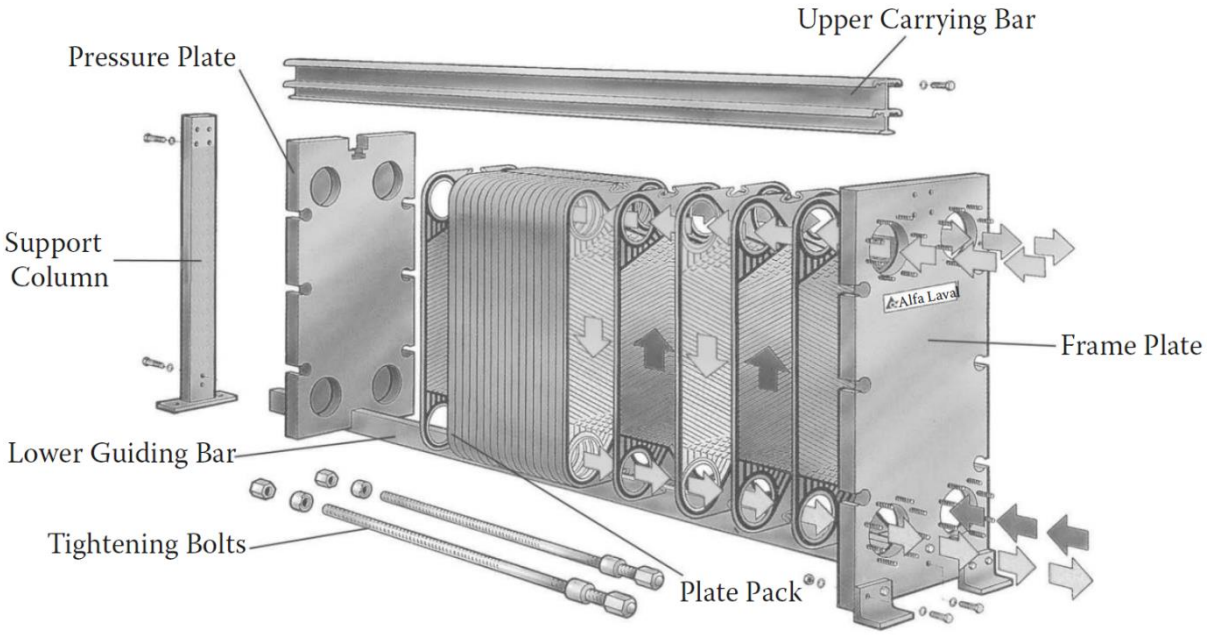

Fig. 3.1: Gasketed plate heat exchanger (courtesy of Alfa Laval AB).

The key element for heat transfer is a stack of corrugated or embossed plates in mutual contact. Each of the plates has four openings that serve as inlet and outlet ports, and gaskets that direct the fluids into alternate flow paths. The flow channels are formed by two adjacent plates so that the two fluid streams, by alternating flow through the channels, transfer heat, as exemplarily shown in countercurrent operation in Fig. 3.1. The plate stack is held together by the frame,

consisting of two end plates, pressing equipment, and connecting ports. Guiding bars ensure the correct positioning of the plates. The entire plate stack is assembled and sealed between the end plates using tightening bolts. Concerning the plate material, metals are mostly used (stainless steel, titanium, Hastelloy, etc.) but the use of gaskets also allows the application of graphite or polymers as heat transfer material.

Flow patterns and pass arrangement

The design of PHEs provides great flexibility regarding different flow arrangements. This is mainly due to the design of the gaskets (gasket arrangement), which is shown as an example for a vertical flow in Fig. 3.2.

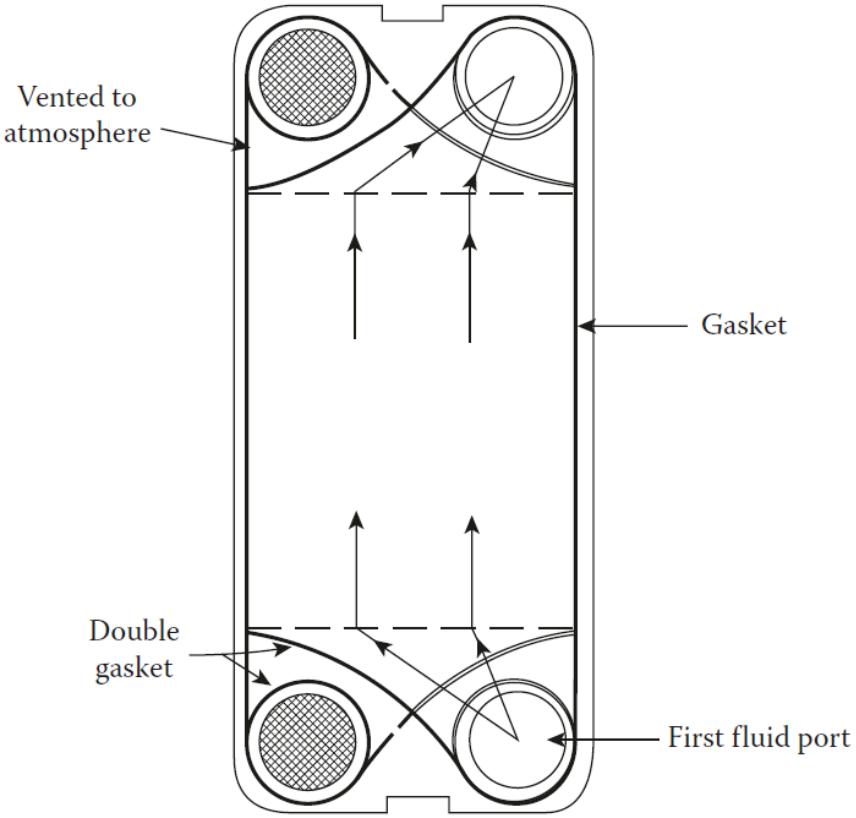

Fig. 3.2: Gasket arrangement. Vertical arranged ports [24].

The flow in a PHE can basically be categorized into the flow direction, the pass, the paths per pass, the distribution along ports and the distribution inside the channel.

- Flow direction

  Countercurrent or parallel flow, where the countercurrent flow allows the highest efficiency due to higher average temperature differences.

- Pass

  The term “pass” refers to a group of channels in which the flow is in the same direction. In single-pass arrangement, the fluids flow in only one direction (upwards or downwards). In multi-pass arrangement, plates with blind holes are used to change the flow direction in the PHE, which leads to an increase in the residence time of the fluids in the heat exchanger (see Fig. 3.3). This results in higher temperature differences at the expense of efficiency.

- Paths per pass

  The number of channels the fluid flow passes through during one pass is called the number of paths per pass. This characteristic correlates with the flow velocity in the channels. The reduction of the paths per pass causes an increase of the flow velocity and vice versa.

- Distribution along ports

  There are two types of distributions, namely U and Z arrangements (see Fig. 3.3). In the U arrangement, all inlets and outlets are located at the same end plate, limiting the system to single-pass arrangements. In the Z arrangement, the inlet and outlet ports are located on opposite end plates. The U configuration allows easy disassembly of the heat exchanger, (e.g., for cleaning). However, the flow distribution in this configuration is more uneven compared to the Z configuration [57].

- Port arrangement

  The ports can be arranged either diagonally (inlet and outlet on the opposite side of the plate) or vertically (inlet and outlet on the same side of the plate, as depicted in Fig. 3.2), which affects the flow distribution in the channels.

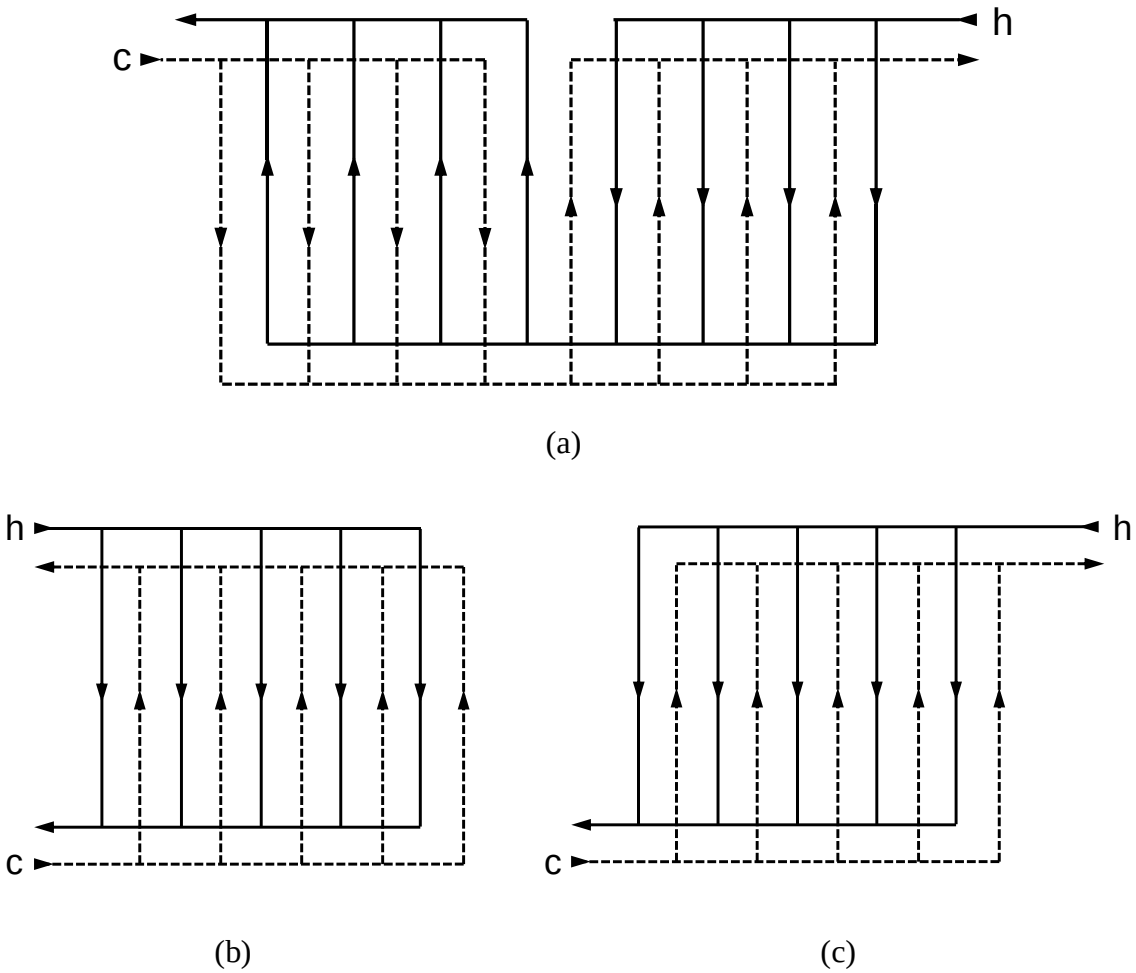

Fig. 3.3: Several PHE flow arrangements. (a) Multi-pass with equal pass (2 pass – 2 pass). (b) Single-pass: U arrangement. (c) Single pass: Z arrangement.

Geometric characterization of chevron plates

Various corrugated plate types are used in practical applications in PHEs. Overall, the chevron type being the most studied [58–61], widely used and offered by all major manufacturers of PHEs [62–64]. The geometrical parameters of a chevron-type plate are shown in Fig. 3.4. It consists of two flow distributors, which are designed to distribute the passing fluid over the entire width *w* and then collect it to the outlet port width, and a core heat transfer section. Both regions are active heat transfer surfaces with only the core region featuring the chevron pattern.

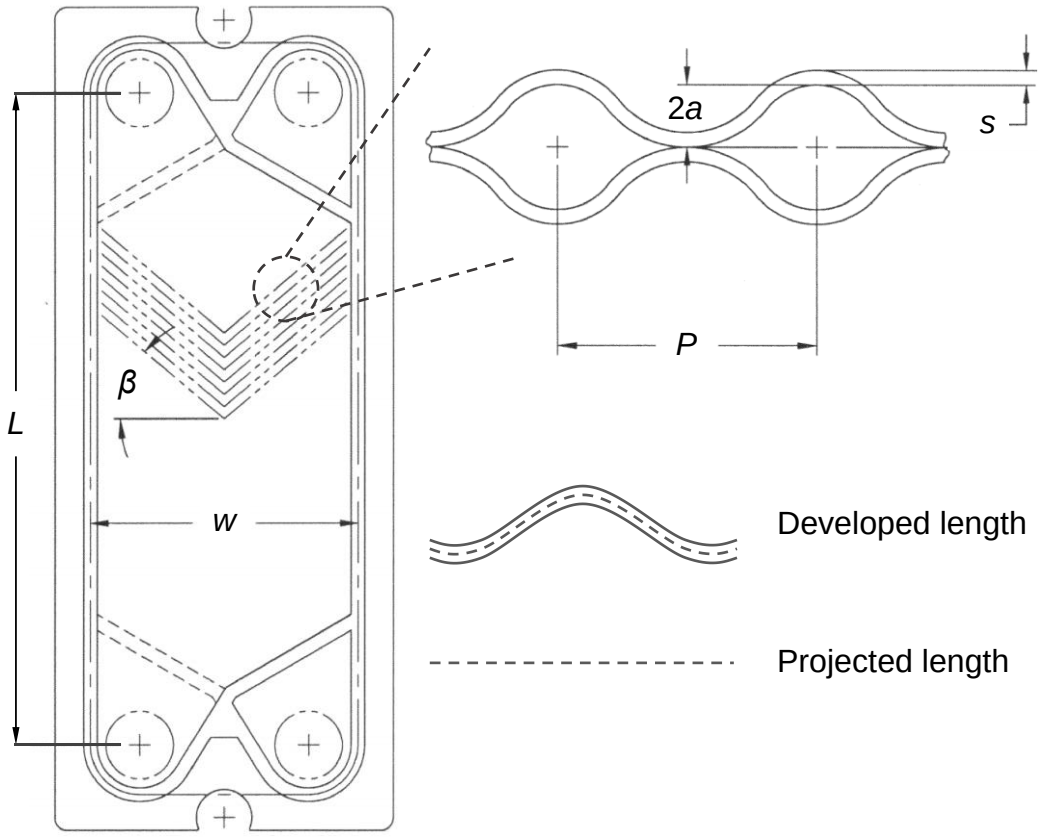

Fig. 3.4: Geometrical parameters of a chevron plate corrugation pattern.

The chevron embossing generates swirling motions in the fluid, whose extent depends, among other things, on the embossing angle β (called chevron angle). Typical angles range between 25 ° and 65 °, whereby the heat transfer and the pressure loss increase with the embossing angle. The reversal of the chevron pattern on adjacent plates results in various contact points that contribute to mechanical stability and thus to ensure low plate thicknesses. The corrugations further cause an increase of the heat transfer surface compared to the original flat plate. It depends on the wavelength of the embossing, called corrugation pitch P, as well as the embossing depth a. The extent of the increase in surface area is expressed in terms of the enlargement factor ϕ:

$$\phi = \frac{\text{Developed length}}{\text{Projected length}} \tag{3.1}$$

The flow channels are the passages formed by two adjacent plates between the gaskets. Since the cross section of a corrugated surface is very complex and varies with position, the mean channel spacing is defined as $2a$. The equivalent diameter D_e or a hydraulic diameter D_h is used to calculate the Reynolds number and convective heat transfer in the flow channels. They are defined as follows:

$$D_{\mathrm{e}} = \frac{4w2a}{2(w+2a)} \approx 4a \tag{3.2}$$

$$D_{\mathrm{h}} = \frac{D_{\mathrm{e}}}{\phi} \tag{3.3}$$

with the approximation that $2a << w$.

3.1.2 Operational characteristics

The use of PHEs offers several advantages over traditional shell and tube heat exchangers. First and foremost, plate surface corrugations provide improved convective heat transfer by creating swirl or vortex flows and disruption and reattachment of boundary layers, resulting in well-mixed flows and consequently high convective heat transfer coefficients. The transition to turbulent flows thus already occurs at low Reynolds numbers (10 – 400 [24]). This favors high compactness combined with low weight, the efficient use of this heat exchanger design in heat recovery measures, and reduced fouling rates. Especially for the use of polymers and polymer composites, which are usually associated with lower thermal conductivities than conventional materials, high compactness is important for achieving competitive performances.

Other features include easy expandability, elimination of cross-contamination, low fluid volume, and suitability for high-viscosity applications. The interested reader is again referred to the literature for further information.

3.2 Materials and Methods

3.2.1 Fabrication process

The conductive polymer composite corrugated heat exchanger plates being investigated were manufactured at the ZBT. The production steps include sheet extrusion, embossing and post-processing of the sheets and are illustrated in Fig. 3.5.

A total of two polymer-graphite composite formulations were used for corrugated plate fabrication, which were evaluated as suitable by the material characterizations discussed in Chapter 2. Firstly, a polypropylene-graphite composite (C143-75; PP-G) for low temperature applications with a graphite mass fraction of 75 % and, secondly, a polyphenylene sulfide-graphite composite (C116-65; PPS-G) for high temperature applications with a graphite mass fraction of 65 %. The graphite used has a D90 value of 45 µm (90 wt.% of the particles are smaller than 45 µm). The procedure for producing the plane sheets (see Fig. 3.5a) has already been outlined in Section 2.2.1. By means of the in-house made chevron dies (Fig. 3.5b), the composite plates were imprinted with the corresponding embossing in a hot-pressing process (c). The exact geometry parameters of the plate patterns are given in Tab. 3.1.

Tab. 3.1: Design parameters of the developed PHE.

Design parameter	**Value**
Effective plate width (w)	0.09 m
Effective plate length (L)	0.158 m
Effective heat transfer area (A)	$11.13 \cdot 10^{-3}$ m²
Plate thickness (s)	0.85 – 2.5 mm
Chevron angle (β)	60°
Corrugation pitch (P)	4 mm
Corrugation amplitude (a)	0.5 mm
Enlargement factor (ϕ)	1.14
Aspect ratio (α)	0.5

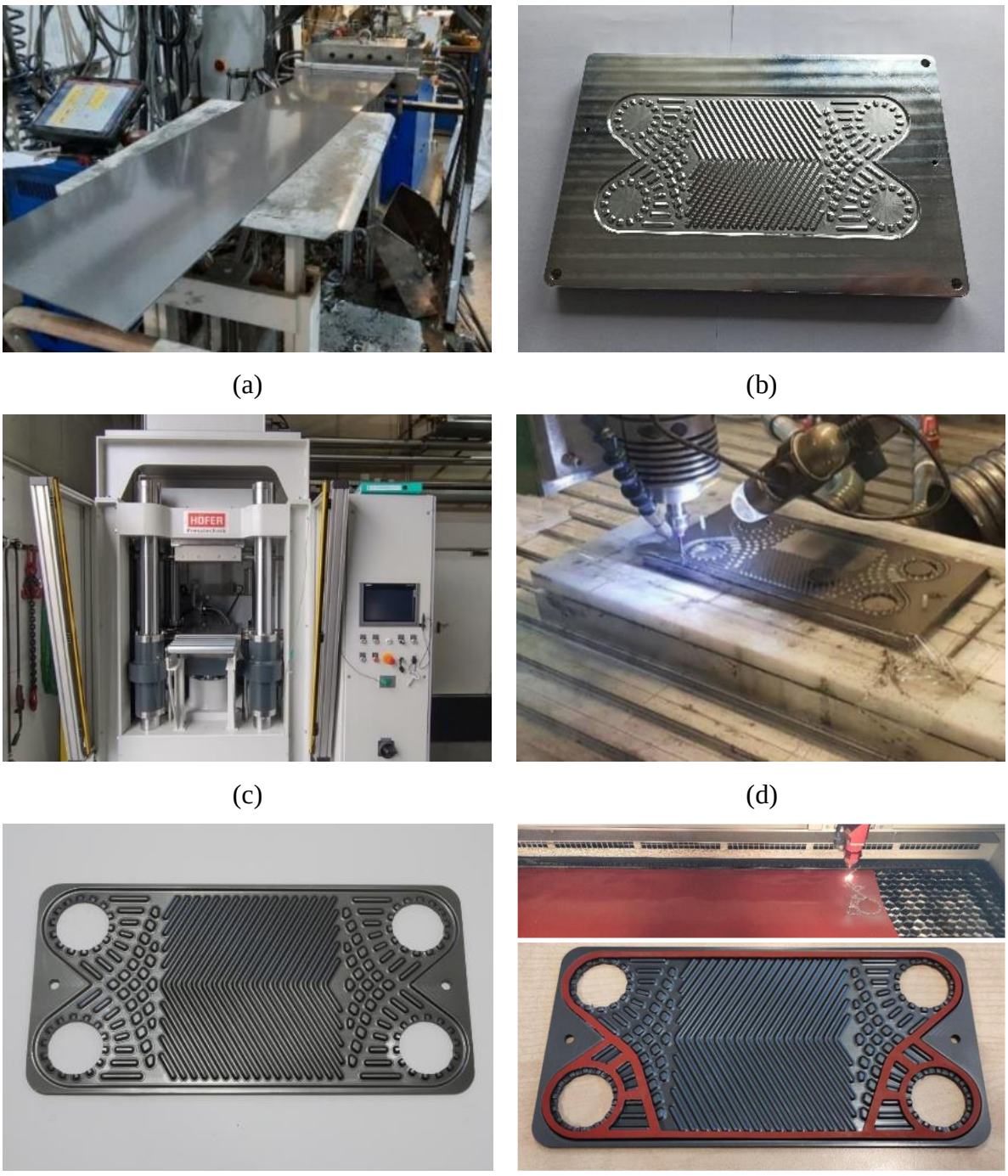

(a) (b)

(c) (d)

(e) (f)

Fig. 3.5: Fabrication process of the polymer composite – PHE: (a) Film extrusion; (b) Chevron die; (c) Hot pressing of the composite plates; (d) Milling out the fluid ports; (e) Chevron plate; (f) Gasket laser cutting.

The PP-G plates have been embossed at ~ 430 K and the PPS-G plates at ~ 570 K. The embossing force was 13.5 N/mm² for both types of plates. After embossing, the edges and the ports were milled out (d) so that the plate was ready for assembling (e) in the heat exchanger. To ensure tightness of the heat exchanger, gaskets are laser cut from a silicone mat (f) which is suitable for temperatures up to 200 °C. The gasket has an uncompressed thickness of 1.5 mm

and a Shore A 60 hardness. To produce a completely polymer-based plate heat exchanger, the clamping plates were made of 18 mm thick polyoxymethylene. This material can withstand relatively high temperatures (up to 100 °C continuously), acts as an insulator (0.3 W/mK) and has very good mechanical properties (strong and rigid) for a polymer. Eighteen evenly spaced M6 stainless steel screws provide the screw connection and thus the sealing of the heat exchanger. Fig. 3.6 shows the construction of the entire PHE as an exploded view. The use of the gasketed plate heat exchanger design allows the number of plates to be varied. In addition, fouling processes can not only be investigated data-based but also visually analyzed at the end of the tests to assess fouling susceptibility.

Fig. 3.6: Exploded view of the developed heat exchanger.

3.2.2 Experimental set-up and procedure

The heat transfer experiments were performed using the PHE shown in Fig. 3.6 to study profiled plates and in the heat exchanger test cell (HX) shown in Fig. 3.7 to study flat plates. The use of flat plates allowed the experimental comparison with the reference material SS, whereas the material comparison for the PHE was performed via the model presented in Section 3.2.3, since an experimental comparison must be based on the same geometric parameters of the materials to be compared. However, the existing equipment for producing embossed plates is not suitable for metallic materials.

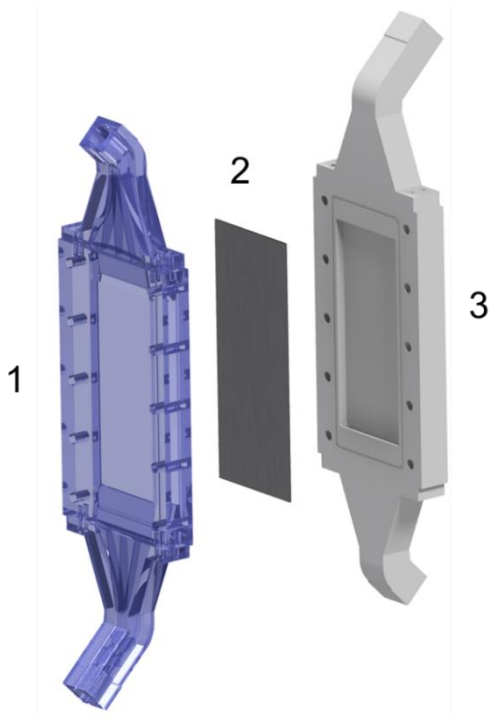

Fig. 3.7: Set-up of the plate heat exchanger test cell (HX). (1) Cold water circuit, (2) Flat plate sample, (3) Hot water circuit.

All heat transfer experiments were carried out in the screening apparatus shown schematically in Fig. 3.8. The setup contains a vertically oriented interchangeable test section (4, in Fig. 3.8) to be able to exchange between HX and PHE.

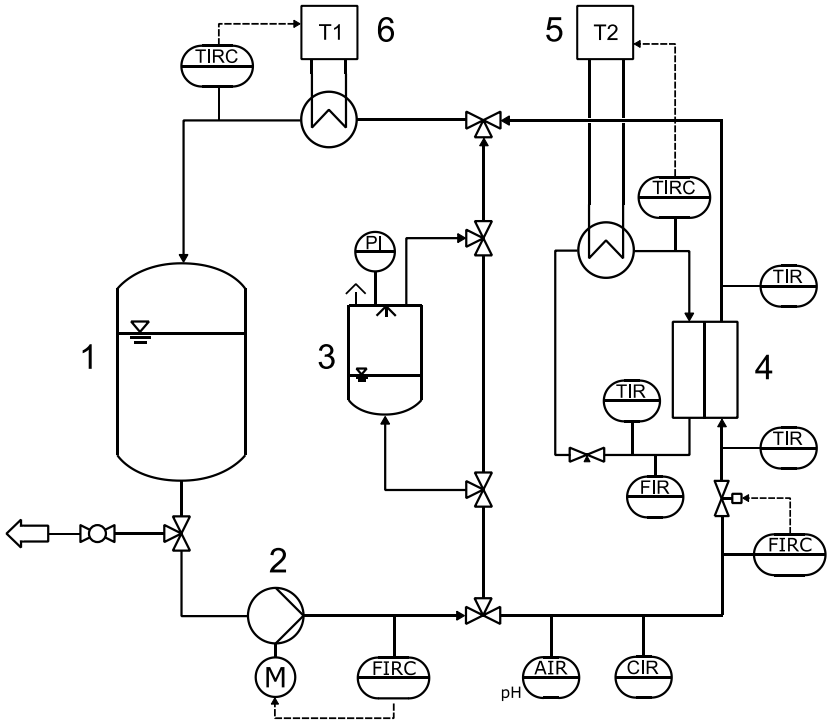

1 Tank

2 Pump

3 Degasser

4 Heat exchanger

5 Heating circuit thermostat

6 Thermostat for bulk temperature control

Fig. 3.8: Process flow chart of the experimental set-up.

The HX (see Fig. 3.7) has a rectangular heat transfer surface of 144 cm². To avoid vortex formation and thus locally strong shear forces during the experiments, the inlets are aligned longitudinally to the heat transfer surface. In addition, flow diffusers are located at the inlets and outlets to ensure a uniform flow over the heat transfer surface. However, the flow entering the HX can neither be assumed as hydrodynamically nor thermally fully developed. The sample material acts as a heat transfer wall and separates the cold liquid from the hot liquid. The heating side of the test section is made of polyoxymethylene and is additionally insulated to ensure almost adiabatic conditions. The solution side is made of polymethylmethacrylat to allow visual monitoring of possible bubble formation. The design and geometry of the PHE has already been described in Section 3.2.1. Both heat exchangers were operated in counter as well as in parallel flow. In the case of the PHE, however, a distinction is made not only between the flow direction but also between the pass arrangement and the distribution along port manifolds, as described in Section 3.1.1. For the investigations conducted in this thesis, only two arrangements were used, one of which corresponds to an overall counter-flow arrangement (No. 111, see Fig. 3.9a) and one to an overall parallel-flow arrangement (No. 113, see Fig. 3.9b). The naming is based on the classification method of Kandlikar and Shah [65].

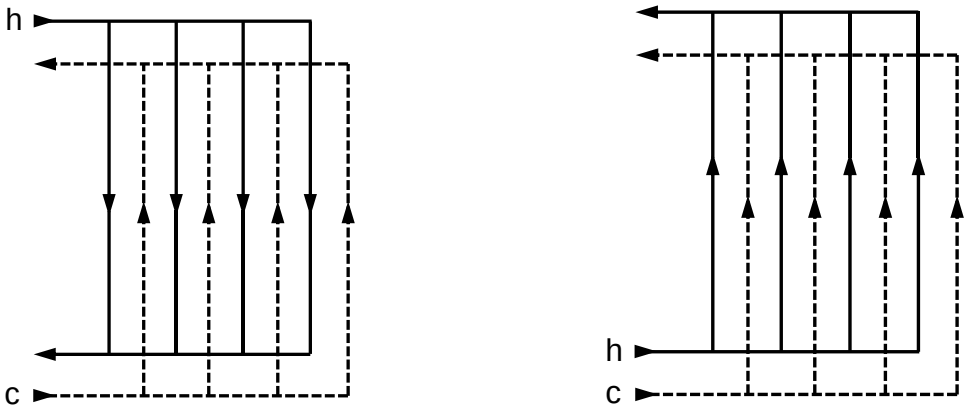

Fig. 3.9: Used pass arrangements. (a) No. 111. (b) No. 113.

Both the hot and cold fluids circulate through the heat exchanger, forced by a centrifugal pump (2, in Fig. 3.8) in the case of the cold fluid circuit or by the pump integrated in the thermostat (5) in the case of the hot fluid circuit. Deionized water was used as the heat transfer fluid. Temperature sensors (Pt100 1/ DIN) were placed in the flow directly at the inlet and outlet of the heat exchangers (4), where the temperature distribution and flow profiles are homogeneous. In order to create constant test conditions, the relevant operating parameters were controlled. The volume flow rates of the fluids entering the heat exchanger were controlled with needle valves and a speed control of the centrifugal pump. The fluid inlet temperatures were controlled

by the thermostats (5) and (6), respectively. All relevant temperatures and volume flows are recorded continuously to guarantee an accurate energy balance.

To suppress potential bubble formation on the surfaces under investigation, a vacuum spray tube degasser (3) was operated before the start of the corresponding experiments, which, according to the manufacturer, removes 90 % of the dissolved gases. Degassing of the fluid before the start of an experiment is indicated subsequently by dg (degassed).

Using the energy balance for the calculation of the heat transfer rate $\dot{Q}$, the overall heat transfer coefficient U is calculated according to Eq. 3.4. The calculations of the heat transfer rate refer to the cold fluid, where energy losses are almost excluded, as there is the smaller temperature difference to the environment (approx. 20 °C). Additionally, a very accurate Coriolis flow meter is used (measurement accuracy of 0.1 %). To compensate for measurement fluctuations, the data were recorded every second for 10 minutes after a steady state was reached, and the mean overall heat transfer coefficient was determined.

$$U = \frac{\dot{Q}}{A\Delta T_{lm}} \tag{3.4}$$

The bias uncertainties in the overall heat transfer coefficients were determined by calculating the 95 % confidence intervals according to Eq. 3.5, which are composed of the measurement uncertainties of the recorded temperatures ($T_{\mathrm{h,in}}$, $T_{\mathrm{h,out}}$, $T_{\mathrm{c,in}}$, $T_{\mathrm{c,out}}$) and the mass flow of the cold fluid.

$$B_U = \sqrt{\left[\sum_T \left(\frac{\partial U}{\partial T} B_T\right)^2 + \left(\frac{\partial U}{\partial \dot{m}_{\mathrm{c}}} B_{\dot{m}_{\mathrm{c}}}\right)^2\right]} \tag{3.5}$$

The heat transfer measurements were performed for various operating conditions, shown in Tab. 3.2. For the investigation of the flat plates conducted in the HX, the plate materials, wall thicknesses and operating conditions were varied. In addition, the number of thermal plates was varied for the profiled plate studies conducted in the PHE. Thereby, the expression thermal plate (or heat plate) refers to the plates in the PHE that transfer heat, excluding the two end plates (for illustration see Fig. 3.10).

Tab. 3.2: Operating conditions of the heat transfer measurements.

Operating parameter	HX	PHE
Reynolds number hot fluid (Re_h)	3800	200 - 1600
Reynolds number cold fluid (Re_c)	300-3000	200 - 1600
Inlet temperature hot fluid ($T_{h,in}$)	70 °C; 80 °C	70 °C; 80 °C
Inlet temperature cold fluid ($T_{h,in}$)	25 °C	40 °C
Number of plates (N_{tp})	1	1-7

3.2.3 Plate heat exchanger modeling

To evaluate the performance of the developed PHE in comparison to established materials, either a direct experimental comparison (exactly the same PHE geometry and the same experimental conditions are necessary) or a mathematical model is required. Since the thermal plates produced have a thickness *s* that is partly unusual for conventional materials, the primary approach is excluded, which is why a rigorous modeling approach was used. This method allows a performance comparison between the developed polymer composites and e.g., stainless steel not only for the realized geometry parameters (see Tab. 3.1) but over a wide range of all relevant material properties (particularly the thermal conductivity λ), operating (temperatures T and mass flows $\dot{m}$) and geometry parameters.

Considering the energy balance of a small control volume *dx* in a PHE according to Fig. 3.10 and assuming that the heat transferred to the fluid from the adjacent channels is equal to the enthalpy change of the fluid, the following differential equations (3.6 - 3.8) are obtained to describe the temperature variation in the *x*-direction.

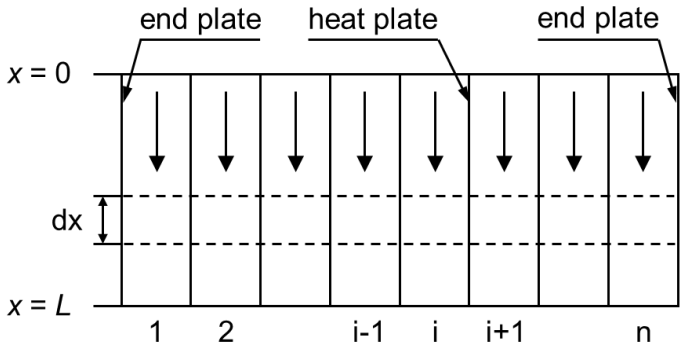

Fig. 3.10: Schematic diagram of a PHE.

Here, Eq. 3.6 corresponds to the first, Eq. 3.7 to an intermediate, and Eq. 3.8 to the last channel where the end plates are considered adiabatic:

$$\frac{dT_1}{dx} = \frac{Uw}{C_1}(T_1 - T_2) \tag{3.6}$$

$$\frac{dT_\mathrm{i}}{dx} = \frac{Uw}{C_\mathrm{i}}(2T_\mathrm{i} - T_{\mathrm{i}-1} - T_{\mathrm{i}+1}) \tag{3.7}$$

$$\frac{dT_\mathrm{n}}{dx} = \frac{Uw}{C_\mathrm{n}}(T_\mathrm{n} - T_{\mathrm{n}-1}) \tag{3.8}$$

with the overall heat transfer coefficient defined as:

$$U = \left(\frac{1}{h_\mathrm{h}} + \frac{s}{\lambda} + \frac{1}{h_\mathrm{c}}\right)^{-1} \tag{3.9}$$

In the above equations, *w* is the effective plate width and *C* the heat capacity flow rate. The subscripts h and c indicate the hot and cold fluid stream. Thereby *U*, as well as the fluid temperatures, are solved as a function of the position *x* for higher accuracy instead of assuming an average overall heat transfer coefficient. To calculate the overall heat transfer coefficient *U* (Eq. 3.9), respectively the convective heat transfer coefficients *h*, different Nusselt correlation were applied, which cover the selected plate geometry and operating conditions, as given in Tab. 3.3. In addition, CFD simulations of plate heat exchanger sections were used to generate a customized Nusselt correlation adapted to the exact geometry of the developed heat exchanger plates (see Section 3.2.4). By using different Nusselt correlations it could be evaluated which one provides the best agreement with the experimental data.

Tab. 3.3: Heat transfer correlations.

Investigator	Nusselt correlation			Comments
Muley and Manglik [66]	$Nu = C_1 C_1' Re^{p1} Pr^{1/3}(\mu/\mu_w)^{0.14}$			$Re > 10^3$, $30 \le \beta \le 60$
	$C_1 = 0.2668 - 6.967\times10^{-3}\beta + 7.244\times10^{-5}\beta^2$			$1 \le \phi \le 1.5$
	$C_1' = 20.78 - 50.94\phi + 41.16\phi^2 - 10.51\phi^3$			
	$p1 = 0.728 + 0.0543\sin[(\pi\beta/45) + 3.7]$			
Kumar [67]	$Nu = C_1 Re^m Pr^{0.33}(\mu/\mu_w)^{0.17}$			ϕ = 1.17, C1 and m are constants and given as:
	Re	C1	m	
	20 - 400	0.306	0.529	
	> 400	0.108	0.703	
Wanniarachchi et al. [68]	$Nu = [Nu_1^3 + Nu_t^3]^{1/3} Pr^{1/3}(\mu/\mu_w)^{0.17}$			$1 \le Re \le 10^4$; $20 \le \beta \le 62$
	$Nu_1 = 3.65\,\beta^{-0.455}\,\phi^{0.661}\,Re^{0.339}$			
	$Nu_t = 12.6\,\beta^{-1.142}\,\phi^{1-m}\,Re^m$			
	$m = 0.646 + 0.0011\,\beta$			

Since the fluid viscosity μ at wall temperature must also be known for the calculation of h with the above correlations, these are calculated according to the relation shown in Eq. 3.10.

$$\dot{Q} = \frac{T_\mathrm{h} - T_\mathrm{w,h}}{\frac{1}{h_\mathrm{h} A}} = \frac{T_\mathrm{w,c} - T_\mathrm{c}}{\frac{1}{h_\mathrm{c} A}} = \frac{T_\mathrm{h} - T_\mathrm{c}}{\frac{1}{UA}} \tag{3.10}$$

Where the subscript w indicates the temperature at the wall. Furthermore, various geometry parameters are included in the correlation or needed for the Eqs 3.6 - 3.8. These were chosen for model validation according to the parameters listed in Tab. 3.1. For the material comparison, the parameters given in Tab. 3.4 were selected, which were kept within the scope of the state of the art.

Tab. 3.4: Parameters of the PHE modeling for material comparison.

Design parameter	**Value**
Effective plate width (w)	0.2 m
Effective plate length (L)	0.6 m
Chevron angle (β)	60°
Corrugation Pitch (P)	8 mm
Corrugation amplitude (a)	1 mm
Enlargement factor (ϕ)	1.15

3.2.4 CFD modeling

Model design

The goal of the CFD simulations is to create a customized correlation for the heat transfer coefficient or the Nusselt number of the developed plate heat exchanger. As can be seen in Tab. 3.3, these are always dependent on the dimensionless numbers Re and Pr. Therefore, it is first necessary to verify whether the Nusselt number of the PHE under investigation depends only on these dimensionless numbers or on additional parameters. To assess the dependence of the Nusselt number on other parameters, a sensitivity analysis is carried out. For this purpose, the correlation matrix is calculated to assess the relationship between the parameters. This is symmetrical and its contained values, the correlation coefficients r_{xy}, can vary between -1 and 1. They are obtained by [69]:

$$r_{xy} = \frac{\sum_\mathrm{k}((x_\mathrm{k} - \bar{x})(y_\mathrm{k} - \bar{y}))}{\sqrt{\sum_\mathrm{k}(x_\mathrm{k} - \bar{x})^2 \cdot \sum_\mathrm{k}(y_\mathrm{k} - \bar{y})^2}} \tag{3.11}$$

The correlation coefficient describes the relationship between two variables x and y. The expression $\bar{x}$ and $\bar{y}$ denotes the mean value of all data points x_k and y_k, respectively. The value -1 indicates a negative linear correlation, the value 1 indicates a positive linear correlation and the value 0 indicates no correlation. The values between 0 and 1 or -1 describe the magnitude of the dependency. Values below 0.3 indicate almost no correlation. Furthermore, the correlation matrix can be used to prevent multicollinearity, i.e. the strong interdependence of two independent variables, by representing the relationship between all variables [69]. To create a correlation matrix, a broad database is necessary. Therefore, different configurations of the PHE are simulated. The inlet temperature of the cold fluid T_c as well as the hot fluid T_h, the temperature difference between the inlet temperatures ΔT_{in}, the plate spacing s_p, the Reynolds number Re, the thermal conductivity of the plate material λ and the number of thermal plates N_{tp} are varied according to Tab. 3.5.

Tab. 3.5: Parameters of the PHE simulations.

Design parameter	**Value**
Inlet temperature cold fluid ($T_{c,in}$)	0.2 m
Inlet temperature cold fluid ($T_{h,in}$)	0.6 m
Plate spacing (s_p)	0 - 2 mm
Reynolds number cold fluid (Re_c)	500-2000
Reynolds number hot fluid (Re_h)	500-2000
Quantity of thermal plates (N_{tp})	2 - 4
Thermal conductivity of the wall (λ)	1.13 – 100 W/mK

The Prandtl number Pr depends only on temperature-dependent quantities. Therefore, by varying the input temperatures, a database of the Nusselt number for different Prandtl numbers is created. In the case of dependence, another parameter may have to be included in the model equation, as well as, for example, the dependence of viscosity in the correlations in Tab. 3.3. Otherwise, this parameter is neglected, and the fitting is performed only to the reduced equation:

$$Nu = aRe^{b} \cdot Pr^{c} \tag{3.12}$$

To fit the model to the data obtained by the simulations, the downhill simplex method is chosen. To assess the quality of the fit, the root mean squared error (RMSE) is calculated and minimized:

$$\mathrm{RMSE} = \frac{1}{n_{sim}} \cdot \sqrt{\sum_{i=1}^{n_{sim}} \left(\frac{Nu_{sim,i} - Nu_{model,i}}{Nu_{sim,i}} \right)^2} \tag{3.13}$$

To assess the data, R-Square is also determined, which is a measure of the quality of a fit. It describes the amount of scatter in the data, provided by the underlying model [69]:

$$R^2 = \frac{\sum_i \left(Nu_{model,i} - \overline{Nu} \right)^2}{\sum_i \left(Nu_{sim,i} - \overline{Nu} \right)^2} \tag{3.14}$$

The value $\overline{Nu}$ indicates the average value of the data from the simulation for the Nusselt number.

Simulation

The commercial softwares ANSYS Fluent® [70] and ANSYS Worbench® [71] are used to simulate the PHE. Images used courtesy of ANSYS, Inc. Due to the plate sizes, number of plates and the complex inlet and collection structures (flow distributors), the meshing of the entire heat exchanger leads to an exorbitant number of cells, resulting in a very high computing time. Therefore, it is appropriate to reduce the size of the plate heat exchanger and thus the number of cells. For this reason, as before in the mechanical simulations, only a section of the plate heat exchanger is simulated (see Fig. 3.11). The latter is cut from the central heat-transferring surface, which has the inserted embossing pattern. Considering the symmetrical structure of the plate, only a section with half the plate width is simulated. First, the geometries to be investigated were set up using Autodesk Inventor®. This includes different plate spacings as well as different plate quantities. The hot fluid is located adjacent to the outer plates. In the case of direct plate contact ($s_p = 0$), an additional geometry must be created in the area of the contact points of the plates, since the mesh must be particularly highly resolved in this area in order to be able to accurately represent the geometry and resolve the turbulent effects (see Fig. 3.11). This is followed by meshing with Ansys Meshing. Thereby, inflation layers are used in the near-wall region of the fluid to dissolve the boundary layer. The rest of the geometry is meshed with unstructured tetrahedral cells. A coarse mesh is used for the solid material domain, since only thermal conduction and no flow effects occur here. To assess the mesh quality, the dimensionless wall distance y+ is determined after each simulation and the mesh is adjusted in the boundary layer region so that the first cell is located in the viscous sublayer. This is performed in several iteration steps. An example of a mesh is given in Fig. 3.11.

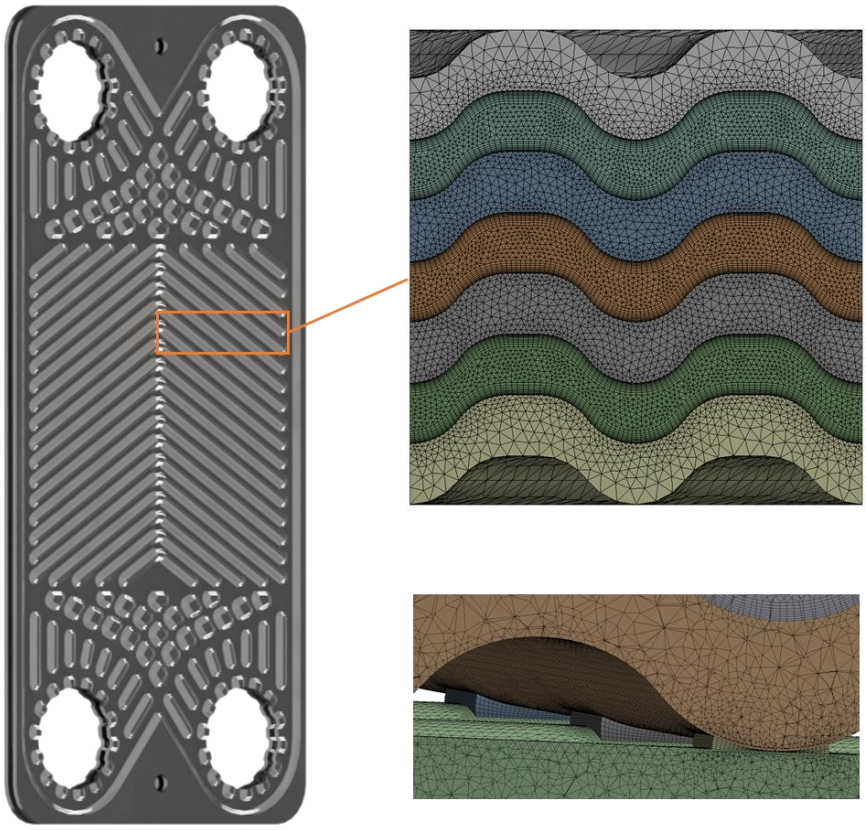

Fig. 3.11: Computational domain for the heat transfer simulations of the PHE. (l) Used plate heat exchanger geometry. (r) Illustration of mesh within the fluid domain and around the contact points.

In total, the studied domains consist of 13 million to 16.5 million cells. The simulations for all configurations are performed for a steady-state flow field, and the k-ω SST model is chosen as turbulence model. Water is chosen for both the hot and cold fluid, and the PHE is simulated in countercurrent flow. The transferred heat flux is chosen as convergence criterion. Subsequently, using post-processing in Ansys Fluent, the convective heat transfer coefficient for each wall is determined. This is computed as given in Eq. 3.15 using the heat flux through the wall, the wall temperature, and a reference temperature to be specified. The area-averaged average is then calculated [72]:

$$h = \frac{1}{A}\int_0^A \frac{\dot{q}}{T_\mathrm{w} - T_\mathrm{ref}}\,dA \tag{3.15}$$

The arithmetic mean of the inlet and outlet temperature is taken as the reference temperature for the hot and cold fluid, respectively:

$$T_\mathrm{ref} = \frac{T_\mathrm{in} + T_\mathrm{out}}{2} \tag{3.16}$$

Due to the use of a small PHE section, only small temperature differences between inlet and outlet occur. In particular, if the temperature differences ΔT_{in} and ΔT_{out} are similar, the arithmetic temperature difference is used instead of the mean logarithmic temperature difference. For further evaluation, the heat transfer coefficient is finally converted into the Nusselt number according to Eq. 3.17:

$$Nu = \frac{hL}{\lambda_{\text{fluid}}} \tag{3.17}$$

3.3 Results and Discussion

3.3.1 Thermal performance

Heat exchanger test cell

Fig. 3.12 and Fig. 3.14 show the results of selected heat transfer measurements conducted on flat heat transfer materials in the HX. The comparison of the *U* values at different operating conditions in Fig. 3.12 impressively shows the influence of the flow regime on the convective heat transfer coefficient and consequently the overall heat transfer coefficient. However, depending on the proportion of the thermal resistance of the wall (R_w) in the total thermal resistance of the heat transfer (R_{tot}, equals the reciprocal of *U*), the overall heat transfer coefficient is more or less affected by change in Reynolds number. Thus, the *U* value increases very strongly with Reynolds number for samples with high thermal conductivity (or low R_w). Based on these explanations, the *U* value for the polymer composite sample increases less than that for the SS sample as the Reynolds number increases since its thermal resistance is about 8 times higher at the same wall thickness.

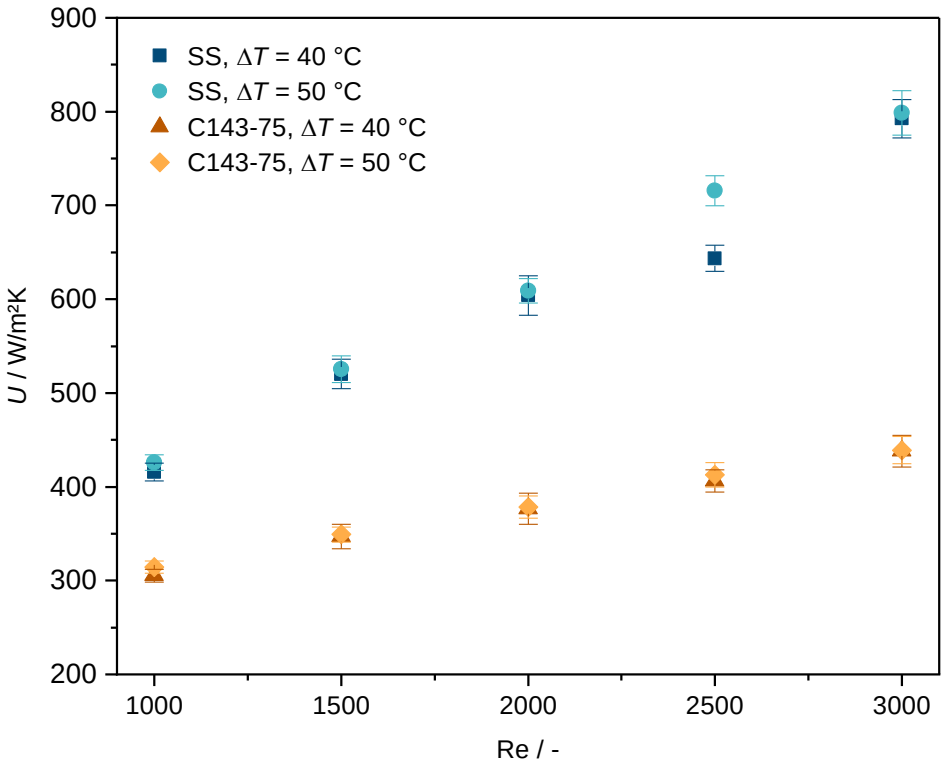

Fig. 3.12: Dependence of the overall heat transfer coefficient on the operating conditions. $Re_c = Re_h$. $T_{c,in}$ = 30 °C. s = 2 mm.

Strictly speaking, the polymer composite sample C143-75 benefits to the same extent as the SS sample from an increase in Reynolds number, in terms of heat transfer. In fact, the thermal resistances of the heat transfer from the fluid to the wall (R_{fluid}) decrease by the same amount, regardless of the material, as can be seen from the illustration of the thermal resistances (see Fig. 3.13). However, as the proportion of R_w to R_{tot} increases, the former becomes limiting and the increase in the U value is slowed down. Nevertheless, Fig. 3.13 shows that even in the turbulent flow regime a large fraction of R_{tot} is due to R_{fluid}. Complementing this with the fact that the evaluations in Fig. 3.12 and Fig. 3.13 are based on polymer composites with high wall thickness (2 mm), it can be concluded that further increases in turbulence, e.g. by the manufacturing of structured plates (PHE), could further exploit the potential of these materials. For comparison: the thermal resistance of a PP wall of the same thickness is about 11.8 m²K/kW. In this case, surface structuring with the aim of reducing R_{fluid} would be unnecessary.

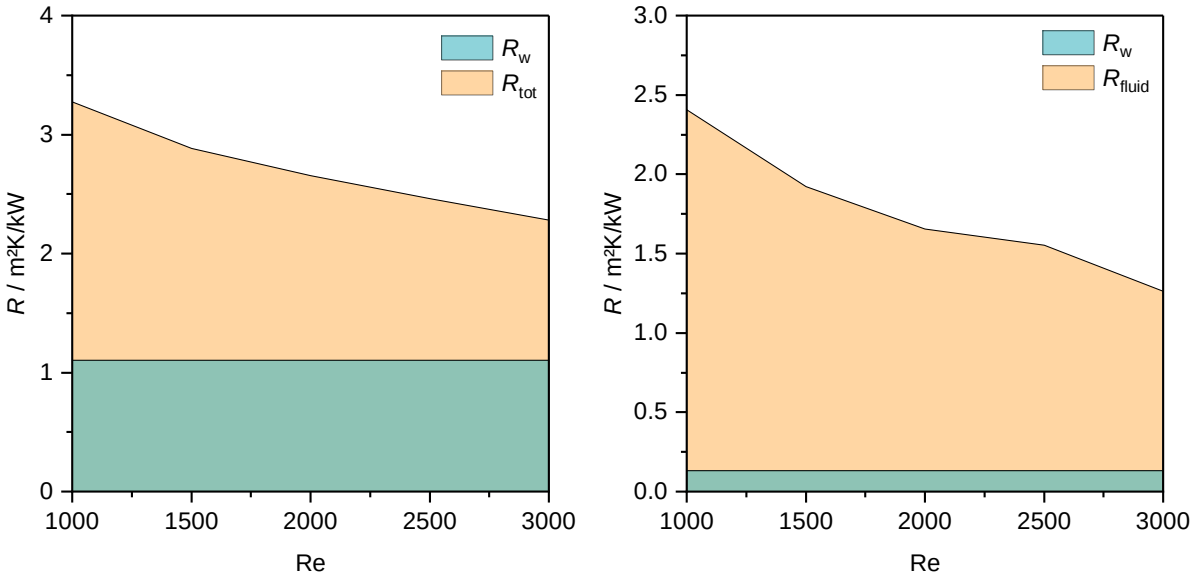

(a) (b)

Fig. 3.13: Thermal resistances as a function of flow characteristics. $Re_c = Re_h$. ΔT = 40 °C. $T_{c,in}$ = 30 °C; $T_{h,in}$ = 70 °C. (a) C143-75. (b) SS.

This results also show that the comparison (using the *U* value as an indicator) differs among materials for different operating points. A qualitative material comparison is made at this point based on Fig. 3.14, which shows the *U* values for laminar as well as turbulent flow conditions on the cold side and turbulent flow conditions on the hot fluid side. It can be seen that the PP grade has only a minor influence on the heat transfer. The graphite content in the sample also has only a minor influence on the heat transfer in the range investigated (75 - 80 wt.%), which is also confirmed by the thermal conductivity measurements in Section 2.3.2. The greatest influence on the heat transfer results from sandblasting (sb) of the specimens, which improves it by up to 19 %. The extent of this phenomenon is dependent on the operating conditions (especially Re), but also on the intensity of the sandblasting. As mentioned in Section 2.3.2, sandblasting removes the polymer film from the surface of the samples and greatly increases the roughness. This increases both the thermal conductivity and the convective heat transfer coefficients during operation. This also shows that the determination of thermal conductivity alone is not sufficient to evaluate materials with regard to their performance in heat exchangers. The thermal conductivity of the composite C143-80 could be increased by 8.9 % by sandblasting (see Figure 2.12), whereas the *U* value in heat exchanger operation could be increased by 11-19 %. In order to cause such an increase of *U* by an increase of the thermal conductivity alone, it would have to be significantly higher, which has already been shown by the above explanations. With respect to the heat transfer, sandblasting of the polymer composites is consequently recommended.

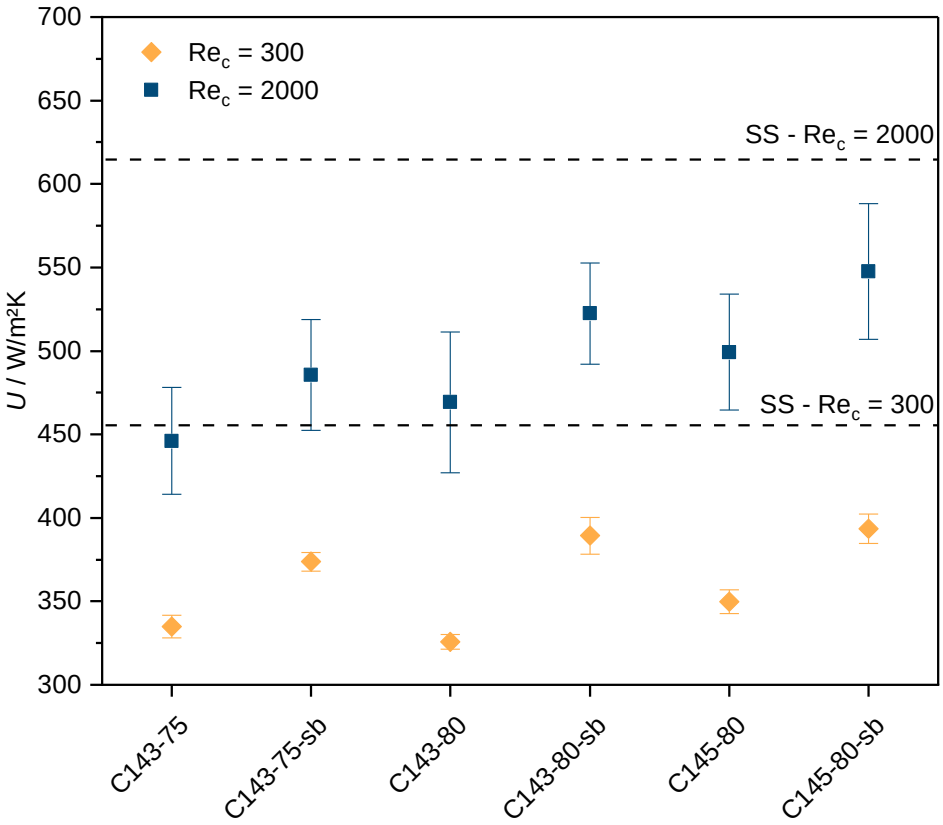

Fig. 3.14: Dependence of the U value on the investigated material. Re_h = 3800; ΔT = 45 °C; $T_{c,in}$ = 25 °C; $T_{h,in}$ = 70 °C.

The cause of the increase of the convective heat transfer coefficient by sand blasting is similar to that occurring in crystallization fouling processes (investigated in the following Chapter 4). Some of the roughness peaks appear to be so large that they penetrate the viscous sublayer, leading to local turbulence and consequently an increased convective heat transfer coefficient [73]. For the laminar case shown, the PP-graphite composites achieve U values corresponding to 60-85 % of the value of SS. If the large density difference between SS and the composites is also considered (approx. a factor of 4.7), the composites appear to be competitive with SS, which will be addressed in Section 3.3.3. Overall, the results shown in Fig. 3.14 are not transferable to the later application, but they serve, similar to the investigations in Chapter 2, for material screening. The investigations, which can be regarded as complements to the thermal conductivity measurements, show that the composition and the graphite mass fraction in the studied range are less important for the thermal performance. The improvement in turbulence, on the other hand, provides significant improvements.

Plate heat exchanger

To maximize the convective heat transfer coefficient, the embossed composite plates presented in Section 3.2.1 are used in the PHE. The chevron patterns applied to the plates promote swirl

or vortex flows as well as the disruption and reattachment of boundary layers [74–76]. In addition, the embossing increases the effective heat transfer surface. Overall, this leads to a significant increase in the overall heat transfer coefficient, as depicted in Fig. 3.15a. Considering constant Reynolds numbers and wall thicknesses, the use of profiled plates leads to at least a doubling of the *U* value. Significant advantages can also be seen in comparison with SS. However, this advantage decreases with increasing Reynolds number, since for SS most of the thermal resistance is due to the heat transfer fluid-wall. In the case of the patterned polymer composite, however, the largest fraction of thermal resistance is present in the wall even at a low Reynolds number of 1000, as shown in Fig. 3.15b. Yet this figure also demonstrates that, as assumed in the previous chapter, the patterning of the plates further pushes the potential of the polymer composites. Over 80% of the thermal resistance is found to be due to the 2 mm thick separating wall. Increases in the Reynolds number would mainly lead to an exorbitant increase in the pressure drop at this point. Further optimization can therefore mainly take place via a reduction in wall thickness (under consideration of the mechanical stability).

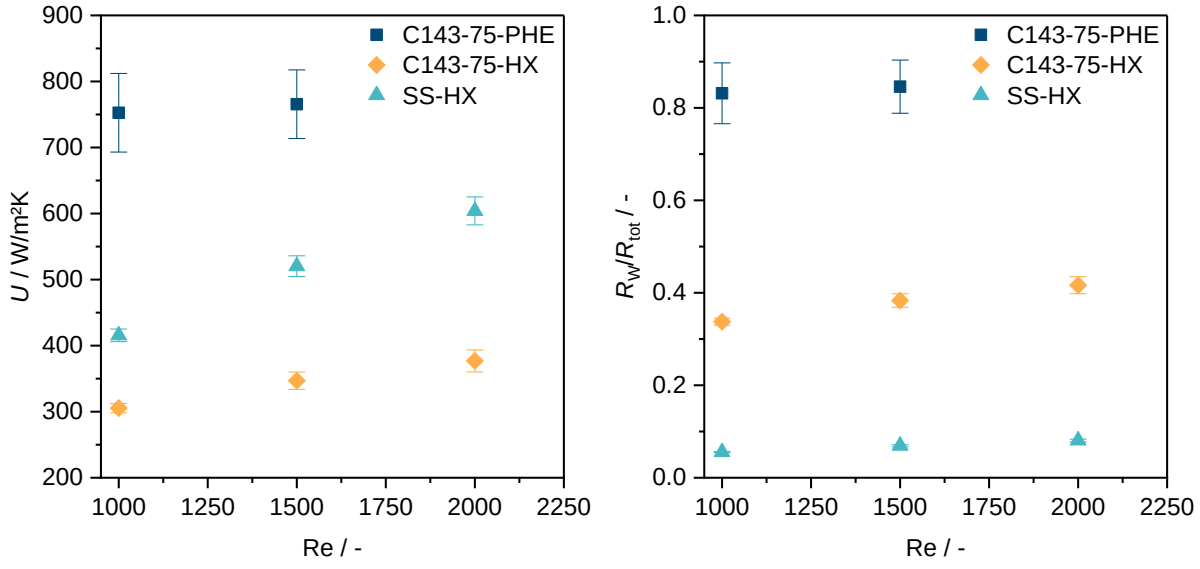

Fig. 3.15: Performance comparison between embossed and unembossed thermal plates. s = 2 mm; $T_{c,in}$ = 30 °C; $T_{h,in}$ = 70 °C. (a) Overall heat transfer coefficients. (b) Proportion of R_w to R_{tot}.

The bulk of the heat transfer measurements in the PHE were carried out primarily regarding model validation and consequently to enable a material comparison with established materials. The operating parameters were varied according to Tab. 3.2 and a total of 143 measuring points were determined. Most of the measurements are limited to PP-G sheets with a thickness of 2 mm. A part of the measurement points of the PP-G plates are shown exemplarily in Fig. 3.16 for one thermal plate and the co-current operation. Measurement data not shown in the main section are listed in the appendix for completeness. For a rough classification of the thermal

performance of the developed heat exchangers, the determined *U* values may be used. Overall, the thermal performance is influenced by end plates, pass arrangement, flow direction, number of transfer units and heat capacity flow rate ratio, but only the number of transfer units depend on the thermal plates used. It increases with increasing *U* value and heat transfer area for a given heat duty. Since the increase of the latter leads to a higher number of transfer units of the PHE (and thus to a higher efficiency) across all materials, only the *U* value is considered as the decisive performance parameter subsequently. According to the thermal conductivity measurements, the PP-G plates have a through-plane thermal conductivity of 1.81 W/mK. Thus, a theoretical *U* value of 905 W/m²K would be achievable (calculated under the assumption that the convective heat transfer coefficients are infinitely large). At Reynolds numbers of 1600 for the cold and hot flow, a *U* value of 842 W/m²K is already reached. The differences to the countercurrent flow are only minor due to small temperature differences between inlet and outlet. Here, the maximum measured *U* value is 856 W/m²K under identical test conditions. However, due to the flattening of the measured values towards high Reynolds numbers, it can also be seen that the values are limited by the thermal resistance of the wall. This is still comparatively high at 1.1 m²K/kW. In comparison, commercially available heat exchangers achieve heat transfer coefficients of up to 7500 W/m²K [20].

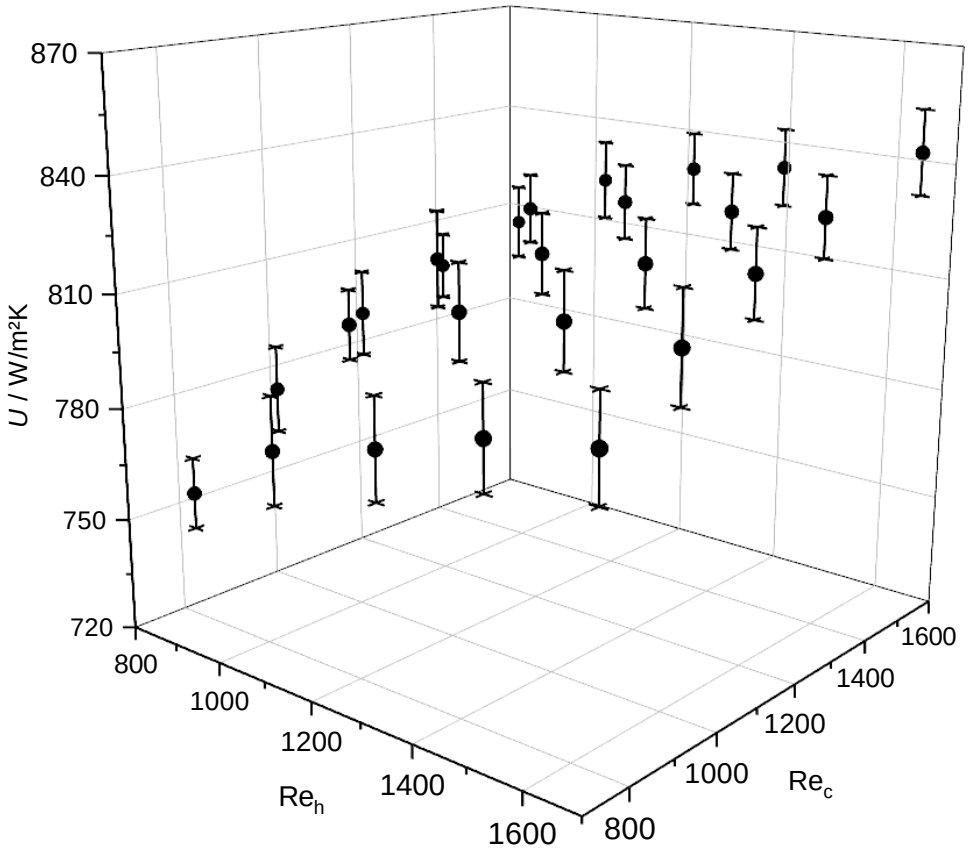

Fig. 3.16: Experimentally determined overall heat transfer coefficients. PP-G; Co-current; N_{tp} = 1; $T_{c,in}$ = 40 °C; $T_{h,in}$ = 80 °C.

The potential for improvement therefore lies in decreasing the thermal resistance in the wall, which can be achieved by further increasing the filling ratio (thermal conductivity increases, but from a certain loading onwards manufacturing problems arise) or, more simply, by reducing the wall thickness at the expense of mechanical stability. To compensate for this low mechanical stability, more robust polymers can be used as a matrix, such as PPS (2-3 times higher tensile strength compared to PP [28]). The effect of reducing the wall thickness for the PPS-G composite from 2.5 mm to 0.85 mm is shown in Fig. 3.17. For this composite, a thermal conductivity of 2.01 W/mK was determined for a wall thickness of 2.5 mm. With Reynolds numbers of 1600, overall heat transfer coefficients of 756 W/m²K and 1850 W/m²K respectively could be achieved for the PPS-G composite. Values that still do not come close to the performance of metallic plate heat exchangers. However, comparing the present results with the heat transfer coefficients of other experimental results of polymer heat exchangers shows comparable performance.

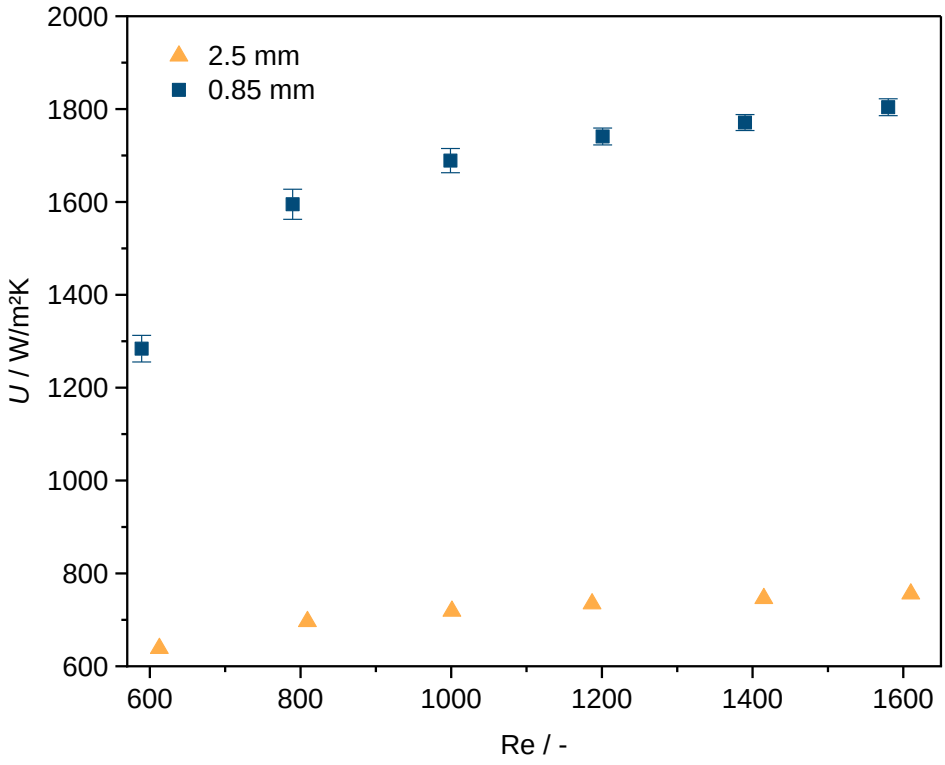

Fig. 3.17: Experimentally determined overall heat transfer coefficients. PPS-G; Countercurrent; N_{tp} = 1; $T_{c,in}$ = 40 °C; $T_{h,in}$ = 70 °C.

A comprehensive literature study of polymer heat exchangers was carried out by Chen et al. [25]. According to the authors, the focus of the investigations in recent years has been on the thermal performance of polymer hollow fiber heat exchangers. Despite the use of poorly thermally conductive polymers (thermal conductivity less than 0.4 W/mK), very high heat transfer coefficients are achieved by using hollow fibers (inner diameter less than 100 µm), ranging from 500 to a maximum of 2100 W/m²K for liquid-liquid heat transfer [4,5,77,78]. Due to a lack of experimental data, the maximum working pressure is questionable for this design, which will operate in the low-pressure range due to the low wall thicknesses. The exception could be the mechanically extremely stable but expensive PEEK. Simple replacement or addition of individual components (as is possible with the PHE) for cleaning or expansion is also not possible with this design. Studies on polymer-based plate heat exchangers are limited to those by Zaheed and Jachuck [79,80], whose PEEK-based cross-flow heat exchanger reaches overall heat transfer coefficients up to 900 W/m²K at a high maximum pressure of 10 bar. The comparison thus shows a superior thermal performance of the heat exchangers developed here when using low wall strengths.

However, for a direct comparison (same geometry, same operating conditions) between the polymer composite PHE and metallic PHEs, the model described in Section 3.2.3 must be used as shown in the following section.

An effect that became apparent in the fouling experiments when using the developed materials and caused a considerable drop in thermal performance is the formation and adhesion of air bubbles on the heat-transferring surfaces. The reason for this is a locally supersaturated liquid at the sample surface and is adressed in detail in Section 4.3.1. However, it was only observed on polymeric surfaces, but not on metallic surfaces. Therefore, it should be checked whether bubble adhesion also occurs in the developed polymer composite based PHE. Fig. 3.18 shows the comparison of measured heat transfer rates for a series of experiments performed with degassed and non-degassed water. To force bubble formation, low Reynolds numbers (200 – 600) were chosen.

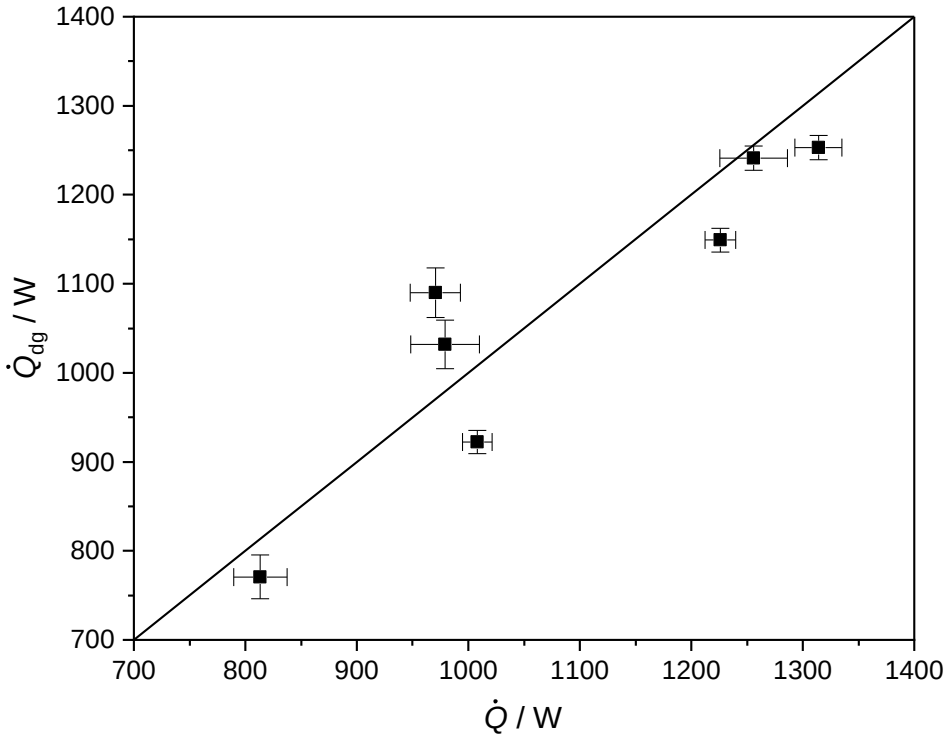

Fig. 3.18: Parity plot for the influence of degassed fluid on the heat transfer in the PHE. N_{tp} = 7; $T_{c,in}$ = 40 °C; $T_{h,in}$ = 70 °C. Countercurrent flow. Re = 200 - 600.

It is evident that there is no significant difference between the use of degassed and non-degassed water. The generation of swirl or vortex flows in the corrugated PHE thus ensures that either no air bubbles are generated (due to lower wall temperatures and thus lower supersaturation) or that these can be effectively removed before a negative influence on the heat transfer arises.

3.3.2 Plate heat exchanger modeling

CFD-simulation based Nusselt correlation

Tab. 3.6 shows the correlation matrix determined based on the data from the CFD-simulations. The simulation data can be found in Table A.5 in the appendix. Since the Prandtl number Pr is temperature sensitive due to its dependence on viscosity, the correlation matrix does not include the effect of the temperature on the Nusselt number. However, this results in a correlation coefficient $r_{Pr,T} = r_{T,Pr} \approx -1$ for the dependence of the Prandtl number on temperature. Since this would lead to multicolinearity in the modeling, the temperature is not considered herein. The correlation matrix shows that the dependence of the Nusselt number on the Reynolds number results to be the largest. Thus, a correlation coefficient of 0.95 is obtained for both the hot and the cold fluid. For the Prandtl number, a moderate dependence is obtained. The correlation coefficient for this parameter is in the range $0.22 \leq r_{Pr,Nu} \leq 0.33$. For the remaining varied parameters, there is almost no dependence, and the correlation coefficients all result in $|r| \leq 0.2$. In particular, the thermal conductivity of the plate material used has hardly any influence on the Nusselt number. This indicates that a plate heat exchanger made of composite material has almost the same heat transfer coefficient as a plate heat exchanger made of SS. Similarly, it can be seen that the effect of plate spacing on Nusselt number is minor. The plate number shows a small effect on the Nusselt number of the cold fluid. This can be explained by plate end effects (the circumstance that the two outer plates in the PHE do not transfer any heat), since with an increase in the number of plates, the Nusselt number of the cold fluid decreases, with otherwise identical conditions. However, the Nusselt number of the hot fluid remains almost unchanged. This can be explained by the fact that the number of channels with hot fluid in the conducted simulations is greater than with cold fluid and the plate end effect is therefore less significant.

Tab. 3.6: Correlation matrix for the determination of the dependence of the Nusselt number on other parameters.

	Nu_c	Nu_h	s	λ_w	Re_c	Re_h	Pr_c	Pr_h	ΔT	N_{tp}
Nu_c	1.00	0.01	0.02	-0.09	0.95	0.01	0.22	0.08	0.07	-0.11
Nu_h	0.01	1.00	0.05	-0.06	0.01	0.95	0.04	0.33	-0.25	0.01
s	0.02	0.05	1.00	-0.05	-0.05	-0.05	0.04	0.15	-0.10	-0.07
λ_w	-0.09	-0.06	-0.05	1.00	-0.03	-0.03	0.02	0.09	-0.06	-0.04
Re_c	0.95	0.01	-0.05	-0.03	1.00	0.04	0.02	0.09	-0.06	-0.04
Re_h	0.01	0.95	-0.05	-0.03	0.04	1.00	0.02	0.09	-0.06	-0.04
Pr_c	0.22	0.04	0.04	0.02	0.02	0.02	1.00	0.05	0.56	0.03
Pr_h	0.08	0.33	0.15	0.09	0.09	0.09	0.05	1.00	-0.80	0.12
ΔT	0.07	-0.25	-0.10	-0.06	-0.06	-0.06	0.56	-0.80	1.00	-0.08
N_{tp}	-0.11	0.01	-0.07	-0.04	-0.04	-0.04	0.03	0.117	-0.08	1.00

Overall, the correlation matrix indicates a dependence of the Nusselt number on the Reynolds number and the Prandtl number. This is in agreement with known correlations as described in Section 3.2.3, so that the proposed model (Eq. 3.12) is applicable. For this purpose, the parameters of the equation are fitted to the simulation data, which results in the following Nusselt correlation:

$$\mathrm{Nu} = 0.284 \cdot \mathrm{Re}^{0.587} \cdot \mathrm{Pr}^{0.784} \tag{3.18}$$

Fig. 3.19 shows the simulation data along with the correlation based on it. The Nusselt number increases with both the Reynolds number and the Prandtl number. This can be explained by the dependence of the heat transfer coefficient on the flow boundary layer and the thermal boundary layer. As the flow boundary layer increases and the thermal boundary layer decreases, the heat transfer coefficient and thus the Nusselt number increase. Furthermore, it is evident that the simulation data for different Reynolds numbers as well as Prandtl numbers hardly deviate from the plotted plane. This is also reflected in the coefficient of determination, having the value $R^2 = 0.97$. The scatter of the data is consequently very well represented by the model dependent on the Reynolds number and Prandtl number. In the region Re = 1000 and Pr = 4.58 - 3.32, slight deviations are apparent. In this area, the plate spacing was varied, but the relative deviations are small, < 5%. Moreover, like the correlation coefficient $0.02 \leq r_{s,\mathrm{Nu}} \leq 0.05$, the data do not indicate a direct correlation of plate spacing and Nusselt number.

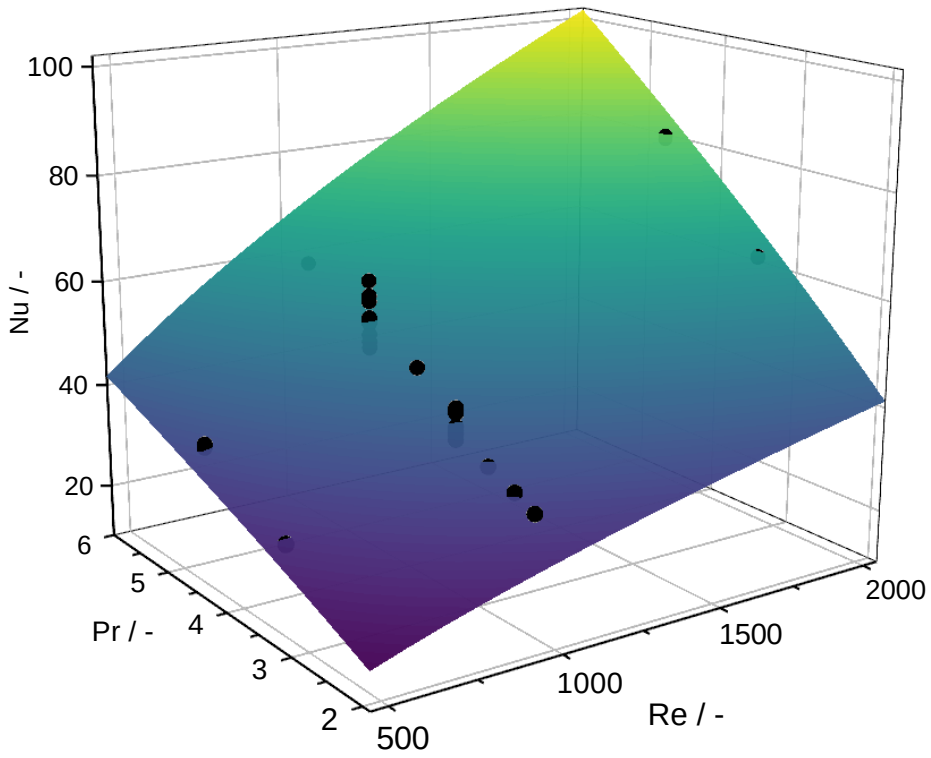

Fig. 3.19: Nu plotted against Re and Pr. Data points: CFD simulations (Table A.1); Plane: Correlation after parameter fitting.

Model validation

For the validation of the model described in Section 3.2.3, the through plane thermal conductivity determined by laser-flash was used initially. The results of the simulations are exemplarily shown for the PP-G composite with a thermal plate number of one in Fig. 3.20. Thereby, the simulations resulting in the upper plane are based on the correlation given in this thesis and the simulations resulting in the lower plane are based on the correlation according to Muley and Manglik. At first sight, the correlation given in this work seems to fit the measured values much better, whereas a systematic deviation arises with the correlation according to Muley and Manglik. This systematic deviation, due to the underestimation of the measured values, cannot be attributed to a flow maldistribution or poorer heat transfer coefficients in the inlet and outlet areas (flow distributors) of the developed PHE since the measured values would otherwise be overestimated by the simulation. In principle, only an underestimation of the convective heat transfer coefficients (h) by the correlation is then conceivable. But not only the correlation according to Muley and Manglik applied in Fig. 3.22, but also the two other correlations taken from the literature qualitatively show the same systematic deviation from the measured values. Consequently, it can also be excluded that the correlations are affected negatively by the endplate effect. In the experimental calculation of h, which is conducted indirectly by measuring

U, if the number of thermal plates is insufficient, the end-plate effect causes an overestimation of *h*. The reason for this is that the end plates in the experiment cannot be assumed to be completely adiabatic. However, above a sufficiently large number of plates, the end-plate effect becomes negligible [81,82].

However, the correlation of this work also leads to a systematic deviation that only becomes apparent upon detailed analysis. The slope of the measured values is not well represented by the correlation, which leads to an overestimation of the measured values at low Reynolds numbers and to an underestimation at high Reynolds numbers. This smaller slope of the plane compared to the experimental data implies that the thermal resistance of the convective heat transfer is underestimated by the simulation. The higher the convective heat transfer coefficient at constant thermal resistance of the wall, the flatter the plane will become. Consequently, the correlation presented in this work overestimates the Nusselt number or convective heat transfer coefficient.

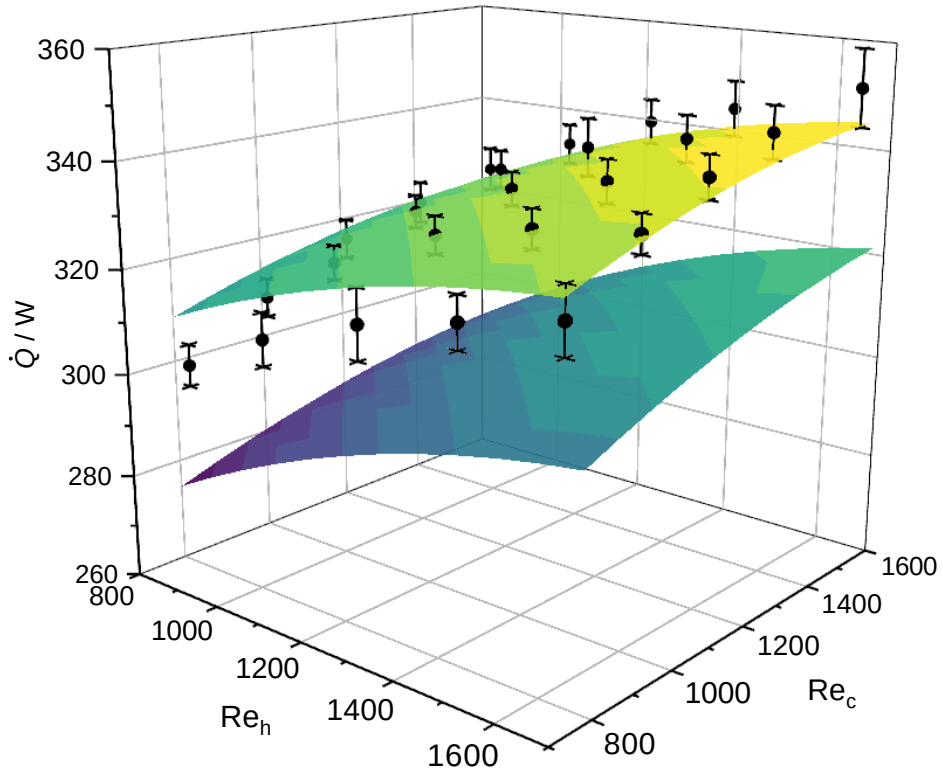

Fig. 3.20: Measured and simulated heat transfer rates. PP-G; Co-current; N_{tp} = 1; $T_{c,in}$ = 40 °C; $T_{h,in}$ = 80 °C. Simulation with λ = 1.81 W/mK. Upper plane: correlation according to Eq. 3.18. Lower plane: Correlation according to Muley and Manglik (see Tab. 3.3).

The plot of all experimentally determined values against the simulated values in Fig. 3.21 confirms this assumption. In this graph, an increasing *U* value is equivalent to an increasing con-

vective heat transfer coefficient or an increasing Reynolds number. Assuming that the simulations overestimate the heat transfer coefficient, the systematic difference should become negligible at very high Reynolds numbers ($\alpha \rightarrow \infty$, determining thermal resistance lies in the wall) and increase with decreasing Reynolds number (determining thermal resistance lies in the convective heat transfer). And this is precisely what can be found in Fig. 3.21. The overestimation of the heat transfer originates in the fact that only one section of the PHE was simulated. Moreover, a section was chosen that was located in the area of the chevron pattern of the PHE, which are designed for a maximum heat transfer coefficient. The flow distributors, where lower convective heat transfer prevails, as well as possible flow maldistributions are not considered in this case. Consequently, a trustworthy Nusselt correlation based on CFD simulations would have to cover the whole heat exchanger or at least all representative parts. Furthermore, it can be seen that the deviation reverses with increasing Reynolds number (experiment yields higher values than simulation). This can only be explained by the fact that the thermal resistance in the wall is lower than assumed, i.e., the thermal conductivity must be higher than estimated in the simulations. A fact that is also consistent with the divergence of the correlations found in the literature (shown in Fig. 3.21 for the correlation according to Wanniarachchi). However, for the latter, the heat transfer coefficient seems to be well estimated since the slope of the data points corresponds to the angle bisector. This is logical, since the correlations in the literature are based on experimental data, which in turn take into account the heat transfer in the flow distributors.

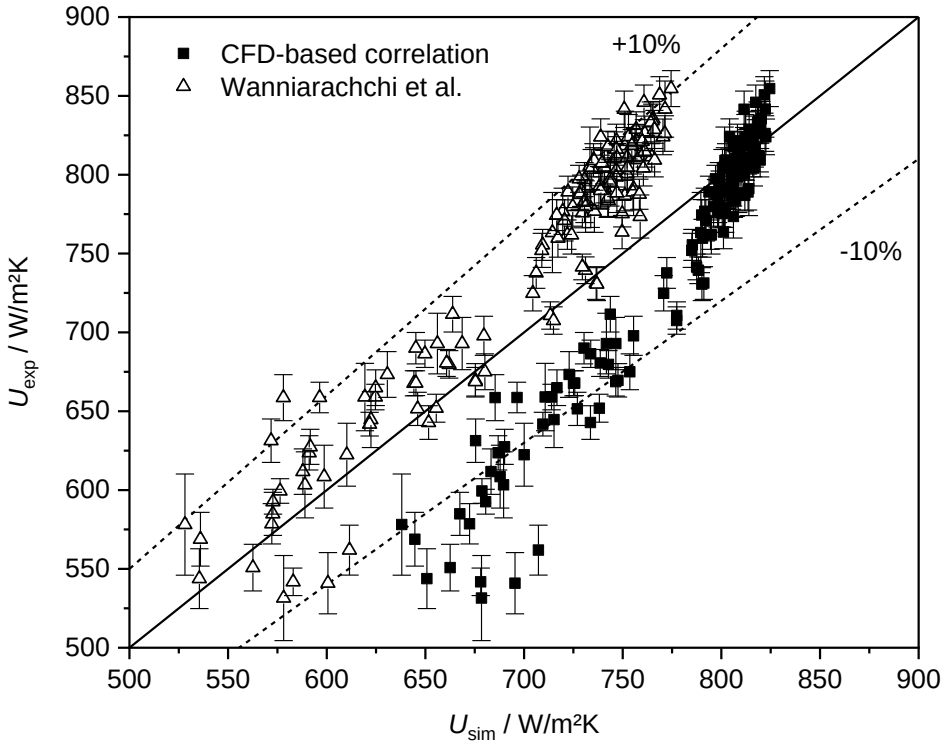

Fig. 3.21: Comparison between measured and simulated overall heat transfer coefficients. PP-G. λ = 1.81 W/mK.

The reason for the deviations must lie in the anisotropic properties of the composite plates produced. The sheet extrusion of the materials ensures a stretching of the (non-spherical) graphite particles in the plane. This results in much higher in-plane thermal conductivities, which was already discussed in Section 2.3.2. The through-plane thermal conductivity relevant for heat transfer is, as described above, only 1.81 W/mK. However, this measurement is based on the unembossed plates. After embossing, the measurement of the thermal conductivity relevant for heat transfer is impossible. Consequently, the stretching during embossing of the sheets could lead to an increase in the effective thermal conductivity. Fitting the thermal conductivity in the model to the experimental data finally ensures an exact match between model and experiment for the correlations taken from the literature, as shown in Fig. 3.22. Depending on the underlying correlation, however, the thermal conductivities must be adjusted to different values, always requiring a significantly higher value than the measured one (1.81 W/mK). Thus, the increase in thermal conductivity for the PP-G composite is between 7.7 and 16 % (see Tab. 3.7). This is quantified by the reduction of the mean average percentage error (MAPE) by adjusting the thermal conductivity. Only the adjustment of the thermal conductivity using the CFD simulation-based correlation does not lead to better agreement due to the already discussed overestimation of the convective heat transfer coefficient. Therefore, this correlation will not be considered in further discussions.

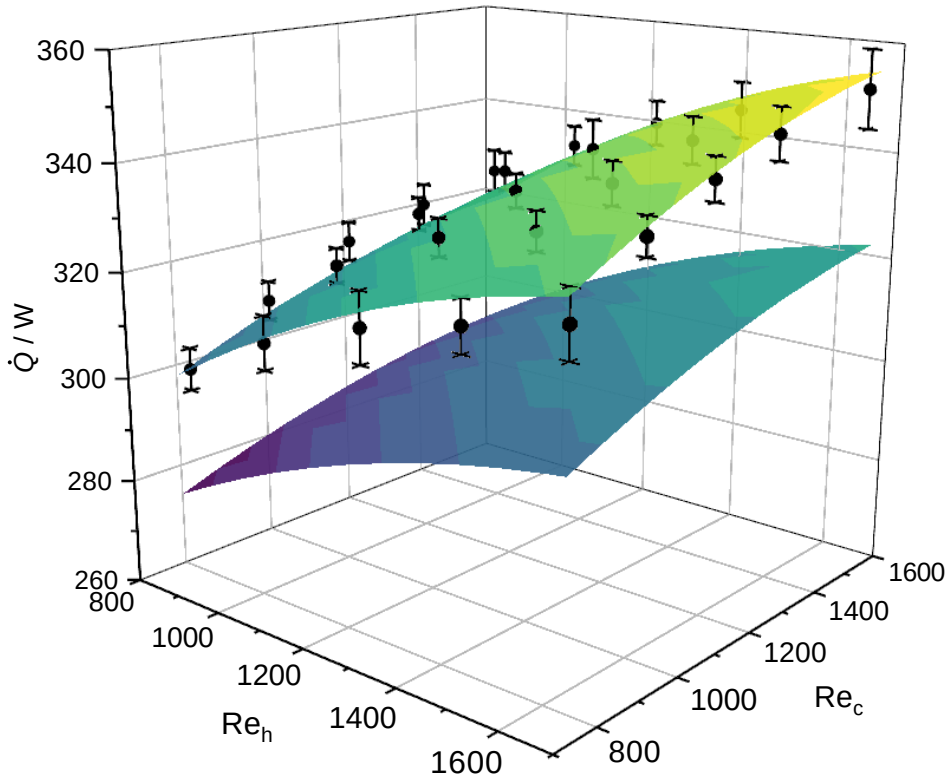

Fig. 3.22: Measured and simulated heat transfer rates. PP-G; Co-current; N_{tp} = 3; $T_{c,in}$ = 40 °C; $T_{h,in}$ = 80 °C. Lower plane: Simulation with λ = 1.81 W/mK. Upper plane: Simulation with λ = 2.05 W/mK. Correlation according to Muley and Manglik (see Tab. 3.3).

After the adjustment, all correlations provide good fits to the experimental data. However, the correlation according to Muley and Manglik is only applicable for Reynolds numbers greater than 1000, which is why only half of all data collected could be compared with it. This also explains the apparently best agreement of this correlation. For all subsequent modeling, the Wanniarachchi correlation is used, since it performs about as well as the Kumar correlation, but offers greater flexibility due to the geometry parameters that can be implemented (see Tab. 3.3).

Tab. 3.7: Adjusted thermal conductivities and goodness of fit of the simulations.

Correlation	Adjusted λ W/mK	Increase in λ	MAPE U λ = 1.81 W/mK	MAPE U Adjusted λ
Muley and Manglik	2.05	13.3 %	8.93 %	1.44 %
Wanniarachchi	1.95	7.7 %	5.85 %	3.11 %
Kumar	2.1	16.0 %	9.72 %	2.59 %
CFD-based (this work)	1.81	0 %	5.82 %	-

That the above-mentioned apparent increase in thermal conductivity by embossing is not a measurement error of the thermal conductivity of the PP-G composite is shown by the studies

on the PPS-G composites. Two different wall thicknesses were investigated here, with the thermal conductivity determined for a 2.5 mm thick, unembossed sheet and given as 2.01 W/mK. According to the results of the parameter adjustments, as shown in Fig. 3.23, the more the original plate is compressed, the greater the increase in the effective thermal conductivity.

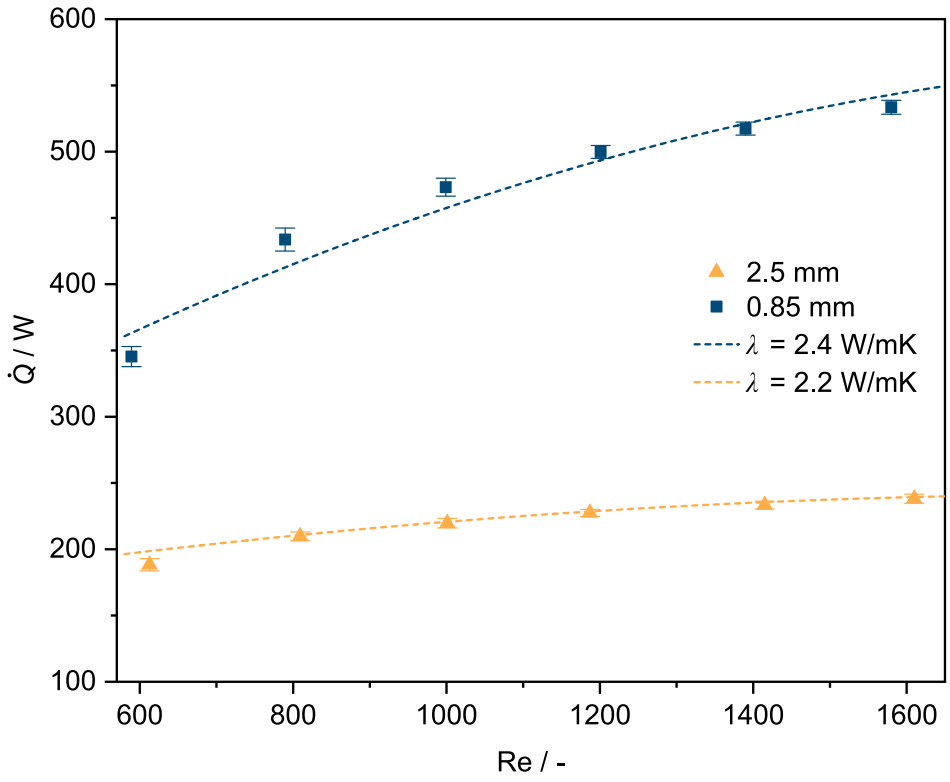

Fig. 3.23: Measured and simulated heat transfer rates. PPS-G; Counter-current; N_{tp} = 1; $T_{c,in}$ = 40 °C; $T_{h,in}$ = 70 °C. Correlation according to Wanniarachchi.

This results in the 2.5 mm thick plate having the best agreement between model and experiment by considering a thermal conductivity of 2.2 W/mK and the 0.85 mm thick plate by considering a thermal conductivity of 2.4 W/mK for the correlation of Wanniarachchi. To further confirm these findings, computed tomography (CT) scans of the cross-sectional area of embossed samples were taken, as shown in Fig. 3.24. It is clearly seen that the particles are aligned along the developed length. However, this may already be sufficient for the increase in thermal conductivity, as this is already equivalent to a (partly) superposition between the in-plane and through-plane direction. Furthermore, particle agglomerations are formed which can act as additional thermal bridges.

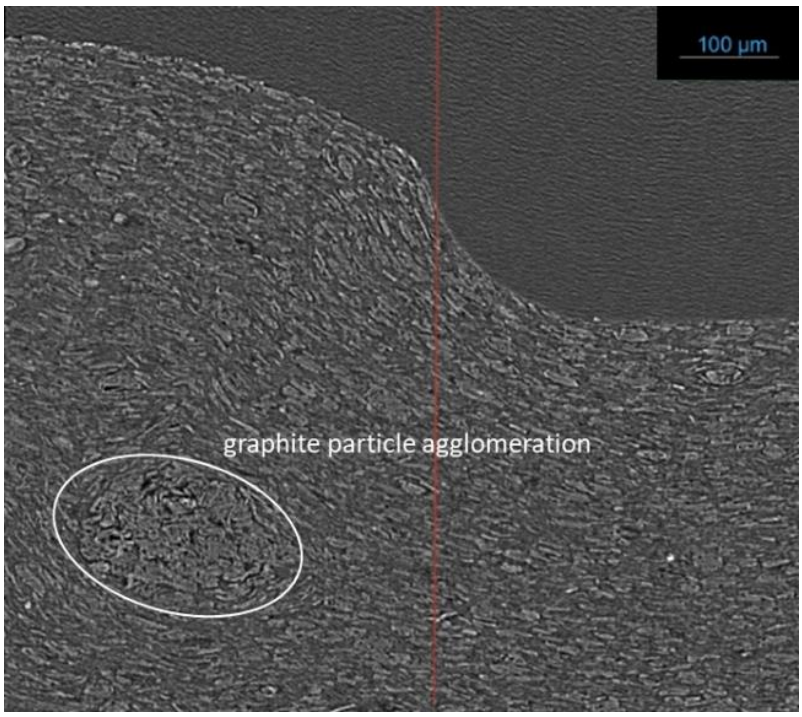

Fig. 3.24: CT scan of the cross-section of an embossed polymer composite plate.

Overall, the parameter fitting leads to a very good agreement between model and experiment. This is additionally illustrated in a parity plot for all measured and simulated overall heat transfer coefficients in Fig. 3.25. Most of the measured values are within an uncertainty of 5 %. Except for a few outliers, all measured values are within an uncertainty of 10 %.

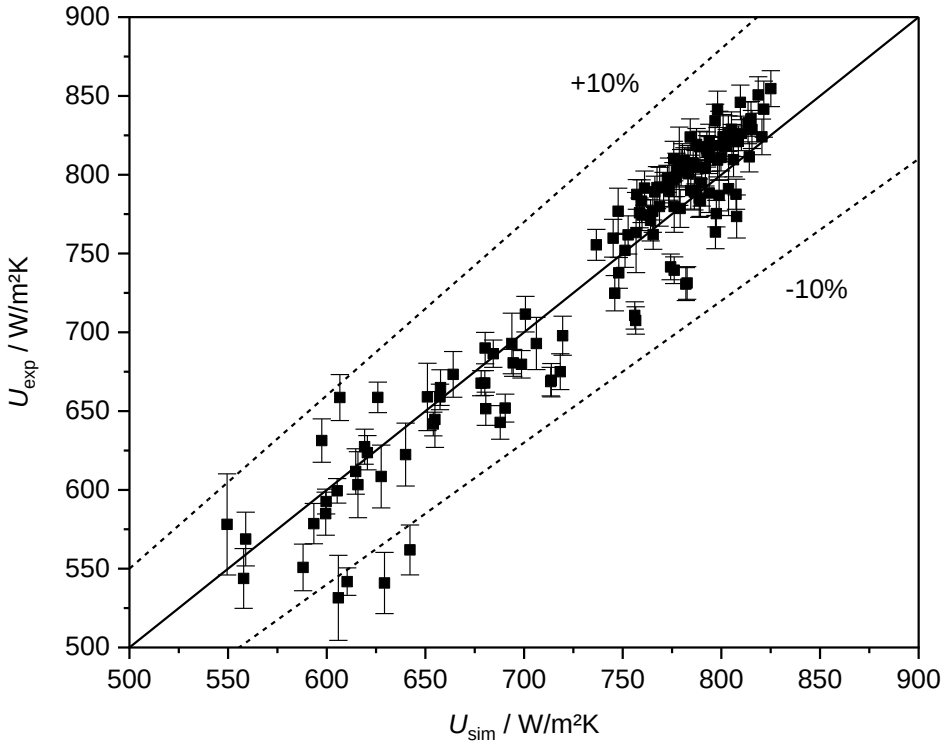

Fig. 3.25: Comparison between measured and simulated overall heat transfer coefficients. PP-G; Thermal conductivity adapted according to Tab. 3.7; Correlation according to Wanniarachchi.

3.3.3 Comparison with conventional materials

Applying the validated model for calculating the performance of polymer composite plate heat exchangers enables the performance comparison with conventionally used materials for heat transfer of corrosive fluids, like stainless steel, Hastelloy or titanium. Even if the polymer composites have economic advantages over the materials mentioned, a direct performance comparison would be in favor of the metals as depicted in Fig. 3.26 (PP-G vs. SS). It shows *U* values simulated with the validated model as a function of the two parameters affecting *U* primarily (Re and *s*). The simulations were performed with only one thermal plate, since in this case no end-plate effect exists (heat is transferred between the two flows in true counter-current and co-current flow, respectively [20]) and therefore cannot influence the comparison. The comparison in Fig. 3.26 covers a large operating and application range. It shows that for every point of the span, the *U* value of stainless steel exceeds that of PP-G, with the difference increasing with increasing Reynolds number. The reason is again the significantly higher thermal resistance of the composite wall, which becomes more pronounced with increasing *h*, as already discussed in previous sections.

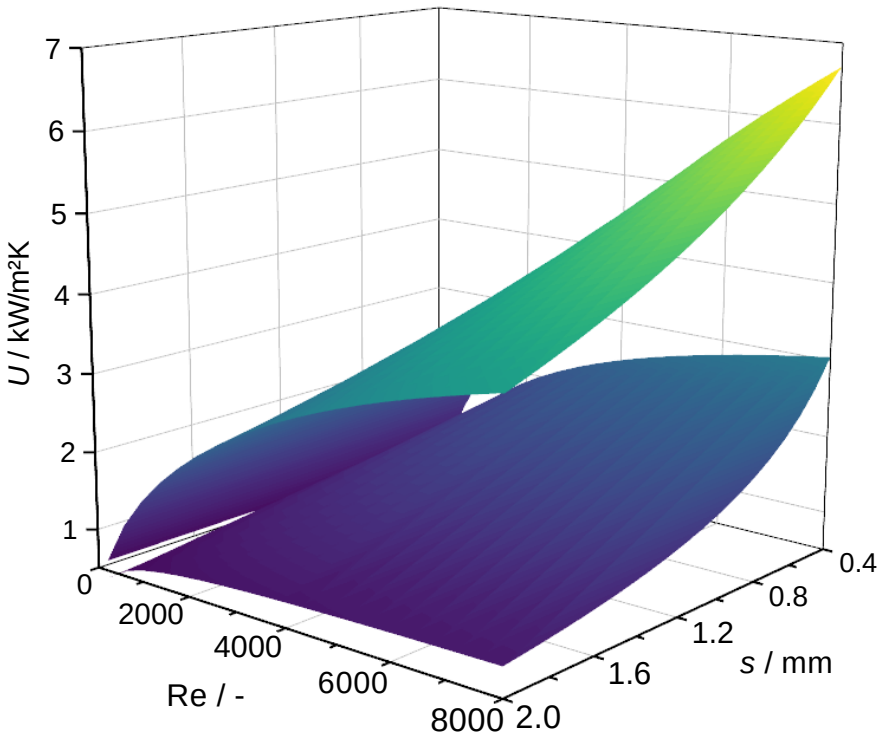

Fig. 3.26: Simulated *U* values for ideal countercurrent flow (N_{tp} = 1); Re_c = Re_h; Geometry parameters according to Tab. 3.4; Nusselt correlation according to Wanniarachchi; Upper plane: SS; Lower plane: PP-G.

However, a detailed comparison becomes necessary when the considerable difference in density of the materials is taken into account and equal heat transfer masses are set as a boundary

condition. For comparison, the density of the PP-G studied is 1.65 g/cm³, whereas the density of SS is 8 g/cm³ (a factor of 4.8). Comparing the same materials based on *UA* as the comparative parameter reverses the result, as shown in Fig. 3.27. The area of stainless steel was standardized to 1 m². This results in a heat transfer area of 4.8 m² for PP-G under the above boundary condition.

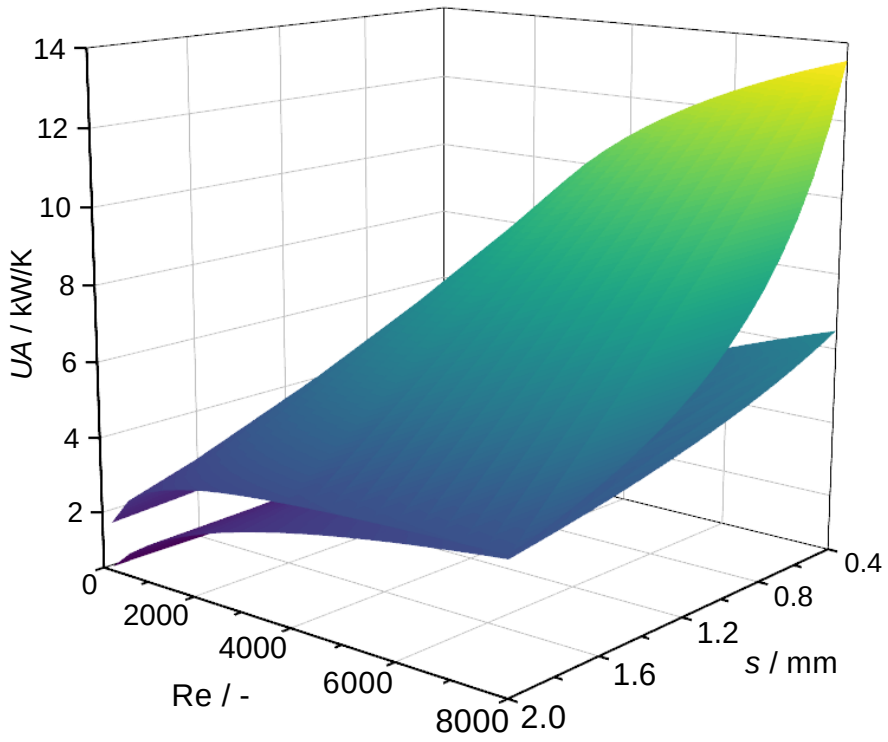

Fig. 3.27: Simulated *U* values for ideal countercurrent flow (N_{tp} = 1); Re_c = Re_h; Geometry parameters according to Tab. 3.4; Nusselt correlation according to Wanniarachchi; Upper plane: PP-G; Lower plane: SS.

However, this ratio only applies if the number of plates is sufficiently large, since the weight of the end plates must also be considered. Furthermore, this comparison does not account for the better mechanical stability of SS compared to PP-G, which is why a fairer comparison is attempted subsequently.

Even if, due to the inferior mechanical stability of the composites, higher wall thicknesses should be adopted (in the example case below wall thicknesses of 1 mm for SS and 1.5 mm for PP-G are assumed), significantly higher heat transfer areas result regarding PP-G. Fig. 3.28 therefore shows the simulated performance comparison between PP-G and stainless steel with *UA* as the comparison parameter over a wide range of Reynolds numbers (200-8000). For this purpose, specific numbers of thermal plates were assumed (based on density ratio and wall thickness ratio: 7 for stainless steel and 27 for PP-G).

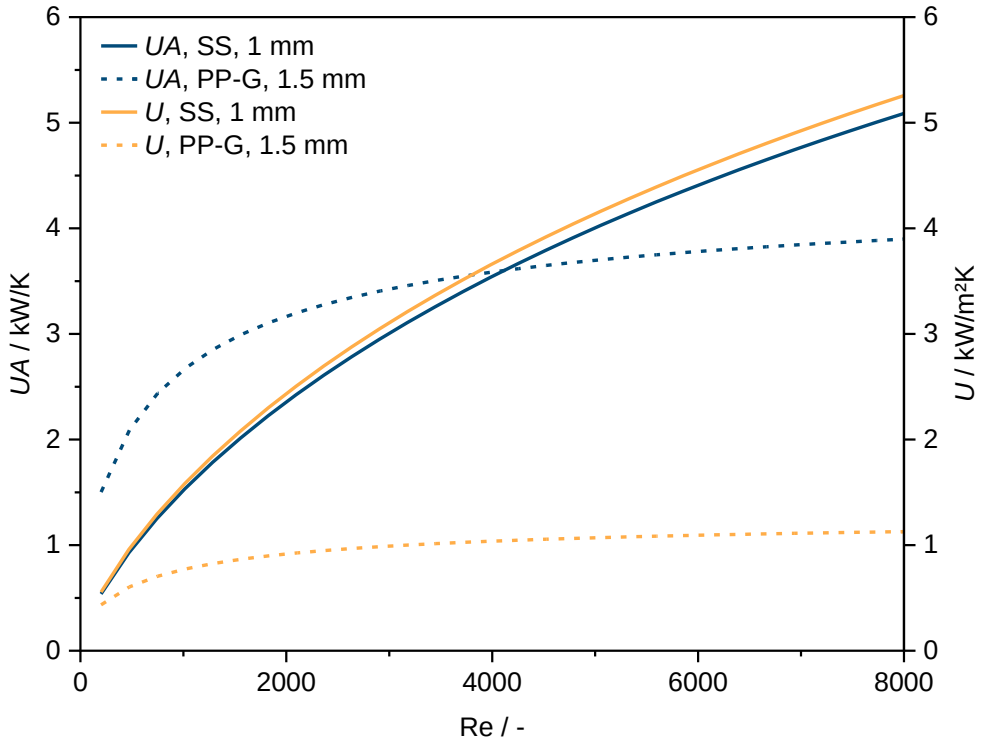

Fig. 3.28: Simulated *U* and *UA* values for constant Reynolds numbers; $Re_c = Re_h$; Geometry parameters according to Tab. 3.4; Nusselt correlation according to Wanniarachchi.

In this scenario, only the generation of high Reynolds numbers (> 4000) leads to SS being preferable to PP-G. This also represents the application limit of the polymer composite, since above this Reynolds number there is no noteworthy increase in performance. This is due to the relatively high thermal resistance of the polymer composite wall, which has a limiting effect above this threshold. In addition, the higher pressure losses that occur at high Reynolds numbers would be an additional stress on the material. At a Reynolds number of 8000, the performance of SS exceeds that of the composite by 30.5%, although correspondingly higher pressure losses would have to be accepted.

However, the comparison with equal Reynolds numbers results in different mass flows in the heat exchangers (due to the higher number of plates chosen for the polymer composite and therefore a larger cross-sectional area). Thus, for the purpose of completeness, Fig. 3.29 shows the comparison with constant mass flow rates, corresponding to the heating or cooling of a certain amount of fluid. If the curve of PP-G is below that of SS, this is equivalent to the fact that a larger area (or larger PHE mass) is required for the same heat duty and vice versa. Thereby, the mass flows of the cold fluid $\dot{m}_c$ were chosen to cover the same Reynolds number range as before (200-8000) with respect to SS, resulting in lower Reynolds numbers regarding

PP-G (60 - 2500). The mass flows of the hot fluid $\dot{m}_h$ were chosen to cover low and high Reynolds numbers (1000 and 8000, respectively) with respect to SS, resulting in Reynolds numbers of 300 and 2500 regarding PP-G.

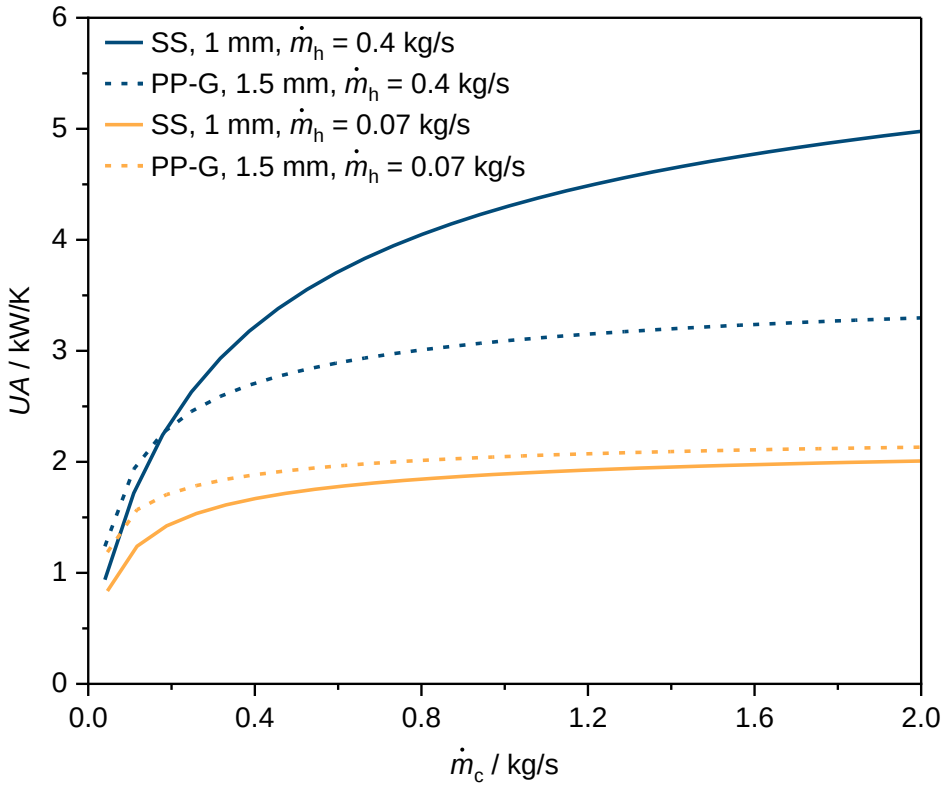

Fig. 3.29: Simulated *UA* values for constant mass flows; Geometry parameters according to Tab. 3.4; Nusselt correlation according to Wanniarachchi.

Again, it can be seen that the polymer composite has advantages over SS at low mass flow rates. At a hot fluid mass flow rate of 0.16 kg/s, more heat would be transferred by using the polymer composite. In this case, the convective heat transfer on the hot fluid side is the limiting factor for both materials. In the case of high mass flows ($\dot{m}_h$ = 1.18 kg/s and $\dot{m}_c$ = 2 kg/s), there is a performance difference of 50 %.

Nevertheless, considering its low density, the polymer composite offers comparable thermal performance compared to its metallic alternatives over a wide range of operating conditions.

4 Crystallization Fouling

4.1 Theory

Fouling is defined as the accumulation of undesirable substances on a surface, in the context of this work specifically on heat exchanger surfaces. It reduces the effectiveness of a heat exchanger by decreasing heat transfer and increasing pressure drop by constricting the cross-sectional area. Fouling can significantly affect the design of a heat exchanger and consequently the amount of material used in its fabrication (oversizing) as well as the performance between cleaning intervals. Consequently, fouling causes a tremendous economic loss as it directly affects the initial cost, operating cost and performance of the heat exchanger [23,83]. In heat exchangers, fouling is caused by substances dissolved or suspended in industrial fluids or micro- respectively macro-organisms [84]. The formation of a fouling layer on a heat transfer surface results in an additional thermal resistance R_f which lowers the overall heat transfer coefficient as follows.

$$\frac{1}{U} = \frac{1}{h_c} + \frac{s}{\lambda} + \frac{1}{h_c} + R_f \tag{4.1}$$

Depending on the cause of fouling, it is classified into the following mechanisms [85]:

- Crystallization fouling
- Particulate fouling
- Chemical reaction fouling (including corrosion)
- Biological fouling

whereby, according to Steinhagen et al. [23], after corrosion fouling, most heat exchangers are affected by crystallization fouling (about 30%, a percentage based on data from 200 companies in New Zealand). Furthermore, in industrial applications, overlapping of different fouling mechanisms may occur, affecting each other [84]. On the polymer composite surfaces investigated in this thesis, corrosion fouling is excluded due to the properties of the material. Therefore, crystallization fouling is investigated to screen the composites, which will be described subsequently in detail. For more information regarding the remaining fouling mechanisms, please refer to the literature [85].

The deposition of crystals on heat exchanger surfaces is common, especially in aqueous systems. Examples include cooling water circuits, where deposits of hardness salts (such as calcium carbonate) occur on heat transfer surfaces and the evaporation of solutions, where the

surface on which the boiling takes place is prone to fouling by crystallization. In general, supersaturation with respect to the prevailing temperature is a necessary condition for crystallization to occur on surfaces. In the case of a saturated solution of salts with normal solubility (e.g., NaCl), precipitation will occur when the solution is cooled down. For saturated solutions of salts with inverse solubility (e.g., $CaCO_3$), precipitation will occur when the solution is heated. Thereby, the highest or lowest temperature in a heat exchanger associated with the solution is at the liquid-solid interface (heat transfer surface). In the presence of (local) supersaturation, the formation of crystal nuclei and crystallites occurs followed by the crystal growth on the surface [86].

Technically, the fouling process is divided into the subsequent five phases [83], applying to all of the previously mentioned fouling mechanisms.

1. Initiation
   The nucleation necessary for deposit formation ensures that the heat transfer coefficient of the initially clean heat transfer surface remains. This initial phase can last up to several days.

2. Transport
   Diffusive mass transport of at least one key component from the bulk flow to the heat transfer surface

3. Attachment
   Deposition or reaction of the substance forming the deposit (e.g., $CaCO_3$) of the fouling controlling species on the surface.

4. Removal
   Depending on the strength of the deposited layer, a more or less pronounced erosion due to the fluid flow is obtained. The mechanism of this erosion is assumed to be the breaking off of entire deposit pieces due to defects in the deposit, the shear forces of the flow or the occurrence of turbulent vortices at the heat transfer surface. Furthermore, there are various mechanisms that do not cause the removal of already formed deposits, but rather an autoretardation of the transport process, such as the decrease in temperature at the deposit-fluid phase boundary due to the growing fouling layer.

5. Aging
   Aging processes can increase the strength of the deposit (e.g., polymerization, regression of defects) or weaken it (e.g., degradation of bio-deposits).

The initial formation of crystal nuclei, which always represent the beginning of the formation of a fouling layer, initially provide a delay (depending on material and operating parameters),

as described above. If the first crystals start to grow in the viscous sublayer of the flow, this results in additional thermal resistance on the one hand, but also in an improvement of the convective heat transfer on the other hand. If the latter effect predominates, negative measured fouling resistances occur, which usually become positive again after a certain time due to further crystal growth. The time period from the beginning of the fouling process until the fouling resistance again becomes zero is called the roughness delay time (see Fig. 4.1).

Based on the fouling mechanisms and sub-steps described above, the possibilities for the temporal progression of fouling shown in Fig. 4.1 result, which are observed in practice [87]. If there is no constant heat flux condition but constant wall temperatures, the formation of the fouling layer provides a decrease in temperature of the liquid-solid interface which has a direct effect on the fouling process. The resulting fouling rate can then range from linear to asymptotic, even if there is no removal rate under the given operating conditions.

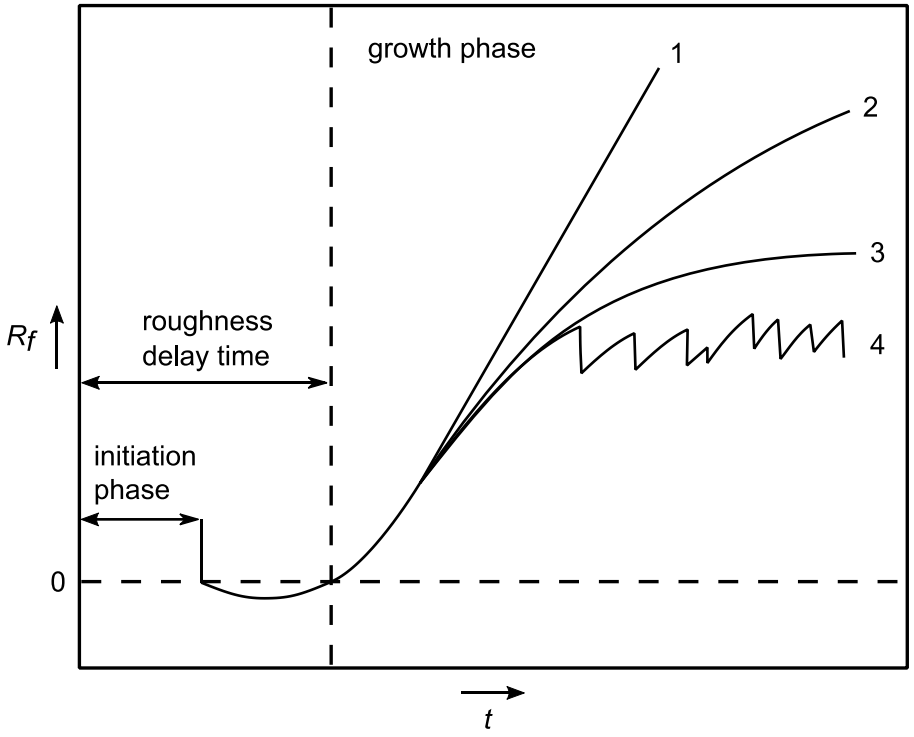

Fig. 4.1: Characteristic fouling resistance curves (based on Bucko [88] and Bansal [89]). (1) Linear increase, (2) decreasing fouling behavior, (3) asymptotic fouling behavior, (4) sawtooth profile.

4.1.1 Influence of process conditions on crystallization fouling

The deposition rate during crystallization fouling can be simplistically attributed to the following steps: transport of ions from the bulk to the surface, surface integration of the material, and

removal of the fouling layer from the surface, which are dependent on both crystallization kinetics (single salt precipitation or mixed salt precipitation) and flow conditions in the heat exchanger. Due to the complexity of the crystallization mechanism and the variety of heat exchangers, numerous authors have therefore made efforts to describe fouling processes mathematically [89–93]. Overall, the following influencing factors can be derived with regard to crystallization fouling:

- Fouling increases linearly with increasing foulant bulk concentration.
- The surface integration is strongly temperature dependent (increases with temperature) and is usually described via an Arrhenius approach.
- Improved mass transfer favors fouling up to a certain point where surface integration becomes limiting.
- The residence time of the liquid on the wall influences the probability that the fouling material adheres to the surface.
- The removal of the deposits from the surface depends on the shear strength of the fouling layer (or adhesion) and the shear stress of the fluid flow.

Furthermore, it must be added that the formation of crystals is also strongly dependent on the surface itself, which will be discussed in more detail below based on the materials studied. Briefly, sites on the heat exchanger surface support the formation of crystals, but also surface energy effects determine crystal growth [86].

4.2 Material and Methods

4.2.1 Materials and preparation

The same materials were used as those investigated in Chapters 2 and 3. See Sections 2.2.1 and 3.2.1 respectively for the preparation.

4.2.2 Experimental set-up

The fouling experiments were carried out at various operating conditions in the screening apparatus shown schematically in Fig. 3.8. The setup has already been described in detail in Section 3.2.2, so only the adjustments for the fouling studies are addressed below. In addition to the two test units already described (PHE and HX1, see Fig. 3.6 and Fig. 3.7), another one is used for the fouling investigations, shown schematically in Fig. 4.2. This is hereinafter referred to as HX2 and is also operated in countercurrent flow for the fouling studies.

It has a heat transfer area of 32 cm² and the liquid ports are aligned transversely to the heat transfer surface, as usual for plate heat exchangers. The flow entering HX2 can therefore neither be assumed as hydrodynamically nor thermally fully developed. Although vortex formation cannot be suppressed in this way, as is the case in HX1, this assembly represents a setup closer to the PHE.

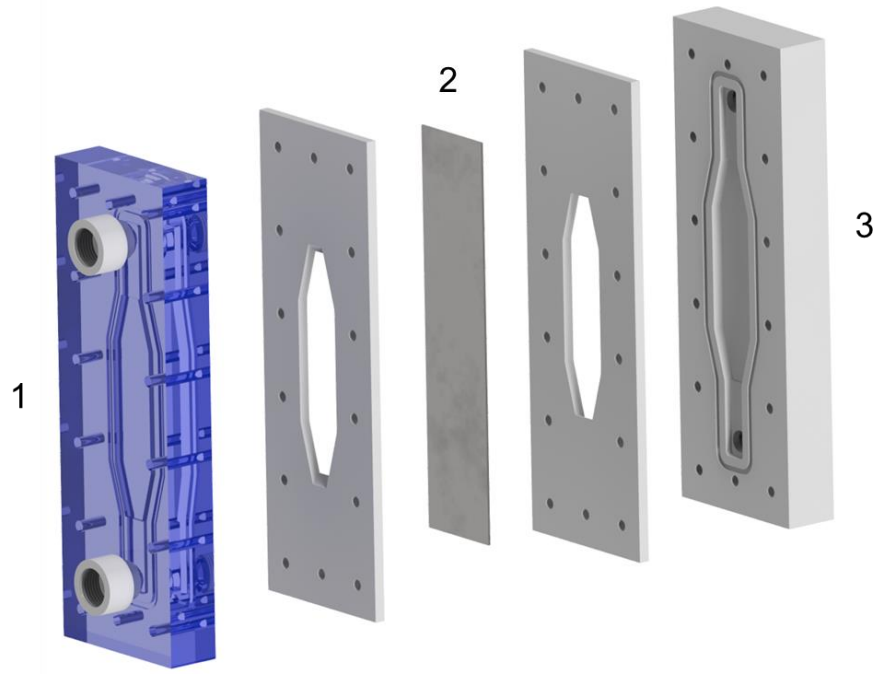

Fig. 4.2: Set-up of the plate heat exchanger test cell (HX2). (1) Cold water circuit, (2) Flat plate sample, (3) Hot water circuit.

Several reasons support the use of multiple test units to investigate fouling processes on the developed polymer composites. As various authors have shown, crystallization fouling processes in heat exchangers depend on the heat transfer material [50,94,95] as well as the process conditions [96,97] (wall temperature, salt concentration, residence time, etc.). In order to focus explicitly on the heat transfer material, controlled test conditions, i.e., especially uniform temperature and flow profiles, are necessary. Therefore, most of the fouling tests are performed in HX1, which ensures the most uniform conditions at the heat transferring surface using flow diffusers. In order to verify the transferability of the results to realistic geometries, further investigations will be carried out in HX2 and the PHE. This will allow the separation of the fouling effects due to the material and the operating conditions.

In all test units, the sample material acts as a heat transfer wall and separates the cold liquid (salt solution) from the hot liquid (hot water). The heating side of the test section is made of polyoxymethylene and is additionally insulated to ensure almost adiabatic conditions. The solution side is made of polymethylmethacrylat to allow visual monitoring of the fouling process

and possible bubble formation. Temperature sensors (Pt100 1/3 DIN) were placed in the flow directly at the inlet and outlet of the test sections, where the temperature distribution and flow profiles are homogeneous. The volume flow rates of the fluids entering the heat exchanger, as well as their temperature, are controlled for constant test conditions. All relevant temperatures and volume flows are recorded transiently. Using the energy balance for the calculation of the heat transfer rate $\dot{Q}$, the overall heat transfer coefficients U are calculated according to Eq. 3.4. As a result of crystallization fouling, the heat transfer rate changes with increasing test duration, providing a transient overall heat transfer coefficient U_f. The resulting thermal fouling resistance R_f is then calculated according to Eq. 4.2 referring to the initial overall heat transfer coefficient U_0 of the clean surface.

$$R_\mathrm{f} = \frac{1}{U_\mathrm{f}} - \frac{1}{U_0} \tag{4.2}$$

4.2.3 Experimental procedure

Prior to each experiment, the investigated polymer compound samples respectively the SS samples were cleaned with isopropanol and deionized water. The screening apparatus was cleaned several times with deionized water to ensure that there were no foreign ions left in the system. The feed solution for the $CaCO_3$-scaling tests is prepared by adding $CaCl_2 \cdot 2\ H_2O$ (≥ 99 %, p.a., ACS, Carl Roth GmbH & Co. KG) and $NaHCO_3$ (≥ 99.7 %, ACS, Sigma-Aldrich Chemie GmbH) to temperature-controlled deionized water, resulting in an initial pH value of about 7.7. For $CaSO_4$-scaling (that is not pH sensitive), the procedure is conducted with the salts Na_2SO_4 (≥ 99 %, ACS, VWR Chemicals) and $Ca(NO_3)_2 \cdot 4\ H_2O$ (≥ 99 %, p.a., ACS, Carl Roth GmbH & Co. KG). Regarding the measurement of the initial overall heat transfer coefficients, the data were recorded for 15 minutes after reaching a steady state before the addition of the second salt (fouling excluded). The bias uncertainties in the initial overall heat transfer coefficients were determined as given in Section 3.2.2 (see Eq. 3.5). After completion of the fouling experiments, the materials to be examined were removed and the deposits were dried and weighed to obtain, besides the thermal fouling resistance, another parameter for assessing the susceptibility to fouling. The deposits were also visually inspected for uniformity and defects to obtain a qualitative statement regarding the adhesion of the deposits to the respective materials.

The test period of the investigations was either adjusted to allow a sound conclusion on the fouling kinetics or to achieve an asymptotic fouling resistance. To accelerate the fouling processes, which can be achieved by high wall temperatures, laminar flow conditions were created

on the cold fluid side (which contains the fouling salts) and turbulent flow conditions on the hot fluid side. In the experiments where bubble formation on the investigated surfaces should be suppressed, a vacuum spray-tube degasser (see Fig. 3.8) was operated before the start of the experiments, which, according to the manufacturer, removes 90 % of the dissolved gases. This completely suppressed the formation of bubbles on the surface. Degassing of the fluid before the start of a fouling experiment is indicated subsequently by dg (degassed). The parameters of all performed fouling experiments are listed in Tab. 4.1.

Tab. 4.1: Operating parameters of the fouling experiments.

Exp. Nr.	Material	Test unit	Re_c	Re_h	$T_{c,in}$ / °C	$T_{h,in}$ / °C	$T_{w,0,calc}$ / °C	Salt	b_{salt} / mmol/kg
1	SS	HX1	500	3900	30	80	68.9	$CaSO_4$	25
2	C143-75	HX1	500	3900	30	80	-	$CaSO_4$	25
3	C143-75-dg	HX1	500	3900	30	80	60.9	$CaSO_4$	25
4	C143-75-sb	HX1	500	3900	30	80	61.6	$CaSO_4$	25
5	SS	HX1	500	3900	40	90	79.4	$CaSO_4$	25
6	C143-75	HX1	500	3900	40	90	-	$CaSO_4$	25
7	C143-75-dg	HX1	500	3900	40	90	71.1	$CaSO_4$	25
8	C143-75-sb	HX1	500	3900	40	90	71.7	$CaSO_4$	25
9	SS	HX1	500	3900	35	90	78.5	$CaCO_3$	3.5
10	C143-75-dg	HX1	500	3900	35	90	70.1	$CaCO_3$	3.5
11	SS	HX2	500	5000	30	80	66.1	$CaSO_4$	25
12	C145-80	HX2	500	5000	30	80	58.7	$CaSO_4$	25
13	SS	HX2	500	5000	30	80	66.1	$CaCO_3$	3.5
14	C145-80	HX2	500	5000	30	80	58.7	$CaCO_3$	3.5
15	C143-75	PHE	500	1000	40	90	51.4	$CaSO_4$	25
16	C143-75	PHE	500	1000	40	90	51.4	$CaCO_3$	3.5

4.2.4 Surface temperature calculation

To draw sound conclusions regarding the fouling processes investigated, knowledge of the surface temperature is crucial besides the surface properties. Since the surface temperatures were not controlled but result from the selected operating parameters as well as material thickness and thermal conductivity, they were estimated as described below for HX1 and HX2. The model from Section 3.2.3 is used to calculate the wall temperatures in the PHE. The two models are based on the same approach, except that for the heat transfer test cells, only one cold and one

hot fluid stream must be considered as described below. In addition, different Nusselt correlations are necessary to calculate the convective heat transfer. The fluid temperature variation in the heat exchanger test cells in flow direction *x* was calculated according to Eq. 4.3 & 4.4.

$$\frac{dT_\mathrm{c}}{dx} = \frac{Uw}{C_\mathrm{c}}(T_\mathrm{h} - T_\mathrm{c}) \tag{4.3}$$

$$\frac{dT_\mathrm{h}}{dx} = \frac{Uw}{C_\mathrm{h}}(T_\mathrm{c} - T_\mathrm{h}) \tag{4.4}$$

To calculate *U*, respectively the convective heat transfer coefficients *h*, Nusselt correlations for turbulent [98] and laminar flows [98,99] were applied. The relation in Eq. 4.5 was used to calculate the initial wall temperatures, which are listed in Tab. 4.1.

$$\dot{Q} = \frac{T_\mathrm{h} - T_\mathrm{w,h}}{\frac{1}{h_\mathrm{h}A}} = \frac{T_\mathrm{w,c} - T_\mathrm{c}}{\frac{1}{h_\mathrm{c}A}} = \frac{T_\mathrm{h} - T_\mathrm{c}}{\frac{1}{UA}} \tag{4.5}$$

Since there are various correlations for the calculation of convective heat transfer coefficients, these were selected to minimize the discrepancy between experiment and model. This procedure led to very small deviations between measured and calculated heat transfer rates for the HX1. These were on average 4 % but maximum 5.9 %. However, for the HX2, which shows flow conditions that are more difficult to describe, the maximum deviation is 14.6% and the average deviation is 9.3%. In addition, estimating the wall temperatures in the presence of air bubbles on the polymer composite surfaces (as discussed later) turns out to be almost impossible, since these represent a location-dependent, transient thermal resistance and strongly influence the flow regime at the surface. It can be expected, though, that higher wall temperatures will occur than on the SS surface with the same operating parameters.

To calculate the wall temperatures in the PHE, the correlation according to Wanniarachchi et al. was used as recommended in the previous chapter. The deviation from the experimentally determined heat flux is 3.5 %.

In order to include fouling resistances in the simulations, the described model is adapted by extending Eq. 3.9 to include thermal fouling resistances.

$$U = \left(\frac{1}{h_\mathrm{h}} + \frac{s_\mathrm{w}}{\lambda_\mathrm{w}} + \frac{s_\mathrm{f}}{\lambda_\mathrm{f}} + \frac{1}{h_\mathrm{c}}\right)^{-1} \tag{4.6}$$

Where $s_\mathrm{f}/\lambda_\mathrm{f}$ indicates the thermal fouling resistance R_f.

4.2.5 CFD modeling

Knowledge of surface temperatures is particularly useful for interpreting crystallization fouling experiments.

Where the temperature profiles in the heat exchanger test cells can be calculated with high accuracy using the model from Section 4.2.4, this proves difficult for the PHE. As shown in the previous chapter, the model provides a very good agreement with the experimental data, but the temperature profiles are only calculated along the flow direction of the fluid. Due to the flow diffusers used in the HX1, this is sufficient in this case, because of the generation of an uniform flow profile orthogonal to the flow direction. However, especially for the PHE, the knowledge of the temperatures on the complete heat transferring surface is needed for the interpretation of the fouling experiments, since these can vary strongly not only along but also orthogonally to the flow direction. For this purpose, CFD simulations were performed with Ansys Fluent. To evaluate the flow through the developed PHE, a complete duct was adopted as the fluid domain, as shown in Fig. 4.3 and simulated with the k-ω SST model as turbulence model.

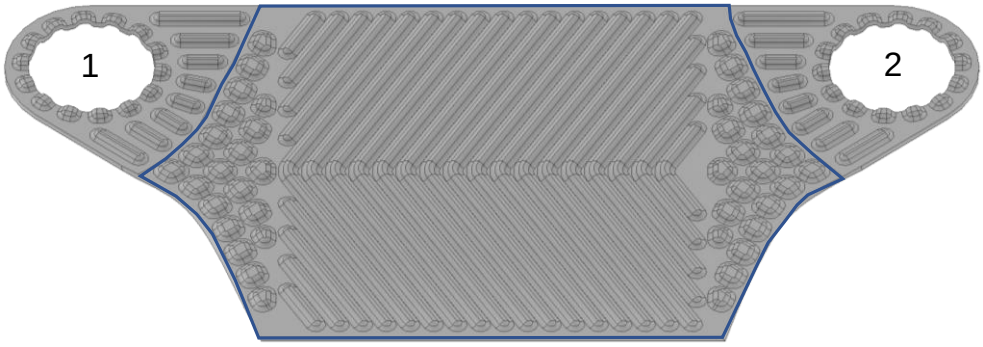

Fig. 4.3: Schematic view of the flow domain of the investigated PHE channel. (1) Inlet. (2) Outlet. Bordered surface: Heat transferring surface.

However, the actual heat transfer from hot to cold fluid could not be simulated, so the transferred heat flux obtained from the model was set as a boundary condition. This is because, as already shown in Section 3.2.4, the geometry of the heat exchanger requires a very fine meshing and consequently large computational resources. Even the meshing of a single channel required 15.5 million elements. A value that would have at least tripled for the simulation of the heat transfer (one cold fluid and two hot fluid channels). Furthermore, due to the same reason, no inflation layers could be integrated in the computational grid, which would have made the simulation of the heat transfer inaccurate. The selected unstructured mesh (maximum element size of 0.2 mm) produces wall y+ values of 0.015 - 5.8 (area weighted average of 1.4). Consequently,

particularly at the contact points, the y+ values are slightly too big to perfectly resolve the viscous sublayer. However, the mean value is still within the recommended range [72], which is why it can be assumed that the accuracy is sufficient, especially for the qualitative observations aimed at with the simulations. This is also shown by the comparison of the simulated mean wall temperatures from the mathematical model and the CFD simulations performed. The difference is only 0.1 °C (mathematical model: 51.4 °C; CFD simulations: 51.5 °C). Since the wall temperatures, with respect to the evaluation of crystallization fouling, were the parameters of interest, the area weighted temperature was chosen as the convergence criterion for the CFD simulations.

4.2.6 Optical bubble detection

Under favorable conditions (e.g., if cavitation nuclei are present at the wall), bubbles can form and adhere on the heat transfer surface of the cold fluid side during the experiments. The gases dissolved in the fluid are present there in a supersaturated form due to the higher wall temperature compared to the bulk. In order to detect the amount of bubbles covering the heat transfer surfaces images were taken and processed transiently.

The optical recording of the air bubbles was performed with a Nikon D5600 SLR camera using a Nikon Micro-Nikkor 55 mm lens and a ring light as illumination unit. This provides a better contrast between air bubbles and sample surface. To determine the degree of bubble coverage on the heat transferring surface, an optical image analysis is performed using an algorithm with functions of the Image Processing Toolbox of Matlab®. This involves cropping the image to the heat transfer surface followed by the creation of a grayscale image. The contrast of the image is increased, and the image is sharpened and binarized. Custom parameter adjustment ensures that the bubbles are captured correctly. The parameters to be adjusted are the greyscale threshold, the setting of the minimum number of pixels forming a bubble (removing noise) and creating disk-shaped circular rings (to make sure that the bubbles are detected as a whole). This process, illustrated in Fig. 4.4, generates binary images that can be utilized to calculate the percentage of the heat transfer surface covered by air bubbles. However, a distinction of the bubble size is not performed by the algorithm.

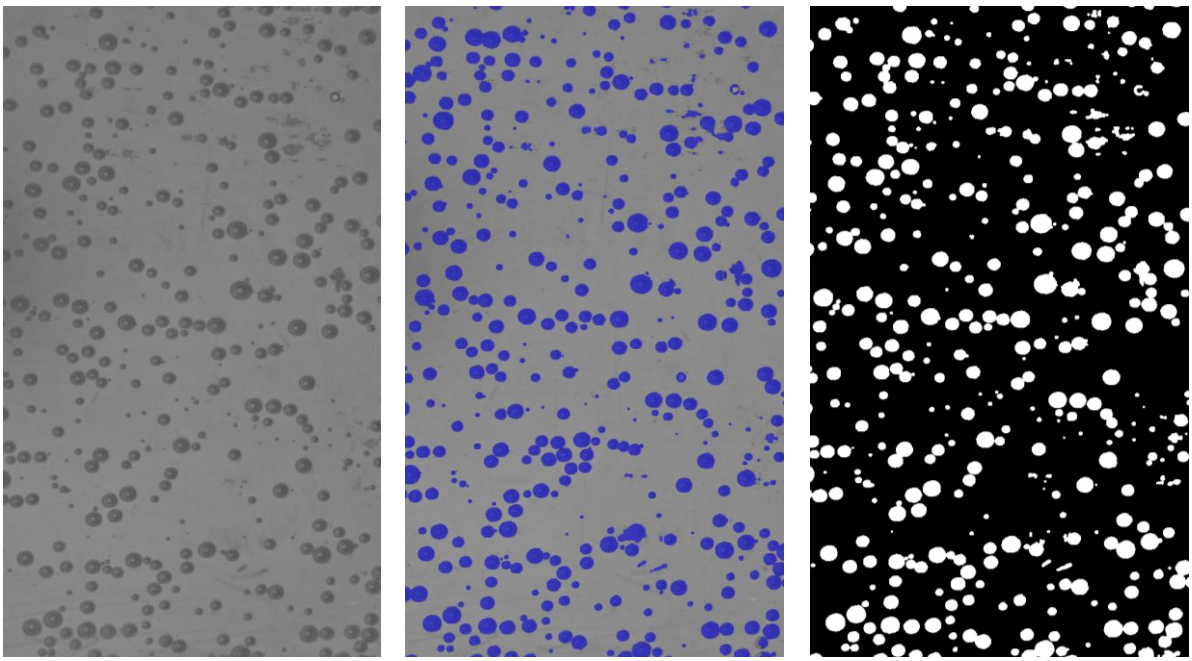

(a) (b) (c)

Fig. 4.4: Workflow of the optical bubble detection. (a) Greyscale image; (b) Overlay for parameter adjustment; (c) Binary image for bubble area determination.

4.3 Results and Discussion

4.3.1 Bubble influence on the fouling resistance

If air bubbles form on the heat transfer surface during a fouling experiment, there are two effects that influence the transient fouling resistance. The first issue is the development of an apparent fouling resistance that is not accompanied by deposition. This effect is illustrated in Fig. 4.5. In fact, this is a thermal resistance due to the formation of air bubbles on the heat exchanger surface. Henceforth referred to as R_{bub}.

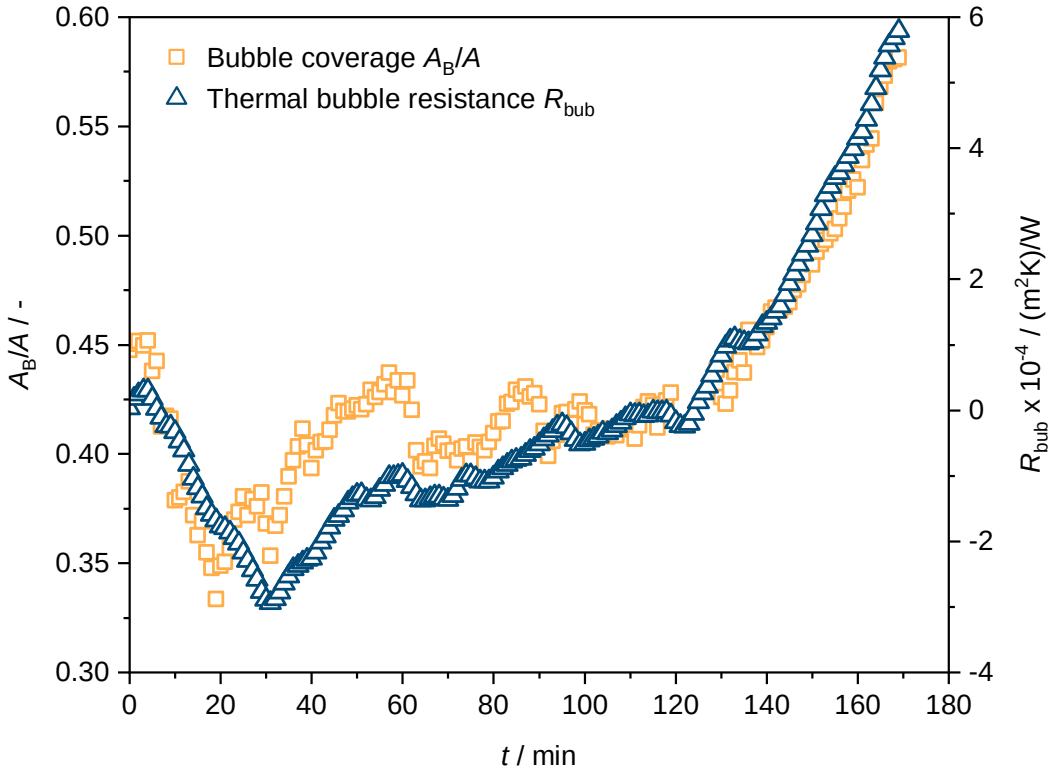

Fig. 4.5: Influence of surface bubble coverage on the thermal resistance. Exp. 2.

Particularly the addition of salt at the beginning of the experiments leads to a supersaturation of the gases in the solution in proximity to the hot sample surfaces. Consequently, many bubbles form on the surface under investigation. To put this into perspective, it must be added that this behavior was only observed in the case of the untreated polymer composites for the HX1.

Almost no bubbles formed on the SS surface and on the sandblasted polymer composite surface they did not adhere. Hence, no change in the overall heat transfer coefficient by avoiding air bubbles (degassing) could be observed, which is why the optical evaluation for the fouling tests was not carried out with these materials. The same applies to the HX2. Even if the Reynolds numbers indicate laminar flow, the arrangement of the inlets causes local turbulence, which prevents the formation of bubbles. The magnitude of the influence of bubble coverage on the

heat transfer using polymer composites is shown by Fig. 4.6. The heat transfer coefficient at the beginning of the fouling test is up to 40% lower in the presence of bubbles (C143-75) than in the absence of bubbles (C143-75-dg and C143-75-sb, respectively). Consequently, more gas residues are present at the surface of the polymer composites, which act as initiators for the formation of bubbles. This so-called heterogeneous bubble formation depends strongly on the surface properties. Rough hydrophobic surfaces (such as the polymer composites used, see Section 2.3.3) nucleate bubbles easily even at low supersaturations, while hydrophilic or even smooth hydrophobic surfaces (such as SS) nucleate bubbles only at exceptionally large supersaturations [100,101].

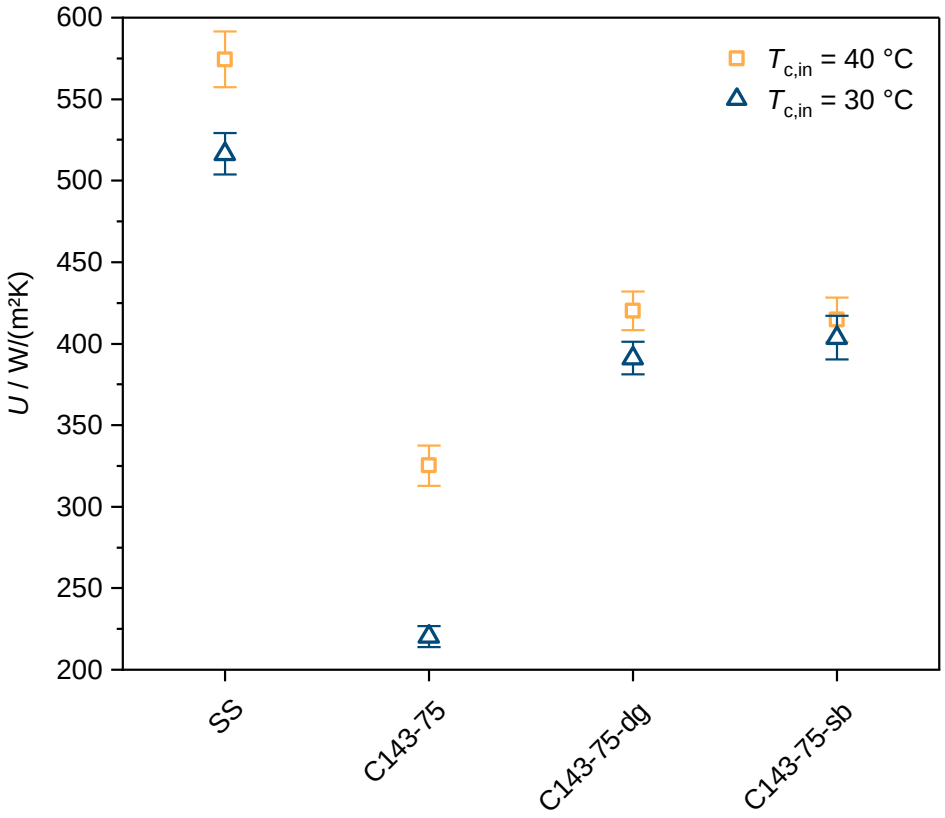

Fig. 4.6: Overall heat transfer coefficients U_0 at the beginning of the fouling experiments in HX1.

In the case of the sandblasted material, which has a superhydrophobic surface due to its high roughness (see Fig. 2.18), bubbles do form, but these bead off in a similar way to the lotus effect and do not adhere [102]. As a result, the bubble coverage of the surface is so low that it has no measurable impact on the overall heat transfer coefficient.

The second issue that arises when air bubbles form on heat transfer surfaces is an enhanced formation of deposits, as can be seen in Fig. 4.7. In the case of non-sandblasted polymer composite, two fundamentally different results are obtained depending on whether the test solution was previously degassed or not. The fouling resistance that occurs after 60 hours, when the test

solution has not been degassed (dg) previously, is approximately a factor of 20 greater compared to degassed solution. This is also evident from the masses of the deposits (see Tab. 4.2), as seven times the mass of $CaSO_4$ is deposited in the presence of air bubbles under otherwise identical experimental conditions. Consequently, when degassed fluid is used, there is almost no fouling propensity, whereas there is a strong fouling propensity when non-degassed fluid is used, which can only be attributed to the presence of air bubbles on the heat-transferring surface.

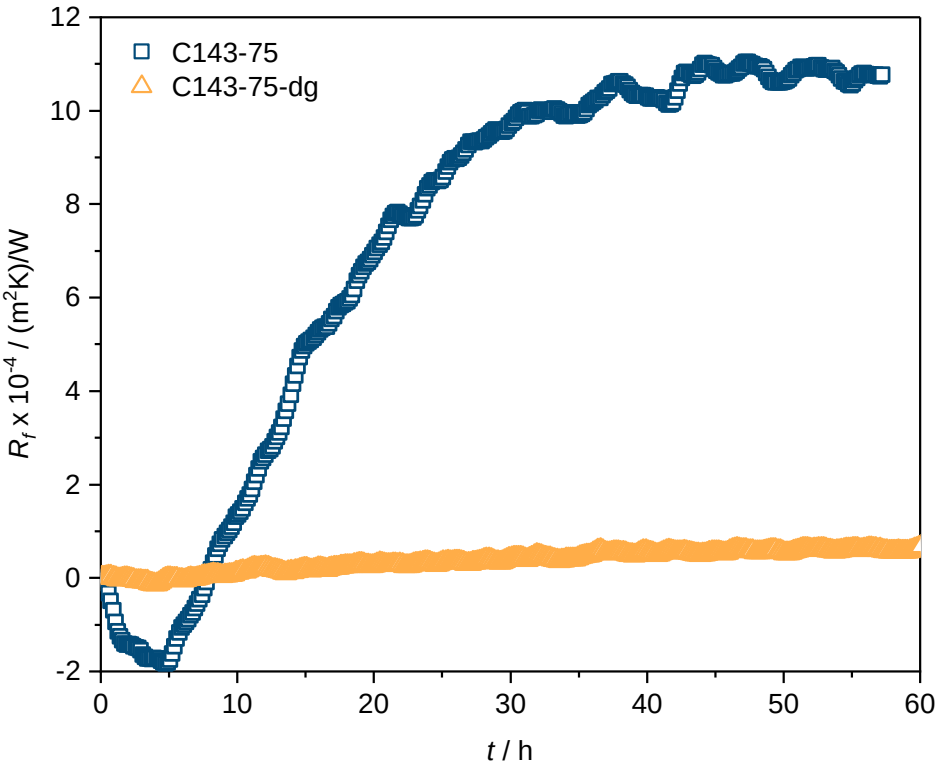

Fig. 4.7: Influence of bubble formation on the fouling resistance. Exp. 2 & 3.

In this case, the heat transferring surface was almost completely covered with air bubbles, that could not be removed by the existing laminar flow and buoyancy forces. The consequence of such gas accumulation has already been discussed in the literature and has a severe effect on the fouling process [103]. When gas bubbles grow on active nucleation sites on the heat transfer surface, the temperature beneath the gas bubbles and in the vicinity of the heat transfer surface increases. Consequently, there is a higher supersaturation at the boundary layer, which enhances the deposition of the salts. The structure of the deposits also changes considerably as evident in Fig. 4.8. The bubble structure is clearly recognizable there and differs from the classical crystal structures.

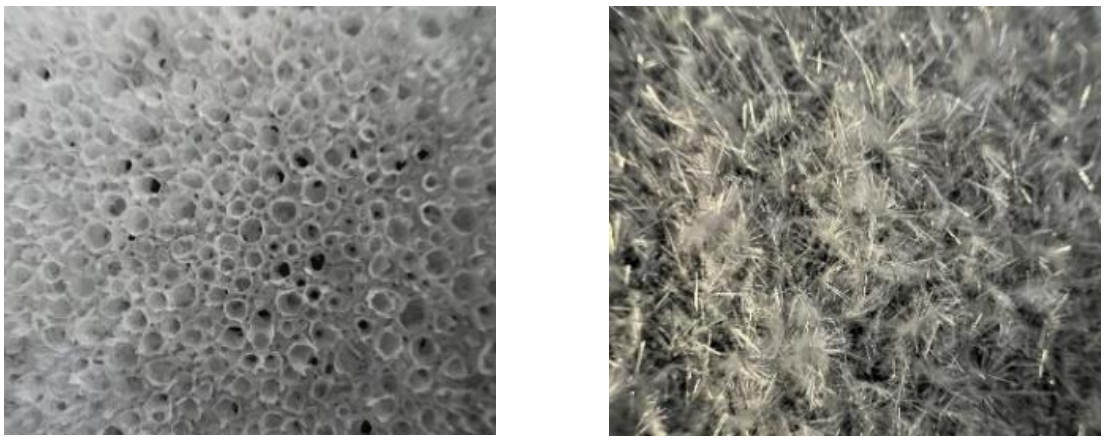

(a) (b)

Fig. 4.8: Influence of the presence of bubbles in the fouling process on the crystal structure formed; (a) bubbles, Exp. 2. (b) no bubbles, Exp. 5.

In order to avoid fouling on the composites investigated here and hence make them competitive to the reference material SS, adherent air bubbles on the surfaces must be avoided. The possibilities to achieve this are degassing of the fluids containing the substances causing fouling, prevention by surface adjustment or hydrodynamic adjustment to remove the bubbles. From a technical point of view, only the two proposals mentioned last are suitable.

4.3.2 Fouling kinetics and quantity

Heat exchanger test cell

Fig. 4.9 and Fig. 4.10 show the results of the fouling tests in HX1 for two different fluid temperatures and $CaSO_4$ fouling. In the case of lower fluid temperatures, there are no major differences between the materials, although SS displays the fastest kinetics, which could be explained by the higher wall temperature. Furthermore, the fouling curve of the untreated polymer composite (C143-dg) seems to change to a steady state after 60 hours, whereas SS still shows a very steep increase. At this point, SS exhibits a fouling resistance value that is twice to three times higher than that of the polymer composites. The masses deposited at the end of the tests are not that conclusive. Although twice as much salt is deposited on stainless steel compared to the material that is least susceptible to fouling in terms of thermal fouling resistance, only a minor difference exists between the untreated polymer composite and stainless steel. To assess with certainty whether the differences between the materials are only due to the different wall temperatures or to the different surface properties, very long experiments or experiments at higher temperatures are necessary.

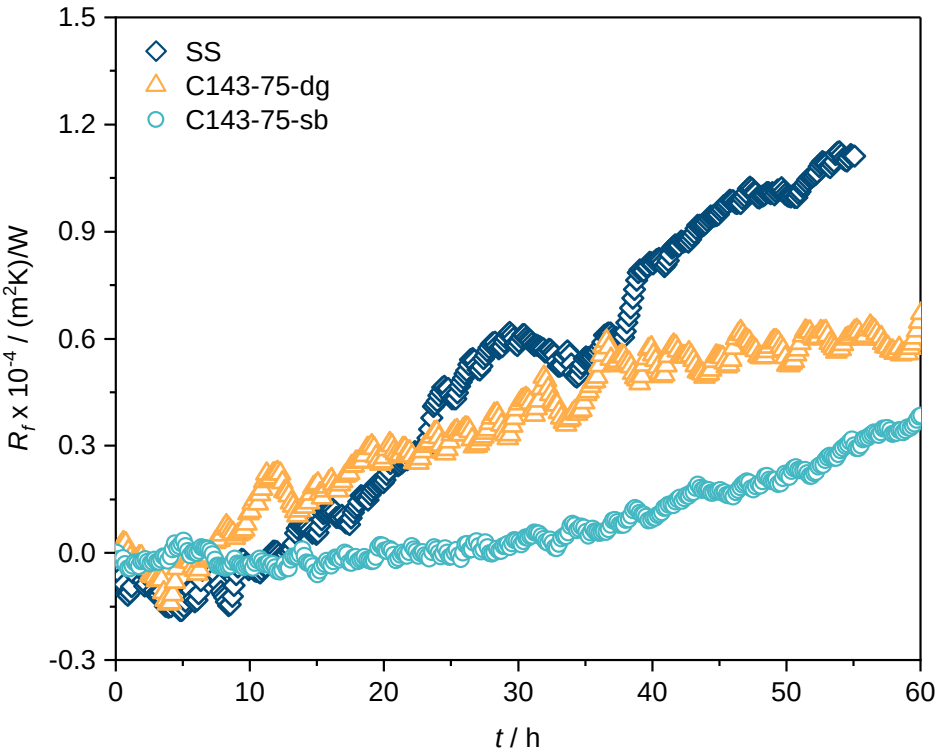

Fig. 4.9: Fouling resistance curves. Exp. 1,3,4.

The results for higher fluid temperatures (see Fig. 4.10) are more impressive. These are accompanied by higher wall temperatures, resulting in higher supersaturation and through the strongly temperature dependent surface integration of ions into the crystal lattice, an overall increase in the rate of crystal deposition [86,96].

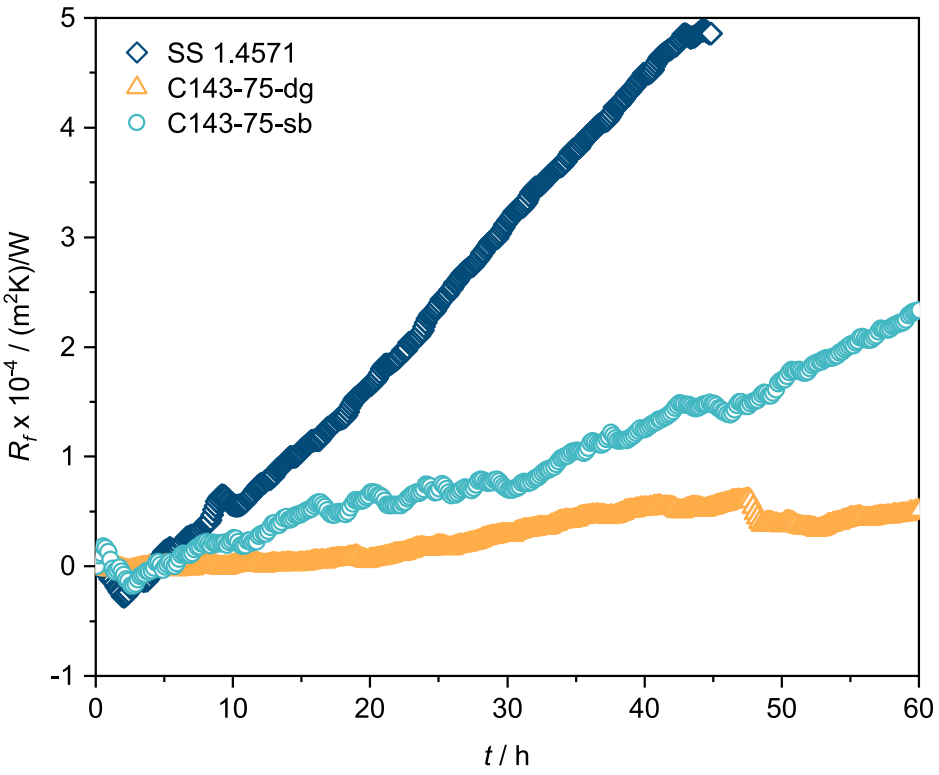

Fig. 4.10: Fouling resistance curves; Exp. 5,7,8.

Especially on the SS surface, a sharp increase of the fouling resistance takes place in a short time, which speaks for fast kinetics compared to the polymer materials. Again, higher surface temperatures are obviously present on the SS surface, but this is compensated by the formation of the thick fouling layer on SS during the experiment. An increasing fouling layer thickness causes the temperature to decrease at the fluid-fouling layer interface, since the transferred heat flux decreases (in the present experimental design). Additionally, the fouling kinetics on SS at a wall temperature of 68.9°C (Exp. 1). is faster than that on the polymer composite at a wall temperature of 71.1°C (Exp. 7). The linear increase in fouling resistance is 2.7×10^{-3} m²K/kW per hour in the case of Exp. 1 (SS) and 2.2×10^{-3} m²K/kW per hour in the case of Exp. 2 (C143-75). At higher wall temperatures, the advantages of the polymer composites over SS also become apparent when looking at the deposited masses in Tab. 4.2, which are about twice as large for SS.

Tab. 4.2: Mass of the deposits after the experiments with $CaSO_4$ in HX1.

Exp. Nr.	Material	m_{dep} / g/m²
1	SS	88.96
2	C143-75	707.29
3	C143-75-dg	100.42
4	C143-75-sb	44.58
5	SS	233.47
6	C143-75	752.08
7	C143-75-dg	126.39
8	C143-75-sb	114.44

Thus, even when wall temperatures are considered, it is concluded that the polymer composites are less susceptible to fouling than SS. Furthermore, it is remarkable that the untreated polymer is hardly affected by the higher temperatures, which are associated with higher supersaturations at the wall and hence faster kinetics. The reason for this is the poor adhesion of the salts to the surface, an effect which has already been demonstrated in the literature for polymer surfaces [104]. After reaching a critical layer thickness, this leads to parts of the fouling layer falling off, caused by the shear forces of the fluid flow (see t=47 h in Fig. 4.11). The fouling resistance drops by 0.23E-4 at this point. Afterwards it rises with the same incline as before. The fouling curve thus corresponds to the sawtooth shape known from the literature [87,88]. This self-cleaning effect could lead to consistently low fouling resistances and consequently longer service time intervals, especially when high shear forces and turbulences are generated (as is the case in PHEs).

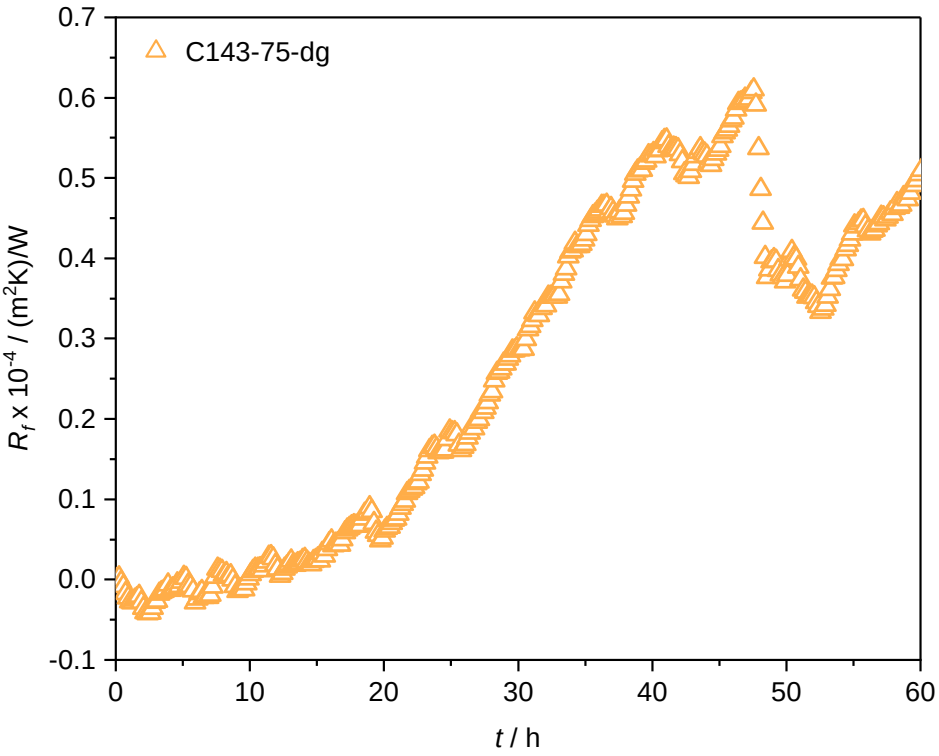

Fig. 4.11: Fouling resistance curve and self-cleaning effect illustration; Exp. 7.

Incidentally, this also applies if a very large salt layer forms on the polymer composite sample due to bubble formation (as in Fig. 4.7). The layer detached itself completely after drying and was only held in place by the walls of the heat exchanger. Cleaning in place of the materials with respect to crystallization fouling should therefore be straightforward based on the qualitative results shown here.

The fact that the sandblasted sample performed worse than the untreated sample at the higher fluid temperatures appears to be due to a change in induction phase, which decreases with increasing wall temperature due to increased crystallization fouling rates. The induction time is about 30 hours long for the lower temperatures (see Fig. 4.9). Thereafter, the fouling kinetics exceed that of the untreated polymer. However, these findings contradict those of the masses deposited at the end of the fouling tests in Tab. 4.2, which imply similar fouling susceptibility of treated and untreated surfaces.

This is due to the fact that the thermal fouling resistances plotted in the diagrams are based only on the measurement of the overall heat transfer coefficient (see Eq. 4.2). It is therefore implied that the change in the heat transfer coefficient has only one cause, namely the creation of an additional thermal resistance by the growing fouling layer. However, the growing fouling layer leads not only to a deposit resistance but also to a change in convective resistance as show by many authors [105–107]. Thus, the increase in surface roughness due to the fouling layer promotes turbulences at the surface leading to an increase in convective heat transfer, which can

strongly influence R_f, especially in the presence of thin fouling layers. This effect becomes negligible for large deposit quantities, whereas for thick fouling layers the constriction of the flow cross section can lead to a significant influence due to increased flow velocities. The latter effect can be neglected due to the relatively high cross-sectional area in the HX1. Moreover, most of the measured fouling curves are only affected by the first mentioned effect at the beginning of the experiments. But, as mentioned above, inconsistencies appear between the comparison of fouling curves and fouling masses of C143-75-dg and C143-75-sb. The sandblasted sample already shows a very rough surface at the beginning of the test, which is why it benefits less from the formation of the fouling layer with regard to the improvement of convective heat transfer. In the case of the untreated sample, however, the influence of the increase in roughness due to the formation of the fouling layer appears to be significant, since a lower R_f is obtained on it for nearly identical fouling mass. However, since the fouling layer adheres better to the sandblasted specimen (no fragments of the fouling layer detached in any test), it can be assumed that the untreated specimen is advantageous for long test durations.

Supplementary Fig. 4.12 shows the results of the fouling tests for a second model salt system (calcium carbonate) and high wall temperatures. As with calcium sulfate fouling, significant advantages of the polymer composites over SS can be identified.

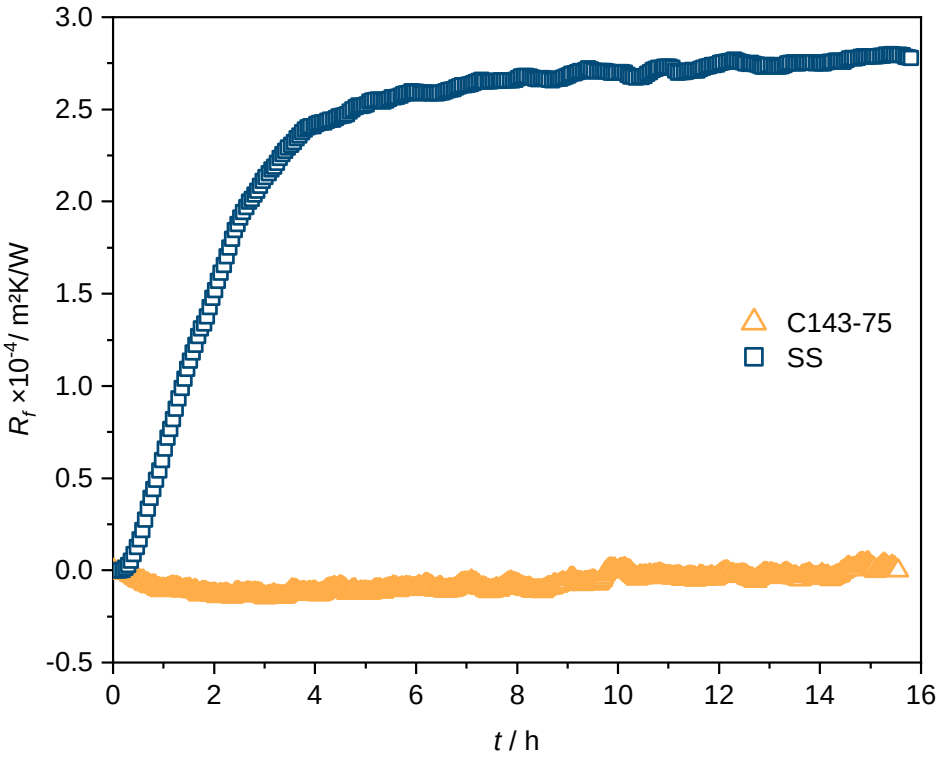

Fig. 4.12: Fouling resistance curves. Exp. 9 & 10.

In the case of the more dynamic $CaCO_3$ fouling, asymptotic fouling resistances form already after 15 h of testing. Where an asymptotic fouling resistance of 0.27 m²K/kW is formed on SS, the composite shows almost no fouling susceptibility. Consequently, this also applies to the fouling kinetics, which are expressed by the linear increase of the fouling resistance. Even if this is not evident in this plot, the fouling resistance related to C143-75 increases by 1.1×10^{-3} m²K/kW per hour from a testing time of two hours. The fouling resistance of the SS sample, on the other hand, increases in the initial phase by 8.8×10^{-2} m²K/kW per hour, which corresponds to a factor of 80.

In any case, the use of polymer composites seems to be advantageous over SS in systems susceptible to crystallization fouling. This is confirmed by the results obtained with HX2 for calcium sulfate as well as for calcium carbonate fouling (Fig. 4.13 and Fig. 4.14 respectively). Even though the volume flow rates of the cold fluid streams were adjusted to give the same mean Reynolds numbers, different flow conditions prevail in this heat exchanger, as described in Section 4.2.2. Thus, higher flow velocities than implied by the Reynolds number prevail there partially. This primarily leads to better removal of bubbles due to local turbulence. The improved removal also influences deposits, which, based on the previous discussion, mainly advantages the polymer composite.

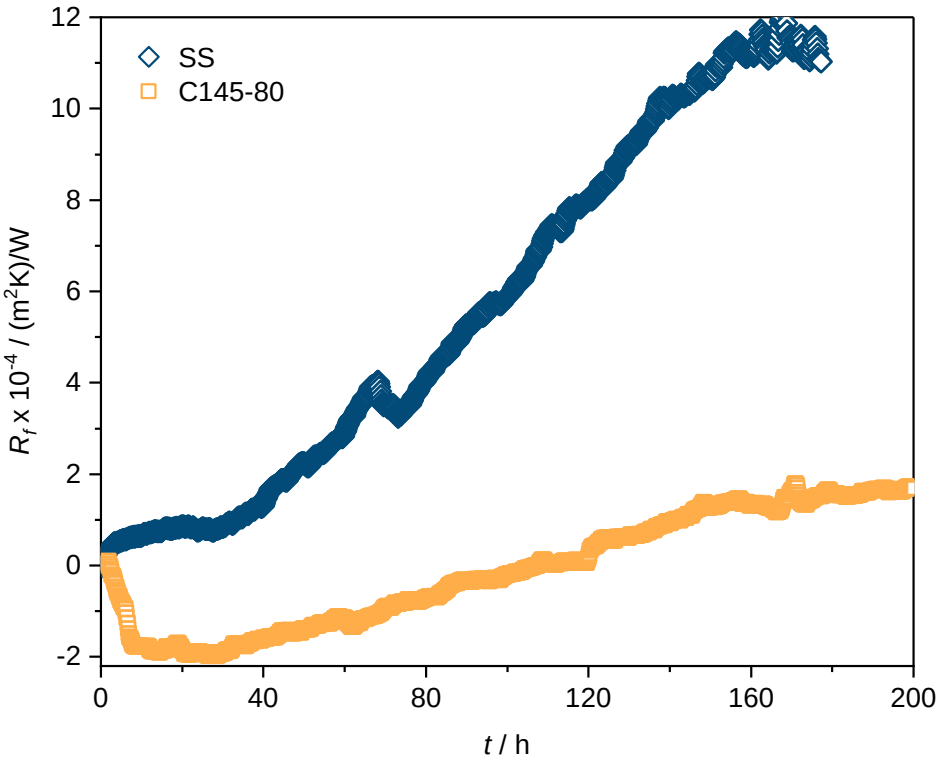

Fig. 4.13: Fouling resistance curves. Exp. 11 & 12.

Fig. 4.13 and Fig. 4.14 confirm this thesis. For both calcium sulfate and calcium carbonate, significantly higher fouling resistances are formed with SS as heat transfer surface. In addition, the polymer composite shows a strongly pronounced negative fouling resistance over a long period of time. Such negative fouling resistances result as previously discussed from increasing convective heat transfer coefficients due to local turbulence caused by initial crystal formation.

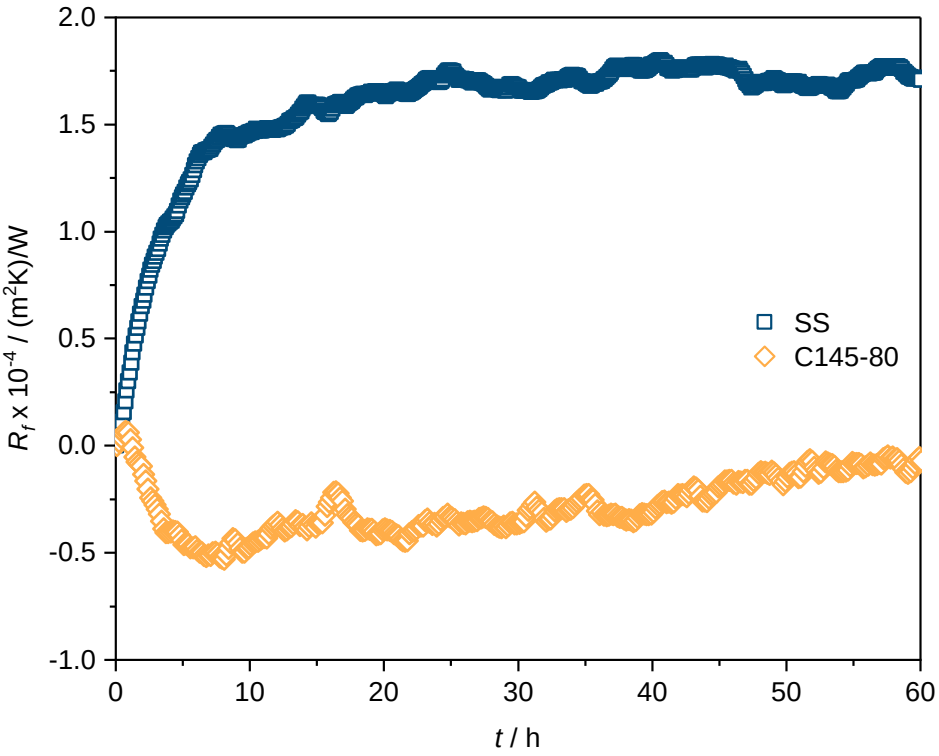

Fig. 4.14: Fouling resistance curves. Exp. 13 & 14.

Due to the poor adhesion to the composite, a covering fouling layer is never formed in HX2. It remains patchy, which explains the positive effect on the fouling resistance. The increased heat transfer coefficient thus almost compensates for (Fig. 4.13) or exceeds (Fig. 4.14) the thermal resistance caused by the deposits. This is also demonstrated by the amounts deposited on the surfaces in Tab. 4.3. The deposited quantities on the polymer composites are out of proportion to the low fouling resistances.

Tab. 4.3: Mass of the deposits after the experiments in HX2.

Exp. Nr.	Material	m_{dep} / g/m²
11	SS	836.8
12	C145-80	163.7
13	SS	90.8
14	C145-80	19.9

Possible properties underlying fouling-resistant surfaces have been discussed frequently in the literature [16,108–110]. In most cases, the topographic and energetic surface properties are used for evaluation. These have already been presented for the developed polymer composites in Section 2.3.3 and are shown again in the following Tab. 4.4 for the materials that were investigated with respect to fouling for clarification. What should always be considered is that the mentioned properties can affect the measurement methods mutually. For example, the significant increase in roughness of the polymer composites by sandblasting also results in significantly higher contact angles and surface free energies. As already discussed in detail in Chapter 2, Young's equation used to determine surface free energies, is only valid for perfectly smooth surfaces [111]. Yet an increase in roughness leads to an increase in the apparent contact angle for liquids that have a Young contact angle of >90 ° [112]. As a result, the sandblasting of the materials apparently increases the surface free energy. The actual value should be nearly the same as that of the non-sandblasted sample.

Tab. 4.4: Material surface properties.

Exp. Nr.	γ_{OWRK} /mNm	θ_{H2O} / °	S_a / µm
SS	40.46	81.4	0.077
C143-75	27.77	93.4	0.243
C143-75-sb	51.91	139.9	9.792
C145-80	27.83	92.2	0.703

Furthermore, a separate evaluation, i.e., which property contributes to which extent to more or less fouling, is hardly possible, since the samples investigated have different surface energies and roughness. As shown in Section 2.3.3, different PP grades and different graphite contents cause only minor differences in the properties considered. The two polymer composite materials examined in the fouling tests can therefore be regarded as representative for the entire material class. Only the sandblasting of the materials causes a significant difference in the surface properties.

A high surface roughness, which usually results in a shorter induction phase due to faster nucleation processes, does not seem to be crucial for the fouling process with the investigated materials. The reason for this assumption is the many times higher roughness of the composites, especially if sandblasted, compared to SS. The advantage over SS in terms of lower asymptotic fouling resistance and slower crystallization fouling kinetics must therefore be due to the different surface free energies of the materials investigated. Overall, it can be stated that the polymer composite surfaces possess a lower surface energy than the SS surface, which in this particular case appears to lead to a lower susceptibility of fouling. The fact that a lower surface energy leads to less deposit formation is in accordance with the literature [16,109,113,114]. However, the different energetic behavior of different surfaces at the interface between the initial crystals and the surface is very complex and cannot be reduced to one parameter alone, such as the surface free energy [115]. Therefore, no correlation can be given between surface free energy and fouling behavior. Furthermore, it cannot be stated in general that the use of polymer surfaces always leads to reduced fouling susceptibility compared to metallic surfaces. Several authors have observed both an increase [116] and a decrease [113,117] in fouling susceptibility in a direct comparison of polymer surfaces with metallic surfaces. An assessment must therefore always be made in a direct comparison, whereby a low surface energy seems generally to be preferred. This usually results also in poor adhesion of deposits [110], which facilitates cleaning of the heat exchangers in-place and may avoid a blocking of single channels. For this reason, surface treatments and coatings that reduce the surface energy of thermal plates of PHEs have proven to be very useful [16,108]. The low adhesion forces between surface and crystal due to low energy surfaces can also be observed for the material C143-75, as shown (see Fig. 4.11) and discussed above. However, to transfer these positive results to PHEs, an optimal design (shape and size of the plates, overall flow design, etc.) of the unit is necessary. In order to verify whether this already applies to the developed PHE, preliminary fouling investigations were carried out in it.

Plate heat exchanger

To assess the fouling susceptibility of the developed heat exchangers, Fig. 4.15 shows the thermal fouling resistances developed over the test period for the model systems calcium carbonate and calcium sulfate. The salt concentrations were chosen according to the experiments in the heat exchanger test cells. The boundary conditions were chosen to ensure that the wall temperatures were as high as possible to accelerate fouling. Consequently, low Reynolds numbers on the solution side and high fluid temperatures were chosen. However, the good heat transfer with PHE results in high temperature differences at the plate surfaces. In Tab. 4.1, the mean value is

given as 51.1, but the actual temperatures vary according to the model from Section 3.2.3 between 45.3 °C and 56.3 °C.

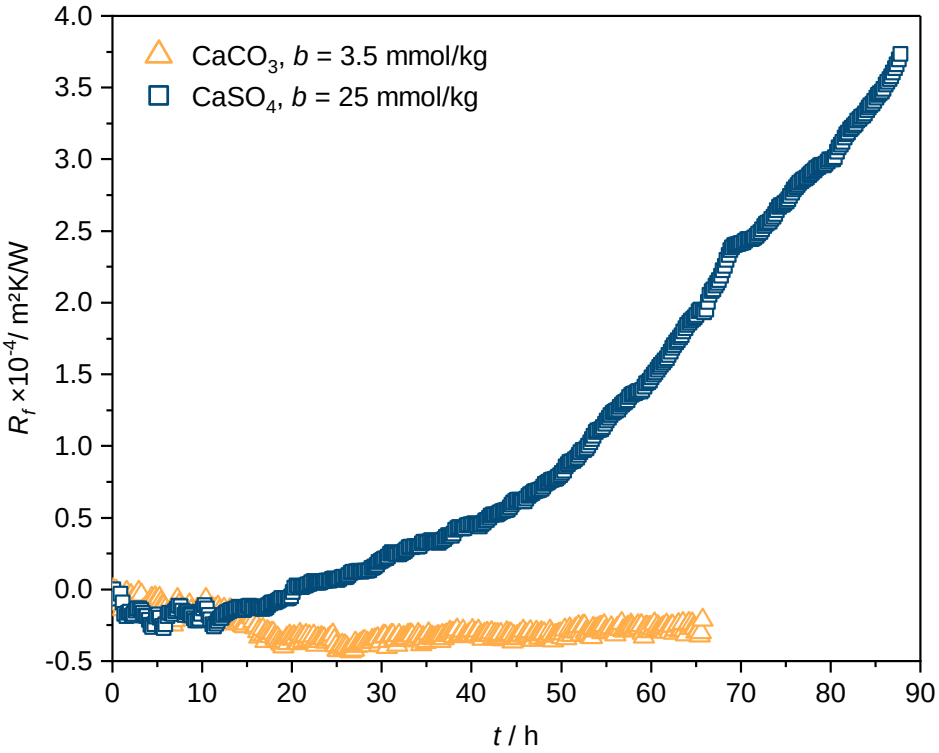

Fig. 4.15: Fouling resistance curves; Exp. 15 &16. N_{tp} = 3.

An eminent difference can be observed between the two model salts. Whereas calcium carbonate shows almost no deposition tendency, very high fouling resistances are formed after an induction phase when using calcium sulfate. At the start of both experiments, the fouling resistances fluctuate around 0 m²K/W or even decrease to negative values. In the experiment carried out with calcium carbonate, however, the fouling resistance does not increase to positive again in the period investigated, which speaks for extremely slow kinetics for the selected experimental conditions. After 65 h, the heat transfer coefficient exceeds the initial one by 1.3 %. Due to the already extremely selected test conditions, i.e., aiming at high temperatures (higher temperatures are not possible due to the use of PP as composite matrix) combined with minimum plate spacing (there are contact points between the individual plates), a tendency to $CaCO_3$ fouling is therefore not given. In the case of $CaSO_4$ fouling, on the other hand, there is an increasing rise in the fouling resistance after a delay time of 20 h. Here, the fouling curve does not conform to one of the typical four patterns [87]: linear, falling rate, asymptotic and saw tooth type, but appears to be self-reinforcing. After 85 hours, this results in a performance reduction of 21%, with an increasing trend. An examination of the fouling layers, illustrated in Fig. 4.16, shows the reason for the self-reinforcing trend.

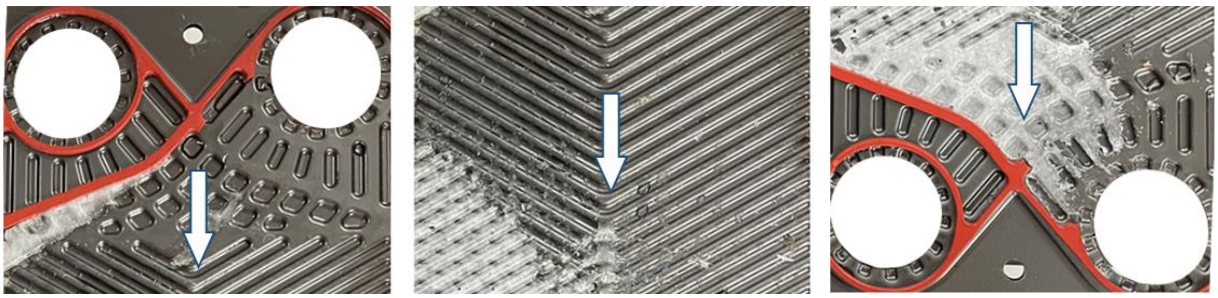

(a) (b) (c)

Fig. 4.16: Visualization of $CaSO_4$ crystallization fouling on the heat transfer surface in the (a) inlet; (b) middle; (c) outlet region.

Some parts of the channels, especially at the outlet, are blocked by the deposits, as a result a part of the heat transfer surface is no longer available for heat transfer. However, since large parts of the heat transfer area seem to be unaffected by fouling after a test period of 85 h, this rather suggests a poorly designed inlet and outlet region (flow distributor) of the PHE, than the unsuitability of the polymer composites in fouling prone systems. Bansal et al. [97] were able to show, for example, that a well-designed inlet and outlet region leads to higher heat fluxes at simultaneously lower susceptibility to fouling because of the generation of an improved flow distribution. Therefore, a proper design of the flow distributor is crucial to exclude flow maldistribution and dead zones and thus to minimize fouling.

In order to verify whether the cause of the fouling tendency in the developed PHE is due to flow maldistributions, CFD simulations are conducted. Hence, Fig. 4.17 shows the simulated residence time distribution in the affected PHE channel.

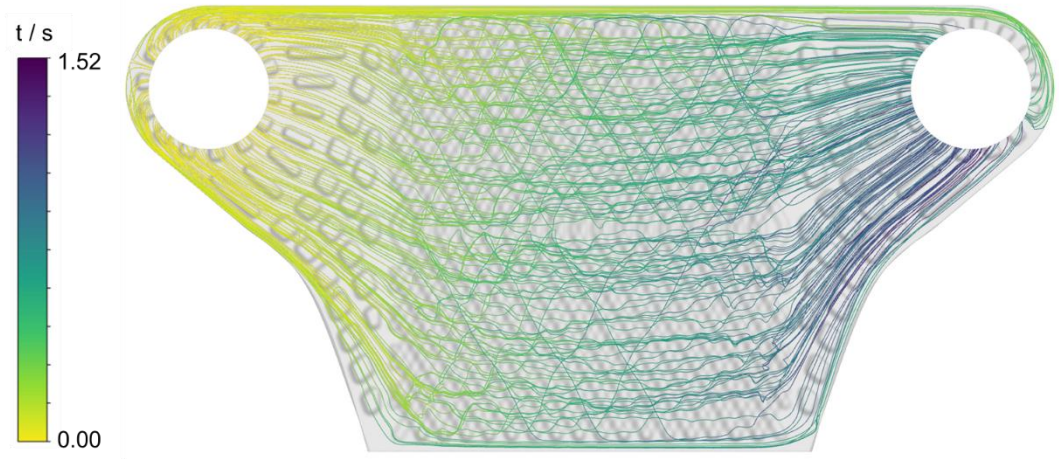

Fig. 4.17: Particle residence time in a PHE channel; 165 Particles.

It is immediately apparent that the fluid residence time is longest in the region most affected by fouling. Furthermore, dead zones appear in the corners of the flow domain, which are also affected by fouling. In addition, parts of the fouling layer cannot be removed due to insufficient

local flow velocities. The self-cleaning effect described above thus does not occur. A longer local residence time of the fluid as well as dead zones favor higher bulk and consequently wall temperatures, which are mainly responsible for crystallization fouling of inverse soluble salts. Therefore, Fig. 4.18 shows the simulated wall temperatures along with the precipitations on the plate.

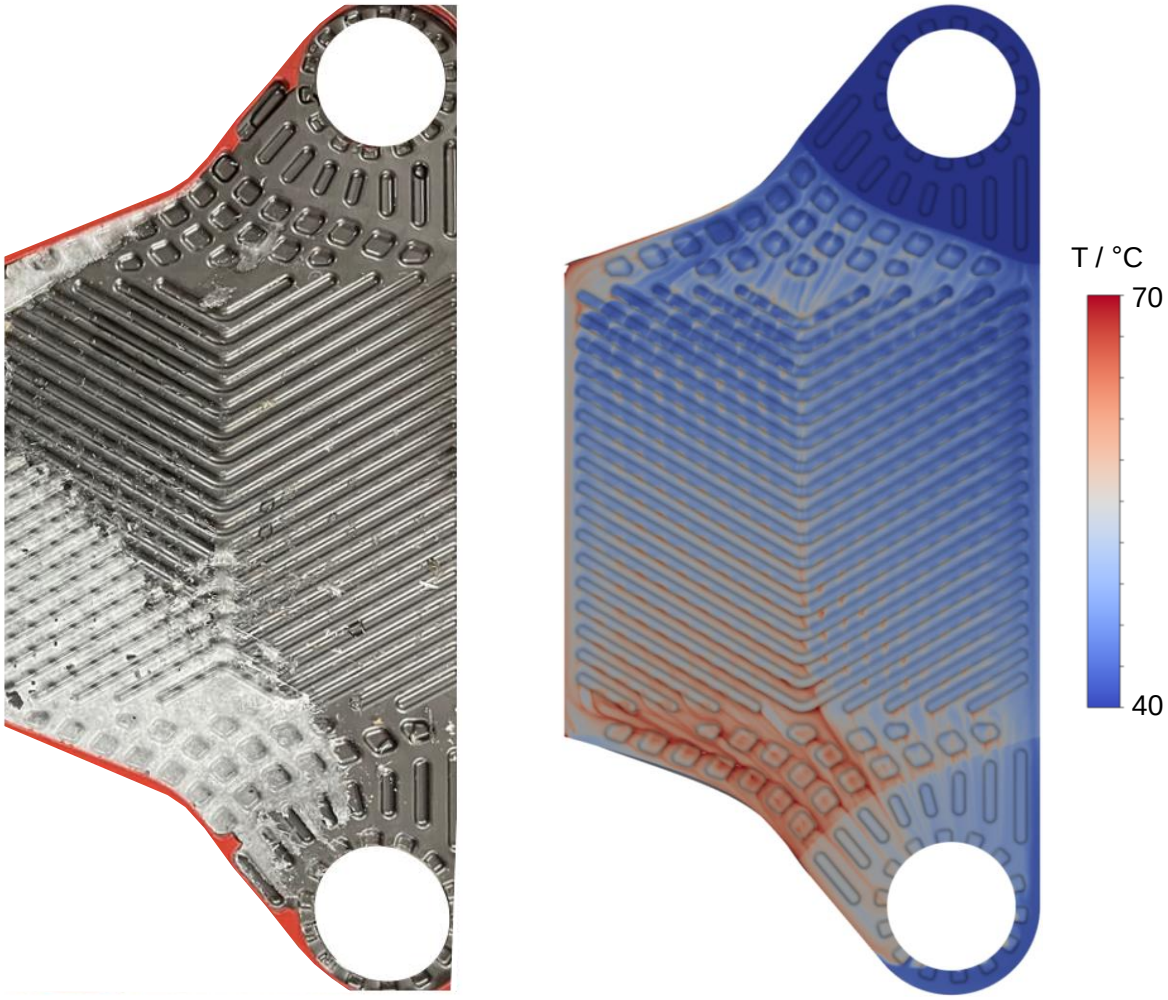

(a) (b)

Fig. 4.18: Visualization of the correlation between simulated wall temperature and scaling. (a) Deposits formed in the experiment. (b) Simulated wall temperatures.

The comparison of the plate affected by fouling with its surface temperature (in the clean state) shows a very clear correlation between high temperatures and crystallization fouling. Whether the design of the PHE plate alone determines whether scaling layers form on the polymer composites cannot be stated with certainty at this point. However, the results suggest that the plate geometry (especially the flow distributors) should be redesigned, with the aim of a more uniform flow and consequently temperature profile to further reduce fouling.

The comparison of the results in Fig. 4.15 with conventional martials is difficult since identical plate geometries would be necessary. However, a qualitative comparison will be attempted at

this point. There are several publications dealing with fouling processes with $CaSO_4$ or $CaCO_3$ in PHEs [97,118,119]. The plate geometry is always similar to the one investigated here (chevron type, same corrugation angle, similar enlargement factor). However, due to lower material thicknesses and the use of metallic heat exchangers, it is likely that higher temperatures are present on these heat exchange surface, which accelerates fouling processes. The higher Reynolds numbers of these investigations, on the other hand, ensure lower fouling susceptibilities because of decreased surface temperatures. Even if higher fouling resistances are usually formed in the publications listed than on the plates investigated here, this cannot be directly equated with lower fouling susceptibility of the polymer composites. However, it is remarkable that parts of the surfaces investigated here remain completely free of fouling (see Fig. 4.16), which is not the case in the publications listed when pronounced fouling occurs. This could be an indication of the advantage of polymer composites over metallic materials in terms of fouling susceptibility. A result that could already be shown for flat plates.

4.3.3 Performance comparison considering fouling effects

So far, all considerations in this chapter have been made only with respect to thermal fouling resistances and deposited masses. To get a better sense of the performance reduction properties of scaling layers, the results of the fouling experiments are implemented below in the model from Section 3.2.3, extended with Eq. 4.6. The considerations here refer only on the asymptotic fouling resistances and are of a hypothetical character. Fig. 4.19 shows the simulations from Fig. 3.28 extended by fouling resistances measured in the experiments. The highest asymptotic fouling resistances measured in the heat transfer test cells (HX1 and HX2) were implemented for both calcium carbonate and calcium sulfate fouling.

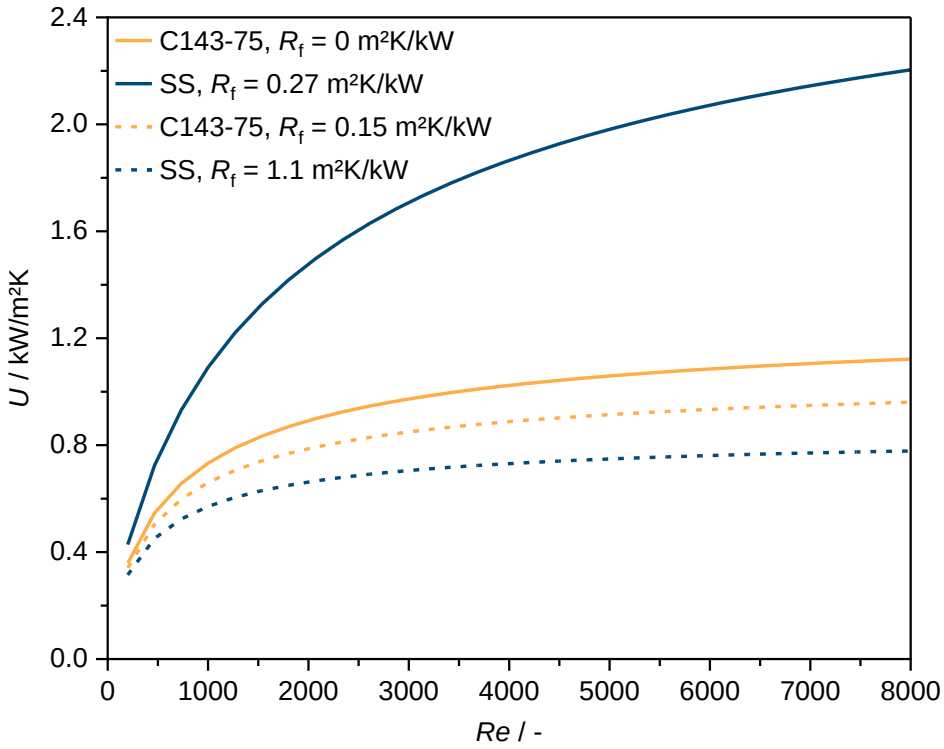

Fig. 4.19: Simulated *U* values for constant Reynolds numbers; $Re_c = Re_h$; Geometry parameters according to Tab. 3.4; Nusselt correlation according to Wanniarachchi. Straight lines correspond to to $CaCO_3$ fouling resistances (Fig. 4.12). Dashed lines correspond to $CaSO_4$ fouling resistances (Fig. 4.13).

Since the SS surface is more affected by fouling, there is a decrease in the performance difference between the composite and SS for $CaCO_3$ fouling. At high Reynolds numbers (Re = 8000), the *U* value of the polymer composite increased from 20.5% to 50.9% compared to SS. Thus, in this scenario, oversizing of the SS heat exchanger would be necessary to compensate for the reduction in performance due to the fouling layer, but not with a C143-75 heat exchanger. With the knowledge in mind that the composites have a much lower density than SS, the composite would be advantageous for the same material weight usage. In fact, consideration of $CaSO_4$ fouling shows that fouling can provide such a severe limitation of heat transfer that the polymer composite surface, which is less affected by fouling, performs better than SS at long operating times. In this scenario, C143-75 outperforms SS by up to 23.4 % regarding *U*. As already mentioned, the observations made here are of a theoretical character. However, on the basis of the experimental results of the fouling tests carried out, there is a justified assumption that the polymer composites also have a very low susceptibility to fouling in the plate heat exchanger and can outperform conventional materials in this respect.

5 Conclusions

The use of heat exchangers in corrosive environments usually forces plant operators to rely on expensive materials such as high alloy steels, titanium, or synthetic graphite. The underlying corrosion resistance of the polymer composite PHEs presented in this thesis, coupled with low raw material costs and manufacturing processes, makes them a viable alternative for these type of heat exchangers. The range of applications can be extended by using different polymers as matrix. For example, a polypropylene-based heat exchanger could be used for temperatures up to 90 °C and a polyphenylene sulfide-based heat exchanger for temperatures up to at least 150 °C. The manufacturing of highly filled thermoplastic graphite composites can compensate for many of the disadvantages of pure polymers for the use in heat exchangers, which makes their use as thermal plates in PHEs conceivable in the first place.

The filler provides a mechanically more stable, stiffer material. The elastic modulus increases by approx. 500 % compared to pure polymer when polypropylene is used as matrix material. Simultaneously, the elongation at break decreases to less than 1 %. In addition, the contact points in plate heat exchangers between the individual plates at minimum plate spacing ensure the necessary mechanical stability over a wide pressure range of the materials that are otherwise less stable than metals.

The increase in thermal conductivity due to the use of graphite as filler is further enhanced by the embossing process, which according to model data results in an increase in thermal conductivity of up to 20 % compared to the non-embossed sheet. Still, due to the anisotropic character of the graphite particles, only effective thermal conductivities up to 2.4 W/mK are achieved. Due to the significantly lower density, the composite materials enable the realization of large heat transfer surfaces at the same heat transfer weight compared to metallic PHEs, which compensates to a considerable degree for their lower thermal conductivity.

In systems susceptible to crystallization fouling the use of the developed polymer composites resulted in significantly reduced fouling proneness compared to stainless steel (SS) when bubble formation was avoided. This can be achieved by degassing the fluids used, sandblasting the surfaces of the polymers (which creates a superhydrophobic surface and prevents bubble adhesion), or creating turbulences on the surfaces. The latter is achieved, for example, simply by the characteristics of PHEs. The reduced fouling susceptibility of the polymer composites is shown by means of slower crystallization kinetics and the formation of lower fouling quantities, for both model salts investigated. Due to lower thermal conductivities of the polymer composites, the use of SS provides higher heat transfer rates, but this fact can be reversed by the formation

of larger fouling layers on the metal. Another major advantage is the low adhesion of deposits to the composite materials, which leads to a self-cleaning effect that could reduce downtimes for cleaning in technical processes. However, the requirement for this is an appropriate design of the flow distributors, the inlet section of the thermal plates, since the formation of dead zones or poorly perfused parts in the PHE can cause the formation of deposits even when fouling resistant materials are used.

Overall, this thesis provides a promising basis for optimized future designs of efficient, corrosion resistant and cost-effective polymer composite based plate heat exchangers especially for industrial applications in corrosive or metal free environments.

6 Outlook

Future work should address two main areas. First, the improvement of the performance of the polymer composite plate heat exchangers to broaden their scope and consequently maximize their applicability. Secondly, the precise characterization of their operating range in terms of thermal and mechanical parameters, to promote their use in industrial applications.

With regard to improving performance, a distinction must be made between material technology and design optimization. Any increase in thermal conductivity of the materials will have a very strong impact on the performance of the PHE. Therefore, further material formulations and possibly an alignment of the graphite particles should be considered. Especially the latter approach may result in a significant increase in through-plane thermal conductivity based on the discussion in Chapter 2, but possibly at the expense of the price of the final product. Design optimization must aim at maximum mechanical stability as well as uniform flow distribution in the fluid channels of the PHE, to avoid fouling as effectively as possible. The main task in this respect is the design of the flow distributors, which should be CFD-aided designed. The peripheral regions where the clamping bolts are placed are also critical, as high stresses act on the material there, which is why great attention should also be paid to optimizing the clamping of the PHE.

To enable the use of novel heat transfer materials, their application limits must be precisely defined. These include the operating temperature, maximum absolute pressures, maximum pressure differences (in accordance with pressure equipment directives), and the definition of chemical resistances. In order to achieve these objectives, a large number of time-intensive load tests are still necessary, since these must also cover long-term behavior (creep behavior, alternating loads, material fatigue) at various temperatures. Only this will enable the safe and effective use of polymer composite PHEs in industrial applications.

References

[1] S. Kakaç, H. Liu, A. Pramuanjaroenkij, Heat exchangers: Selection, rating, and thermal design, 3rd ed., CRC Press, Boca Raton, Fla., 2012.

[2] S. Kakaç, H. Liu, A. Pramuanjaroenkij, Heat Exchangers, CRC Press, 2020.

[3] C. T'Joen, Y. Park, Q. Wang, A. Sommers, X. Han, A. Jacobi, A review on polymer heat exchangers for HVAC&R applications, Int. J. Refrig. 32 (2009) 763–779. 10.1016/j.ijrefrig.2008.11.008.

[4] L. Song, B. Li, D. Zarkadas, S. Christian, K.K. Sirkar, Polymeric Hollow-Fiber Heat Exchangers for Thermal Desalination Processes, Ind. Eng. Chem. Res. 49 (2010) 11961–11977. 10.1021/ie100375b.

[5] D.M. Zarkadas, K.K. Sirkar, Polymeric Hollow Fiber Heat Exchangers: An Alternative for Lower Temperature Applications, Ind. Eng. Chem. Res. 43 (2004) 8093–8106. 10.1021/ie040143k.

[6] M.P. Bond, Plate heat exchangers for effective heat transfer, Chem. Eng. (Chemical Engineer) (1981) 162–167.

[7] J. Kerner, S. Sjogren, L. Svensson, Where plate exchangers offer advantages over shell-and-tube, Power 131 (1987) 53–58.

[8] P. Kapustenko, S. Boldyryev, O. Arsenyeva, G. Khavin, The use of plate heat exchangers to improve energy efficiency in phosphoric acid production, J. Cleaner Prod. 17 (2009) 951–958. 10.1016/j.jclepro.2009.02.005.

[9] N. Burger, A. Laachachi, M. Ferriol, M. Lutz, V. Toniazzo, D. Ruch, Review of thermal conductivity in composites: Mechanisms, parameters and theory, Prog. Polym. Sci. 61 (2016) 1–28. 10.1016/j.progpolymsci.2016.05.001.

[10] H. Chen, V.V. Ginzburg, J. Yang, Y. Yang, W. Liu, Y. Huang, L. Du, B. Chen, Thermal conductivity of polymer-based composites: Fundamentals and applications, Prog. Polym. Sci. 59 (2016) 41–85. 10.1016/j.progpolymsci.2016.03.001.

[11] S. Ghaffari-Mosanenzadeh, O. Aghababaei Tafreshi, E. Dammen-Brower, E. Rad, M. Meysami, H.E. Naguib, A review on high thermally conductive polymeric composites, Polym. Compos. 43 (2022) 692–711. 10.1002/pc.26420.

[12] O. Breuer, U. Sundararaj, Big returns from small fibers: A review of polymer/carbon nanotube composites, Polym. Compos. 25 (2004) 630–645. 10.1002/pc.20058.

[13] H. Glade, D. Moses, T. Orth, Polymer Composite Heat Exchangers, in: H.-J. Bart, S. Scholl (Eds.), Innovative Heat Exchangers, Springer International Publishing, Cham, 2018, pp. 53–116.

[14] S. Schilling, H. Glade, T. Orth, Investigation of Crystallization Fouling on Novel Polymer Composite Heat Exchanger Tubes, Heat Transfer Eng. 43 (2022) 1326–1336. 10.1080/01457632.2021.1963533.

[15] P. Jamzad, J. Kenna, M. Bahrami, Development of novel plate heat exchanger using natural graphite sheet, Int. J. Heat Mass Transfer 131 (2019) 1205–1210. 10.1016/j.ijheatmasstransfer.2018.11.129.

[16] Zettler H. U., M. Wei, Q. Zhao, H. Müller-Steinhagen, Influence of Surface Properties and Characteristics on Fouling in Plate Heat Exchangers, Heat Transfer Eng. 26 (2005) 3–17. 10.1080/01457630590897024.

[17] M. Bangavadi Munivenkatappa, M.E.E. Franklin, A.V. Dhotre, H.A. Pushpadass, Shivanand, A. Anthonysamy, P.K. Mandhyan, P.G. Patil, Mitigation of fouling during milk processing in polytetrafluoroethylene-titanium dioxide coated plate heat exchanger, J. Food Process Eng 45 (2022). 10.1111/jfpe.13836.

[18] S. Balasubramanian, V.M. Puri, Reduction of Milk Fouling in a Plate Heat Exchanger System Using Food-Grade Surface Coating, Trans. ASABE 52 (2009) 1603–1610. 10.13031/2013.29111.

[19] W. Faes, S. Lecompte, Z.Y. Ahmed, J. van Bael, R. Salenbien, K. Verbeken, M. de Paepe, Corrosion and corrosion prevention in heat exchangers, Corros. Rev. 37 (2019) 131–155. 10.1515/corrrev-2018-0054.

[20] L. Wang, B. Sundén, R.M. Manglik, Plate heat exchangers: Design, applications and performance, WIT Press, Southampton, 2007.

[21] Heat Transfer and Pressure Drop Characteristics of Plate-and-Frame Heat Exchangers: A Literature Review, 1993.

[22] Plate heat exchangers for process industry applications: enhanced thermal-hydraulic characteristics of chevron plates, 1996.

[23] R. Steinhagen, H. Müller-Steinhagen, K. Maani, Problems and Costs due to Heat Exchanger Fouling in New Zealand Industries, Heat Transfer Eng. 14 (1993) 19–30. 10.1080/01457639308939791.

[24] S. Kakaç, H. Liu, A. Pramuanjaroenkij, Heat exchangers: Selection, rating, and thermal design, CRC Press, Boca Raton, Fla., 2020.

[25] X. Chen, Y. Su, D. Reay, S. Riffat, Recent research developments in polymer heat exchangers – A review, Renewable Sustainable Energy Rev. 60 (2016) 1367–1386. 10.1016/j.rser.2016.03.024.

[26] S. Amesöder, Wärmeleitende Kunststoffe für das Spritzgießen. Dissertation, Erlangen-Nürnberg, 2010.

[27] C. Heinle, Simulationsgestützte Entwicklung von Bauteilen aus wärmeleitenden Kunststoffen. Dissertation, Erlangen-Nürnberg, 2012.

[28] G.W. Ehrenstein, Polymer-Werkstoffe: Struktur - Eigenschaften - Anwendung, 3rd ed., Hanser, München, 2011.

[29] H.O. Pierson, Handbook of carbon, graphite, diamond, and fullerenes: Properties, processing, and applications, Noyes Publications, Park Ridge, N.J, 1993.

[30] D.H. Kaelble, Dispersion-Polar Surface Tension Properties of Organic Solids, J. Adhes. 2 (1970) 66–81. 10.1080/0021846708544582.

[31] D.K. Owens, R.C. Wendt, Estimation of the surface free energy of polymers, J. Appl. Polym. Sci. 13 (1969) 1741–1747. 10.1002/app.1969.070130815.

[32] W. Rabel, Einige Aspekte der Benetzungstheorie und ihre Anwendung auf die Untersuchung und Veränderung der Oberflächeneigenschaften von Polymeren, Farbe und Lack 77 (1971) 997–1005.

[33] S. Wu, Calculation of interfacial tension in polymer systems, J. polym. sci., C Polym. symp. 34 (1971) 19–30. 10.1002/polc.5070340105.

[34] T. Young, III. An essay on the cohesion of fluids, Phil. Trans. R. Soc. 95 (1805) 65–87. 10.1098/rstl.1805.0005.

[35] F.M. Fowkes, Attractive forces at interfaces, Ind. Eng. Chem. 56 (1964) 40–52.

[36] R. David, J. Spelt, J. Zhang, D. Kwok, Contact Angles and Solid Surface Tensions, in: A.W. Neumann, R. David, Y. Zuo (Eds.), Applied surface thermodynamics, 2nd ed., CRC Press, Boca Raton, FL, 2010, pp. 491–554.

[37] R.N. Wenzel, Resistance of Solid Surfaces to Wetting by Water, Ind. Eng. Chem. 28 (1936) 988–994. 10.1021/ie50320a024.

[38] A.B.D. Cassie, S. Baxter, Wettability of porous surfaces, Trans. Faraday Soc. 40 (1944) 546. 10.1039/tf9444000546.

[39] A. Marmur, Wetting on Hydrophobic Rough Surfaces: To Be Heterogeneous or Not To Be?, Langmuir 19 (2003) 8343–8348. 10.1021/la0344682.

[40] H.J. Busscher, A. van Pelt, P. de Boer, H.P. de Jong, J. Arends, The effect of surface roughening of polymers on measured contact angles of liquids, Colloids Surf. 9 (1984) 319–331. 10.1016/0166-6622(84)80175-4.

[41] S. Palzer, C. Hiebl, K. Sommer, H. Lechner, Einfluss der Rauhigkeit einer Feststoffoberfläche auf den Kontaktwinkel, Chem. Ing. Tech. 73 (2001) 1032–1038. 10.1002/1522-2640(200108)73:8<1032:AID-CITE1032>3.0.CO;2-K.

[42] ANSYS, Inc., Ansys Mechanical ™, ANSYS, Inc.

[43] T.A. Osswald, E. Baur, S. Brinkmann, K. Oberbach, E. Schmachtenberg, International plastics handbook: The resource for plastics engineers, 4th ed., Hanser, Munich, 2006.

[44] G. Martins, R.S. Santiago, L.E. Beckedorff, T.S. Possamai, R. Oba, J. Oliveira, A. de Oliveira, K.V. Paiva, Structural analysis of gasketed plate heat exchangers, Int. J. Press. Vessels Pip. 197 (2022) 104634. 10.1016/j.ijpvp.2022.104634.

[45] M. Ali, A. Ul-Hamid, L.M. Alhems, A. Saeed, Review of common failures in heat exchangers – Part I: Mechanical and elevated temperature failures, Eng. Fail. Anal. 109 (2020) 104396. 10.1016/j.engfailanal.2020.104396.

[46] A.S. Pelliccione, R. SantAnna, M. Siqueira, A.F. Ribeiro, J.E. Ramos, O.P. Silva, M.F. Pimentel, Failure analysis of a titanium plate heat exchanger – Mechanical fatigue, Eng. Fail. Anal. 105 (2019) 1172–1188. 10.1016/j.engfailanal.2019.07.059.

[47] The Dow Chemical Company, DOWLEX^{TM} 2388 Polyethylene Resin, 2005.

[48] S.-H. Chung, H. Kim, S.W. Jeong, Improved thermal conductivity of carbon-based thermal interface materials by high-magnetic-field alignment, Carbon 140 (2018) 24–29. 10.1016/j.carbon.2018.08.029.

[49] A. Leipertz, J3 Tropfenkondensation, in: VDI-Wärmeatlas, Springer Berlin Heidelberg, Berlin, Heidelberg, 2013, pp. 1041–1046.

[50] A. Stärk, K. Krömer, K. Loisel, K. Odiot, S. Nied, H. Glade, Impact of Tube Surface Properties on Crystallization Fouling in Falling Film Evaporators for Seawater Desalination, Heat Transfer Eng. 38 (2017) 762–774. 10.1080/01457632.2016.1206418.

[51] S. Keysar, R. Semiat, D. Hasson, J. Yahalom, Effect of Surface Roughness on the Morphology of Calcite Crystallizing on Mild Steel, J. Colloid Interface Sci. 162 (1994) 311–319. 10.1006/jcis.1994.1044.

[52] Fouling in membranes and thermal units, 2007.

[53] W. Pohl, Einfluß der Wandrauhigkeit auf den Wärmeübergang an Wasser, Forsch Ing-Wes 4 (1933) 230–237. 10.1007/BF02719757.

[54] R.P. Taylor, M.H. Hosni, J.W. Garner, H.W. Coleman, Thermal boundary condition effects on heat transfer in turbulent rough-wall boundary layers, Wärme- und Stoffübertragung 27 (1992) 131–140. 10.1007/bf01599926.

[55] T. Kuppan, Heat Exchanger Design Handbook, 2nd ed., CRC Press, Hoboken, 2013.

[56] B. Zohuri, Compact Heat Exchangers, Springer International Publishing, Cham, 2017.

[57] W.L. Wilkinson, Flow Distribution in Plate Heat-Exchangers, Chem. Eng. (Chemical Engineer) (1974) 289–292.

[58] H. Martin, A theoretical approach to predict the performance of chevron-type plate heat exchangers, Chem. Eng. Process. Process Intensif. 35 (1996) 301–310. 10.1016/0255-2701(95)04129-X.

[59] B. Kumar, A. Soni, S.N. Singh, Effect of geometrical parameters on the performance of chevron type plate heat exchanger, Exp. Therm Fluid Sci. 91 (2018) 126–133. 10.1016/j.expthermflusci.2017.09.023.

[60] R.M. Manglik, Plate heat exchangers for process industry applications: enhanced thermal-hydraulic characteristics of chevron plates, in: R.M. Manglik, A.D. Kraus (Eds.), Process, enhanced, and multiphase heat transfer: A festschrift for A. E. Bergles ; [compilation of all papers presented at the Arthur E. Bergles Symposium held at the Georgia Institute of Technology in Atlanta, Georgia on November 16, 1996, Begel House, New York, 1996, pp. 267–276.

[61] R.M. Manglik, A. Muley, Heat Transfer and Pressure Drop Characteristics of Plate-and-Frame Heat Exchangers: A Literature Review, Thermal-Fluids Laboratory, Department of Mechanical, Industrial and Nuclear …, Cincinnati, OH, 1993.

[62] Alfa Laval AB, Plattenwärmetauscher im Überblick | Alfa Laval, 2023, https://www.alfalaval.de/produkte/waermeuebertragung/plattenwaermetauscher/uebersicht/, accessed 7 March 2023.

[63] Kelvion Holding GmbH, Produkte, 2023, https://www.kelvion.com/de/produkte/kategorie/plattenwaermetauscher/, accessed 7 March 2023.

[64] Tranter, Inc., Wärmetauscher - Tranter, 2023, https://www.tranter.com/de/heat-exchangers/, accessed 7 March 2023.

[65] S.G. Kandlikar, R.K. Shah, Multipass Plate Heat Exchangers—Effectiveness-NTU Results and Guidelines for Selecting Pass Arrangements, J. Heat Transfer 111 (1989) 300–313. 10.1115/1.3250678.

[66] A. Muley, R.M. Manglik, Experimental Study of Turbulent Flow Heat Transfer and Pressure Drop in a Plate Heat Exchanger With Chevron Plates, J. Heat Transfer 121 (1999) 110–117. 10.1115/1.2825923.

[67] H. Kumar, The plate heat exchanger: construction and design, in: Institute of Chemical Engineering Symposium Series, 1984, pp. 1275–1288.

[68] A.S. Wanniarachchi, U. Ratnam, B.E. Tilton, K. Dutta-Roy, Approximate correlations for chevron-type plate heat exchangers, in: V. Sernas, R.D. Boyd, M.K. Jensen (Eds.), Proceedings of the 30th National Heat Transfer Conference, vol. 12, 1995, pp. 145–151.

[69] J. Hartung, B. Elpelt, K.-H. Klösener, Statistik, DE GRUYTER, 2002.

[70] ANSYS, Inc., ANSYS® Fluent®, ANSYS, Inc.

[71] ANSYS, Inc., Ansys Workbench™, ANSYS, Inc.

[72] ANSYS, Inc., Ansys Fluent User's Guide. Release 2021 R2, 2021.

[73] H. Schlichting, Boundary-Layer Theory, 9th ed., Springer Berlin Heidelberg, Berlin, Heidelberg, 2016.

[74] W.W. Focke, P.G. Knibbe, Flow visualization in parallel-plate ducts with corrugated walls, J. Fluid Mech. 165 (1986) 73. 10.1017/S0022112086003002.

[75] H.M. Metwally, R.M. Manglik, Enhanced heat transfer due to curvature-induced lateral vortices in laminar flows in sinusoidal corrugated-plate channels, Int. J. Heat Mass Transfer 47 (2004) 2283–2292. 10.1016/j.ijheatmasstransfer.2003.11.019.

[76] A. Muley, R.M. Manglik, H.M. Metwally, Enhanced Heat Transfer Characteristics of Viscous Liquid Flows in a Chevron Plate Heat Exchanger, J. Heat Transfer 121 (1999) 1011–1017. 10.1115/1.2826051.

[77] I. Astrouski, M. Raudensky, M. Dohnal, Particulate fouling of polymeric hollow fiber heat exchanger, in: M.R. Malayeri, H. Müller-Steinhagen, A.P. Watkinson (Eds.), Proceedings of 10th International Conference on Heat Exchanger Fouling and Cleaning, 2013, pp. 233–239.

[78] P. Bandelier, C.J. Deronzier, F. Lauro, Plastic heat exchangers, Matériaux & Techniques 80 (1992) 67–70. 10.1051/mattech/199280090067.

[79] R.J. Jachuck, C. Ramshaw, Process Intensification-Polymer Film Compact Heat-Exchanger (Pfche), Chem. Eng. Res. Des. 72 (1994) 255–262.

[80] L. Zaheed, R. Jachuck, Performance of a square, cross-corrugated, polymer film, compact, heat-exchanger with potential application in fuel cells, J. Power Sources 140 (2005) 304–310. 10.1016/j.jpowsour.2004.08.024.

[81] P.J. Heggs, H.-J. Scheidat, Thermal performance of plate heat exchangers with flow maldistribution, in: R.K. Shah, T.M. Rudy, J.M. Robertson, K.M. Hostetler (Eds.), Compact heat exchangers for power and process industries: Presented at the 28th National Heat Transfer Conference and Exhibition, San Diego, California, August 9-12, 1992, American Society of Mechanical Engineers, New York, 1992, pp. 87–93.

[82] S. Jin, P. Hrnjak, Effect of end plates on heat transfer of plate heat exchanger, Int. J. Heat Mass Transfer 108 (2017) 740–748. 10.1016/j.ijheatmasstransfer.2016.11.106.

[83] N. Epstein, Thinking about Heat Transfer Fouling: A 5 × 5 Matrix, Heat Transfer Eng. 4 (1983) 43–56. 10.1080/01457638108939594.

[84] H. Müller-Steinhagen (Ed.), Handbook heat exchanger fouling: Mitigation and cleaning technologies, 2nd ed., PP Publico Publ, Essen, 2011.

[85] T.R. Bott, Fouling of heat exchangers, Elsevier, Amsterdam, New York, 1995.

[86] T.R. Bott, Aspects of crystallization fouling, Exp. Therm Fluid Sci. 14 (1997) 356–360. 10.1016/S0894-1777(96)00137-9.

[87] H. Müller-Steinhagen, C4 Verminderung der Ablagerungsbildung in Wärmeübertragern, in: VDI-Wärmeatlas, Springer Berlin Heidelberg, Berlin, Heidelberg, 2013, pp. 91–122.

[88] J. Bucko, M. Mayer, W. Benzinger, W. Augustin, S. Scholl, R. Dittmeyer, Untersuchungen zum Kristallisationsfouling in Mikrowärmeübertragern, Chem. Ing. Tech. 84 (2012) 491–502. 10.1002/cite.201100234.

[89] B. Bansal, X.D. Chen, H. Müller-Steinhagen, Analysis of 'classical' deposition rate law for crystallisation fouling, Chem. Eng. Process. Process Intensif. 47 (2008) 1201–1210. 10.1016/j.cep.2007.03.016.

[90] A. Helalizadeh, H. Müller-Steinhagen, M. Jamialahmadi, Mathematical modelling of mixed salt precipitation during convective heat transfer and sub-cooled flow boiling, Chem. Eng. Sci. 60 (2005) 5078–5088. 10.1016/j.ces.2005.03.040.

[91] F. Brahim, W. Augustin, M. Bohnet, Numerical simulation of the fouling process, Int. J. Therm. Sci. 42 (2003) 323–334. 10.1016/S1290-0729(02)00021-2.

[92] T.M. Pääkkönen, M. Riihimäki, C.J. Simonson, E. Muurinen, R.L. Keiski, Modeling CaCO3 crystallization fouling on a heat exchanger surface – Definition of fouling layer properties and model parameters, Int. J. Heat Mass Transfer 83 (2015) 84–98. 10.1016/j.ijheatmasstransfer.2014.11.073.

[93] S.N. Kazi, Fouling and Fouling Mitigation on Heat Exchanger Surfaces, in: J. Mitrovic (Ed.), Heat Exchangers - Basics Design Applications, InTech, 2012, pp. 507–532.

[94] C. Dreiser, L.J. Krätz, H.-J. Bart, Kinetics and Quantity of Crystallization Fouling on Polymer Surfaces: Impact of Surface Characteristics and Process Conditions, Heat Transfer Eng. 36 (2015) 715–720. 10.1080/01457632.2015.954954.

[95] W. Augustin, J. Zhang, I. Bialuch, T. Geddert, S. Scholl, Modifizierte Oberflächenbeschichtungen zur Foulingminderung auf wärmeübertragenden Flächen, Chem. Ing. Tech. 78 (2006) 607–612. 10.1002/cite.200500141.

[96] T.M. Pääkkönen, M. Riihimäki, C.J. Simonson, E. Muurinen, R.L. Keiski, Crystallization fouling of CaCO3 – Analysis of experimental thermal resistance and its uncertainty, Int. J. Heat Mass Transfer 55 (2012) 6927–6937. 10.1016/j.ijheatmasstransfer.2012.07.006.

[97] B. Bansal, H. Müller-Steinhagen, X.D. Chen, Performance of plate heat exchangers during calcium sulphate fouling — investigation with an in-line filter, Chem. Eng. Process. Process Intensif. 39 (2000) 507–519. 10.1016/S0255-2701(00)00098-2.

[98] M. Mortean, M. Mantelli, Nusselt number correlation for compact heat exchangers in transition regimes, Appl. Therm. Eng. 151 (2019) 514–522. 10.1016/j.applthermaleng.2019.02.017.

[99] H.D. Baehr, K. Stephan, Wärme- und Stoffübertragung, Springer Berlin Heidelberg, Berlin, Heidelberg, 2019.

[100] W.L. Ryan, E.A. Hemmingsen, Bubble Formation at Porous Hydrophobic Surfaces, J. Colloid Interface Sci. 197 (1998) 101–107. 10.1006/jcis.1997.5219.

[101] W.L. Ryan, E.A. Hemmingsen, Bubble Formation in Water at Smooth Hydrophobic Surfaces, J. Colloid Interface Sci. 157 (1993) 312–317. 10.1006/jcis.1993.1191.

[102] P. Roach, N.J. Shirtcliffe, M.I. Newton, Progess in superhydrophobic surface development, Soft Matter 4 (2008) 224–240. 10.1039/B712575P.

[103] S.M. Peyghambarzadeh, A. Vatani, M. Jamialahmadi, Influences of bubble formation on different types of heat exchanger fouling, Appl. Therm. Eng. 50 (2013) 848–856. 10.1016/j.applthermaleng.2012.07.015.

[104] H. Kiepfer, W. Omar, T. Schröder, H.-J. Bart, Polymer Film Heat Transfer Surfaces in Seawater Desalination: Fouling Layer Formation and Technology, Chem. Eng. Technol. 43 (2020) 1205–1213. 10.1002/ceat.201900492.

[105] F. Albert, W. Augustin, S. Scholl, Roughness and constriction effects on heat transfer in crystallization fouling, Chem. Eng. Sci. 66 (2011) 499–509. 10.1016/j.ces.2010.11.021.

[106] B.D. Crittenden, N.J. Alderman, Mechanisms by Which Fouling Can Increase Overall Heat Transfer Coefficients, Heat Transfer Eng. 13 (1992) 32–41. 10.1080/01457639208939786.

[107] A.D. Smith, E. Hitimana, Incorporation of Fouling Deposit Measurements in Crude Oil Fouling Testing and Data Analysis, in: H.U. Zettler, E. Ishiyama (Eds.), Proceedings of the 14th International Conference on Heat Exchanger Fouling and Cleaning, 2022.

[108] J.A. Barish, J.M. Goddard, Anti-fouling surface modified stainless steel for food processing, Food Bioprod. Process. 91 (2013) 352–361. 10.1016/j.fbp.2013.01.003.

[109] H. Müller-Steinhagen, Q. Zhao, A. Helali-Zadeh, X.-G. Ren, The effect of surface properties on CaSO 4 scale formation during convective heat transfer and subcooled flow boiling, Can. J. Chem. Eng. 78 (2000) 12–20. 10.1002/cjce.5450780105.

[110] Q. Zhao, Y. Liu, S. Wang, Surface modification of water treatment equipment for reducing CaSO4 scale formation, Desalination 180 (2005) 133–138. 10.1016/j.desal.2005.01.002.

[111] P.C. Zielke, Experimental investigation of the motion of droplets on surfaces with a gradient in wettability. PhD thesis, Erlangen-Nürnberg, 2008.

[112] D. Quéré, Wetting and Roughness, Annu. Rev. Mater. Res. 38 (2008) 71–99. 10.1146/annurev.matsci.38.060407.132434.

[113] S.N. Kazi, G.G. Duffy, X.D. Chen, Mineral scale formation and mitigation on metals and a polymeric heat exchanger surface, Appl. Therm. Eng. 30 (2010) 2236–2242. 10.1016/j.applthermaleng.2010.06.005.

[114] H. Müller-Steinhagen, Q. Zhao, Intermolecular and Adhesion Forces of Deposits on Modified Heat Transfer Surfaces, in: H. Müller-Steinhagen (Ed.), Proceedings of the 4th International Conference on Heat Exchanger Fouling: Fundamental Approaches & Technical Solutions, Davos, Switzerland, July 8 - 13, 2001, Publico-Publ, Essen, 2002.

[115] T. Geddert, W. Augustin, S. Scholl, Induction Time in Crystallization Fouling on Heat Transfer Surfaces, Chem. Eng. Technol. 34 (2011) 1303–1310. 10.1002/ceat.201000469.

[116] Z. Wu, J.H. Davidson, L.F. Francis, Effect of water chemistry on calcium carbonate deposition on metal and polymer surfaces, J. Colloid Interface Sci. 343 (2010) 176–187. 10.1016/j.jcis.2009.11.031.

[117] Z. Wu, L.F. Francis, J.H. Davidson, Scale formation on polypropylene and copper tubes in mildly supersaturated tap water, Sol. Energy 83 (2009) 636–645. 10.1016/j.solener.2008.10.012.

[118] N. Andritsos, A. Karabelas, Calcium carbonate scaling in a plate heat exchanger in the presence of particles, Int. J. Heat Mass Transfer 46 (2003) 4613–4627. 10.1016/S0017-9310(03)00308-9.

[119] E. Lee, J. Jeon, H. Kang, Y. Kim, Thermal resistance in corrugated plate heat exchangers under crystallization fouling of calcium sulfate (CaSO4), Int. J. Heat Mass Transfer 78 (2014) 908–916. 10.1016/j.ijheatmasstransfer.2014.07.069.

A Appendix Measurement and Simulation Data

Plate heat exchanger measurement data

Tab. A.1: Experimentally determined overall heat transfer coefficients for the operating conditions given in Tab. 3.2. PP-G. Parallel flow. *s* = 2 mm.

U	$B_{U,95\,\%}$	Q	$B_{Q,95\,\%}$	Re_h	Re_c	$T_{h,in}$	$T_{c,in}$	N_{tp}
kW/m²K	kW/m²K	W	W	-	-	°C	°C	-
752	10.81	298.8	4.16	810.9	821.7	80.1	40.1	1
751	52.14	301.2	20.89	816.7	980	80.1	40	1
773.3	101.8	309.2	40.68	778.7	1207	80	40.1	1
784.9	48.72	316.7	19.66	820.1	1406	80.1	40	1
797.2	99.01	320.9	39.81	818.2	1606	80	40.1	1
771	13.03	308.1	5.161	1002	818.8	79.9	40.1	1
797.4	8.543	318.4	3.364	987.8	999.4	79.6	40	1
809	8.157	324.6	3.256	989.1	1201	79.6	40	1
817.7	9.883	329.8	3.869	1005	1416	79.6	40	1
821.5	10.55	332.3	4.145	1016	1608	79.6	40	1
779.8	16.35	315.6	6.641	1222	817.5	79.9	40	1
807.5	8.865	327.7	3.533	1220	999.8	79.8	40	1
816.1	8.044	332.5	3.244	1211	1201	79.8	40	1
824.1	14.11	337.0	5.757	1207	1416	79.8	40	1
828.8	11.07	339.5	4.512	1208	1605	79.8	40	1
790	11.8	320.2	4.79	1428	818.8	80	40.2	1
811	8.841	332.2	3.586	1420	999.6	79.9	40	1
818.6	10.06	336.8	4.1	1410	1202	79.9	40	1
826.2	10.95	341.4	4.5	1416	1416	79.9	40	1
832.9	13.23	344.3	5.481	1390	1603	79.9	40	1
794.8	14.72	324.5	6.016	1625	822.3	80	40.1	1
810.9	8.528	334.8	3.48	1625	999	80	40	1
821.2	9.74	340.4	4	1605	1202	80	40	1
828.7	12.06	344.8	4.982	1587	1414	80	40	1
841.6	17.81	350.9	7.433	1636	1611	80	40	1

Tab. A.2: Experimentally determined overall heat transfer coefficients for the operating conditions given in Tab. 3.2. PP-G. Countercurrent flow. s = 2 mm.

U	$B_{U,95\,\%}$	Q	$B_{Q,95\,\%}$	Re_h	Re_c	$T_{h,in}$	$T_{c,in}$	N_{tp}
kW/m²K	kW/m²K	W	W	-	-	°C	°C	-
763.3	25.43	230.6	7.653	823.1	808.5	70.1	40	1
762	9.321	231.5	2.81	806.4	997.7	70.1	40	1
789.8	9.946	239.5	2.996	805	1189	69.9	40	1
809.2	10.5	245.9	3.166	806.6	1408	70	40	1
823.9	11.52	251.2	3.489	806	1607	70	40	1
779.8	12.43	237.3	3.756	1000	808	70	40	1
805.4	24.83	245.4	7.545	999.2	997	70	40	1
804.8	10.58	247.4	3.207	1001	1187	70	40	1
816.6	10.57	250.9	3.165	979.2	1407	70	40	1
841.5	11.55	259.1	3.528	998.3	1607	70	40	1
778.6	12.03	238.4	3.653	1188	809.8	70	40	1
783.5	9.944	241.6	3.022	1193	995.8	70	40	1
818.4	21.9	253.3	6.742	1212	1191	70	40	1
821.8	10.11	255	3.105	1197	1407	70	40	1
845.9	11	263	3.39	1195	1606	70	40	1
785.1	12.14	242.3	3.716	1421	812.4	70	40	1
786.9	9.834	244.2	3.029	1421	994.7	70	40	1
809.5	10.8	252	3.321	1383	1187	70	40	1
835.4	11.01	261.3	3.424	1419	1407	70	40	1
850.6	11.57	266.1	3.585	1393	1606	70	40	1
788.4	12.34	244.3	3.786	1606	814	70	40	1
791.1	17.03	246.9	5.268	1596	992.1	70	40	1
811.3	9.545	254.3	2.967	1609	1217	70	40	1
824	11.32	259	3.528	1607	1404	70	40	1
854.6	11.39	269	3.541	1594	1605	70	40	1
755.5	9.805	301	3.764	832.2	809.5	79.9	40	1
759.7	12.01	305.2	4.74	815.9	1009	80	40	1
761.8	12.1	307.2	4.805	814.9	1207	79.9	39.9	1
775.8	9.459	313.4	3.801	817.9	1398	80	40	1
791.5	10.82	319.9	4.142	800.5	1598	80	40	1
776.8	14.64	312.9	5.827	993.4	816	80	39.9	1
787.5	9.419	318.4	3.743	991.4	1011	79.9	40	1
776.8	13.35	316.9	5.401	996.2	1208	80	39.9	1

U	$B_{U,95\,\%}$	Q	$B_{Q,95\,\%}$	Re_h	Re_c	$T_{h,in}$	$T_{c,in}$	N_{tp}
kW/m²K	kW/m²K	W	W	-	-	°C	°C	-
791.8	9.668	323.3	3.926	992.6	1399	80	40	1
810	11.21	331.4	4.468	1010	1598	80	40	1
783.2	13.53	318.7	5.484	1210	818.4	80	39.9	1
792.1	12.64	323.9	5.123	1204	1006	80	40	1
802.9	10.74	329.7	4.386	1209	1210	80	40	1
800.6	10.12	330.1	4.15	1209	1401	80	40	1
819.2	10.1	338.7	4.16	1210	1600	80	40	1
791.8	13.34	323.5	5.428	1396	820.9	80	40	1
798.5	12.38	328.5	5.064	1402	1006	80	40	1
789	11.4	326.8	4.697	1420	1212	80	40	1
814.8	9.999	337.9	4.125	1426	1410	80	40	1
834.2	10.51	347	4.35	1422	1601	80	40	1
797.2	13.38	327.4	5.478	1610	820.9	80	40	1
804.5	14.01	332.9	5.782	1609	1005	80	40	1
804.2	11.32	334.7	4.679	1609	1213	80	40	1
809.3	10.67	337.8	4.43	1608	1402	80	40	1
826.1	11.3	345.1	4.705	1641	1606	80	40	1
644.7	17.72	503.8	12.55	407.3	389.6	70	40	3
692.9	16.58	577.4	13.46	598.5	600.9	70	40	3
737.7	9.772	637.5	7.94	813.3	804.9	70	40	3
739.4	8.47	654.7	7.227	978.6	995.4	70	40	3
763.6	10.56	688.9	9.146	1206	1192	70	40	3
773.5	13.67	707.5	12.09	1415	1401	70	40	3
592.6	7.857	689.7	7.344	266	266.8	70	40	5
679.7	8.736	908.8	10.43	547.8	535.9	70	40.1	5
710.7	8.671	1007	11.52	792.5	794.7	70	40.1	5
731.3	10.37	1072	14.57	1049	1067	70	40.1	5
568.8	17.06	1105	26.34	210.5	204.1	80	40.1	7
611.7	14.43	1297	24.3	411.1	209.3	80	40.1	7
622.4	19.94	1367	34.54	607.9	210.9	79.9	40.1	7
599.4	7.776	1246	13.52	215.2	410.3	80	40.1	7
659	8.104	1501	16.44	396.8	399.2	80	40	7
642.8	10.66	1552	22.38	588.3	398.3	80	40	7

U	$B_{U,95\,\%}$	Q	$B_{Q,95\,\%}$	Re_h	Re_c	$T_{h,in}$	$T_{c,in}$	N_{tp}
kW/m²K	kW/m²K	W	W	-	-	°C	°C	-
669.6	10.6	1644	23.8	587.1	599	79.4	40	7
543.8	18.99	813.4	23.96	193.8	204.4	69.9	40	7
603.3	20.93	979.2	30.71	397.1	207.9	70	40	7
561.9	15.85	970.4	22.34	615	210.4	70	40.1	7
658.6	14.61	1008	13.1	207.5	398.8	69.9	40	7
673.3	14.51	1168	21.95	393.9	408.7	70	40.1	7
692.9	19.23	1256	30.38	607.7	401.8	70	40.1	7
658.7	9.676	1043	12.46	212	597	69.9	40	7
686.4	8.663	1226	13.63	393.9	600.3	70	40.1	7
697.8	12.39	1314	21.28	605.6	589.9	70	40.1	7

Tab. A.3: Experimentally determined overall heat transfer coefficients for the operating conditions given in Tab. 3.2. PPS-G. Countercurrent flow.

U	$B_{U,95\,\%}$	Q	$B_{Q,95\,\%}$	Re_h	Re_c	$T_{h,in}$	$T_{c,in}$	N_{tp}	s
kW/m²K	kW/m²K	W	W	-	-	°C	°C	-	*mm*
638.5	15.68	188.3	4.596	612.7	598.1	69.9	40.2	1	2.5
696.5	11.03	209.7	3.311	809.2	795.6	70	40.2	1	2.5
718.7	11.83	219.7	3.6	1001	997.2	70	40.2	1	2.5
734.6	8.673	227.4	2.669	1187	1210	70	40.2	1	2.5
746	9.597	233.3	2.973	1415	1415	70	40.2	1	2.5
755.8	10.94	238.1	3.431	1610	1615	70	40.2	1	2.5
1284	28.63	345.4	7.582	589.2	611.7	69.9	39.8	1	0.85
1595	32.45	433.7	8.685	789.5	795.8	70	39.9	1	0.85
1689	26.1	473.2	6.794	999	995.5	70	39.9	1	0.85
1741	18.16	499.8	4.852	1201	1203	70	39.9	1	0.85
1771	17.18	517.4	4.885	1390	1400	70	39.9	1	0.85
1804	18.25	533.5	5.244	1580	1603	70	39.9	1	0.85

Tab. A.4: Experimentally determined overall heat transfer coefficients for the operating conditions given in Tab. 3.2. PP-G degassed. Countercurrent flow. s = 2 mm.

U	$B_{U,95\,\%}$	Q	$B_{Q,95\,\%}$	Re_h	Re_c	$T_{h,in}$	$T_{c,in}$	N_{tp}
kW/m²K	kW/m²K	W	W	-	-	°C	°C	-
502.2	18.08	770.7	24.55	190.5	203.1	70	40	7

651.8	18.06	1032	27.12	395.1	208.6	70	40	7
661	17.57	1090	27.77	602.1	209.8	70.1	40	7
587	13.27	922.1	13.09	196.4	394.3	70	40.1	7
610.4	160.1	994.8	204	262.8	395.5	69.9	40	7
681.1	8.455	1241	13.5	600.1	400.5	70	40.1	7
443.8	8.997	775.1	12.7	197.1	597	70	40.1	7
631.4	7.935	1149	13.19	399.3	603.8	70	40.1	7
655	7.739	1253	13.46	607.5	605.5	70.1	40.1	7

Simulation results

Tab. A.5: Simulated convective heat transfer coefficients and Nusselt numbers. Two lines represent one configuration (h_c and h_h, respectively).

h	Nu	s	λ_W	Re	Pr	T_{ref}	ΔT	N_{tp}
kW/m²K	-	mm	W/mK	-	-	°C	°C	-
12.885	53.69	0.25	16.2	1000	4.58	40.81	20	4
9.606	40.02	0.25	16.2	1000	3.32	59.44	20	4
8.822	36.76	0.25	16.2	500	4.58	41.17	20	4
6.519	27.16	0.25	16.2	500	3.32	59.21	20	4
12.915	53.81	0.25	16.2	1000	4.58	41.17	30	4
8.835	36.81	0.25	16.2	1000	2.88	69.05	30	4
19.232	80.13	0.25	16.2	2000	4.58	40.51	20	4
14.925	62.19	0.25	16.2	2000	3.32	59.64	20	4
8.716	36.32	0.25	16.2	500	4.58	41.35	20	4
10.652	44.38	0.25	16.2	1000	3.32	59.04	20	4
8.660	36.08	0.25	16.2	500	4.58	41.53	20	4
14.920	62.17	0.25	16.2	2000	3.32	59.74	20	4
13.014	54.22	0.25	16.2	1000	4.58	40.69	20	4
6.478	26.99	0.25	16.2	500	3.32	59.10	20	4
12.838	53.49	0.25	16.2	1000	4.58	40.94	20	4
14.882	62.01	0.25	16.2	2000	3.32	59.69	20	4
19.392	80.8	0.25	16.2	2000	4.58	40.36	20	4
6.479	26.99	0.25	16.2	500	3.32	59.01	20	4
19.361	80.67	0.25	16.2	2000	4.58	40.44	20	4
9.612	40.05	0.25	16.2	1000	3.32	59.37	20	4
12.922	53.84	0.25	16.2	1000	4.58	41.53	40	4
8.268	34.45	0.25	16.2	1000	2.53	78.60	40	4
14.433	60.14	0.25	16.2	1000	5.55	31.89	60	4
7.796	32.48	0.25	16.2	1000	2.27	87.66	60	4
14.762	61.51	0.25	1.13	1000	4.58	40.21	20	4
10.596	44.15	0.25	1.13	1000	3.32	59.85	20	4
12.309	51.29	0.25	100	1000	4.58	41.05	20	4
9.333	38.89	0.25	100	1000	3.32	59.27	20	4
11.756	48.99	0.25	16.2	1000	3.87	50.90	20	4
8.844	36.85	0.25	16.2	1000	2.88	69.39	20	4

h	Nu	s	λ_W	Re	Pr	T_{ref}	ΔT	N_{tp}
kW/m²K	-	mm	W/mK	-	-	°C	°C	-
10.746	44.78	0.25	16.2	1000	3.32	60.98	20	4
8.283	34.51	0.25	16.2	1000	2.53	79.34	20	4
17.593	58.64	0	16.2	1000	4.58	41.09	20	4
13.223	44.08	0	16.2	1000	3.32	59.29	20	4
8.177	54.51	1	16.2	1000	4.58	40.90	20	4
6.088	40.58	1	16.2	1000	3.32	59.41	20	4
9.989	49.95	0.5	16.2	1000	4.58	40.85	20	4
7.995	39.97	0.5	16.2	1000	3.32	59.46	20	4
5.757	57.57	2	16.2	1000	4.58	40.89	20	4
4.389	43.89	2	16.2	1000	3.32	59.42	20	4
11.696	48.73	0.25	16.2	1000	4.58	40.85	20	6
9.915	41.31	0.25	16.2	1000	3.32	59.26	20	6

B Appendix Author Information

Declaration of authorship

This dissertation contains material that has been previously published in scientific journals. These publications are listed below, along with a note of the author's contribution to this dissertation.

H. Kiepfer; P. Stannek; M. Kuypers; M. Grundler; H.-J. Bart. Highly Conductive Thin-Walled Polypropylene/Graphite Composites as Heat Transfer Surfaces in Corrosive Media, in: HEFAT (Ed.), Proceedings of the 15th International Conference on Heat Transfer, Fluid Mechanics and Thermodynamics (HEFAT2021), 2021, pp. 1174–1179, ISBN: 978-1-77592-216-2.

H. Kiepfer, P. Stannek, M. Kuypers, M. Grundler, H.-J. Bart, The potential of thermally conductive polymer composites regarding crystallization fouling mitigation, Heat Mass Transfer (2023). 10.1007/s00231-023-03398-0.

H. Kiepfer, P. Stannek, M. Grundler, H.-J. Bart, Thermally conductive polypropylene composites as corrosion-resistant materials for plate heat exchangers, Polym. Compos. (2023). 10.1002/pc.27613.

H. Kiepfer, P. Stannek, M. Grundler, H.-J. Bart, Development and thermal performance of a thermoplastic-graphite-composite based plate heat exchanger for use in corrosive media, Appl. Therm. Eng. (2023) 121581. 10.1016/j.applthermaleng.2023.121581.

The author (Hendrik Kiepfer) developed parts of the experimental setups, including the polymer composite plate heat exchanger, the mathematical models and methodology, and performed major parts of the laboratory work and simulations. He derived the presented theory using the given literature and wrote the manuscripts in cooperation with the co-authors. Hans-Jörg Bart supervised the present dissertation. The present dissertation (or parts of it) has not been submitted to any state, department, university, or other scientific examination for credit.

Student theses

The following student theses were prepared under the supervision of the author of the present dissertation in the framework of his research.

M. Griebel, CFD Simulation of Fouling Processes with Ansys Fluent. Bachelorarbeit, Kaiserslautern, 2023.

D. Lukas, Evaluierung von Polymerkompositen für den Einsatz in thermischen Meerwasserentsalzungsanlagen. Forschungsarbeit, Kaiserslautern, 2023.

C. Effen, CFD-Simulation eines Plattenwärmeübertragers in Ansys Fluent. Masterarbeit, Kaiserslautern, 2022.

L. Weidler, Experimentelle und theoretische Untersuchungen eines Polymerkomposit-Plattenwärmeübertragers. Studienarbeit, Kaiserslautern, 2022.

K. Bender, CFD-Simulation von Kristallisationsfoulingprozessen mit Ansys Fluent. Studienarbeit, Kaiserslautern, 2022.

A. Reihle, Modellierung und Simulation von Kristallisationsfoulingprozessen in Plattenwärmeübertragern. Masterarbeit, Kaiserslautern, 2022.

A. William, Experimentelle und theoretische Untersuchungen zur Anwendbarkeit von Polymerkomposit-Plattenwärmeübertragern in foulinganfälligen Systemen. Diplomarbeit, Kaiserslautern, 2022.

M. Hofmann, Modellgestütze Auslegung eines Polymerkomposit-Plattenwärmeübertragers. Masterarbeit, Kaiserslautern, 2021.

A. William, Untersuchung von Polymer-Graphit-Kompositen zur Anwendung in Plattenwärmeübertragern. Studienarbeit, Kaiserslautern, 2021.

R. Raab, Charakterisierung hochgefüllter Kunststoffelemente in Hinsicht auf die Anwendung als Wärmeübertragerelemente. Masterarbeit, Kaiserslautern, 2021.

M.A. Raether, Mathematische Modellierung von Foulingprozessen in Gegenstromwärmeübertragern. Bachelorarbeit, Kaiserslautern, 2021.

S. Aupke, Auslegung und Simulation einer Plattenwärmeübertrager-Testzelle. Bachelorarbeit, Kaiserslautern, 2021.

K. Aldaboussi, Modellierung des Wärme- und Stoffübergangs in einem Verfahren zur großflächigen solaren Meerwasserentsalzung. Studienarbeit, Kaiserslautern, 2020.

Y. Dong, Untersuchung thermisch verbesserter Polymerkomposite. Bachelorarbeit, Kaiserslautern, 2020.

M. Lorenz, Charakterisierung von Topographie und Benetzungseigenschaften thermisch verbesserter Polymerkomposite. Forschungsarbeit, Kaiserslautern, 2020.

R. Raab, Numerische Strömungssimulation eines Kondensationsvorgangs von Wasserdampf in Ansys Fluent. Forschungsarbeit, Kaiserslautern, 2020.

Y. Sari, Optimierung einer Anlage zur Bestimmung von Foulingkinetiken. Bachelorarbeit, Kaiserslautern, 2020.

T. Schröder, Experimentelle Untersuchung von Polymerkompositen hinsichtlich Oberflächengüte und Foulingneigung. Diplomarbeit, Kaiserslautern, 2019.

A.-K. Schwartzkopf, M. Usslar, T. Weber, Theoretische Betrachtungen eines Konzepts zur Wassergewinnung aus Meerwasser. Teamarbeit, Kaiserslautern, 2019.

Publications and presentations

List of publications

H. Kiepfer, P. Stannek, M. Grundler, H.-J. Bart, Development and thermal performance of a thermoplastic-graphite-composite based plate heat exchanger for use in corrosive media, Appl. Therm. Eng. (2023) 121581. 10.1016/j.applthermaleng.2023.121581.

H. Kiepfer, P. Stannek, M. Grundler, H.-J. Bart, Thermally conductive polypropylene composites as corrosion-resistant materials for plate heat exchangers, Polym. Compos. (2023). 10.1002/pc.27613.

H. Kiepfer, P. Stannek, M. Kuypers, M. Grundler, H.-J. Bart, The potential of thermally conductive polymer composites regarding crystallization fouling mitigation, Heat Mass Transfer (2023). 10.1007/s00231-023-03398-0.

H. Kiepfer; P. Stannek; M. Kuypers; M. Grundler; H.-J. Bart. Highly Conductive Thin-Walled Polypropylene/Graphite Composites as Heat Transfer Surfaces in Corrosive Media, in: HEFAT (Ed.), Proceedings of the 15th International Conference on Heat Transfer, Fluid Mechanics and Thermodynamics (HEFAT2021), 2021, pp. 1174–1179, ISBN: 978-1-77592-216-2.

H. Kiepfer, P. Sobolčiak, I. Krupa, H.-J. Bart, Polymeric Heat Exchangers in Seawater Desalination - Impact of Surface Charakteristics and Process Conditions on Cleanability, in: A.-Q. Zakaria (Ed.), Proceedings of the 9th Jordan International Chemical Engineering Conference, 2021, pp. 674–688, ISBN: 2020/3/1033.

P. Sobolčiak, A. Abdulgader, M. Mrlik, A. Popelka, A. A Abdala, A. A Aboukhlewa, M. Karkri, H. Kiepfer, H.-J. Bart, I. Krupa, Thermally Conductive Polyethylene/Expanded Graphite Composites as Heat Transfer Surface: Mechanical, Thermo-Physical and Surface Behavior, Polymers 12 (2020).

H. Kiepfer, W. Omar, T. Schröder, H.-J. Bart, Polymer Film Heat Transfer Surfaces in Seawater Desalination: Fouling Layer Formation and Technology, Chem. Eng. Technol. 43 (2020) 1205–1213.

D. Bellaire, H. Kiepfer, K. Münnemann, H. Hasse, PFG-NMR and MD Simulation Study of Self-Diffusion Coefficients of Binary and Ternary Mixtures Containing Cyclohexane, Ethanol, Acetone, and Toluene, J. Chem. Eng. Data 65 (2020) 793–803.

A. Ataki, H. Kiepfer, H.-J. Bart, Investigations on crystallization fouling on PEEK films used as heat transfer surfaces: experimental results, Heat Mass Transfer 56 (2020) 1443–1452.

List of presentations

H. Kiepfer; H.-J. Bart; P. Stannek; M. Kuypers; M. Grundler, The potential of thermally conductive polymer composites regarding crystallization fouling mitigation, Heat Exchanger Fouling and Cleaning Conference XIV (HEFC), 05.06.-10.06.2022, Wagrain, Austria.

H. Kiepfer; H.-J. Bart; P. Sobolciak; I. Krupa, Polymeric Heat Exchangers in Seawater Desalination – Impact of Surface Characteristics and Process Conditions on Cleanability, The Hybrid 9th Jordan International Chemical Engineering Conference (JIChEC09), 12.-14.10.2021, Amman, Jordan.

H. Kiepfer; H.-J. Bart; P. Stannek; M. Kuypers; M. Grundler, Highly Conductive Thin-Walled Polypropylene/Graphit Composites as Heat Transfer Surfaces in Corrosive Media, 15th International Conference on Heat Transfer, Fluid Mechanics and Thermodynamics (HEFAT), 25.-28.07.2021, Virtual Conference.

H. Kiepfer; H.-J. Bart, Thermisch leitfähige Polypropylen/Graphit Komposite als Wärmeübertragungsfläche in korrosiven Medien, Jahrestreffen der ProcessNet Fachgruppen Fluidverfahrenstechnik und Wärme- und Stoffübertragung, 24.-26.02.2021, Online-Event.

H. Kiepfer; H.-J. Bart, Kristallisationsfouling auf polymeren Oberflächen, 29. Außerordentliches Seminar, 09.-16.02.2019, Sulden, Italy.

List of posters

H. Kiepfer; P. Stannek; M. Grundler; H.-J. Bart, Polymer composite plate heat exchangers for application in corrosive environments, Annual Meeting on Reaction Engineering and ProcessNet Subject Division Heat and Mass Transfer 2022, 18.07.2022, Würzburg, Germany.

H. Kiepfer, H.-J. Bart, Milchprotein-Fouling auf PEEK als Wärmeübertragungsfläche: Belagbildung und Reinigbarkeit, Chemie Ingenieur Technik 92 (2020) 1323–1324.

Curriculum vitae

Professional experience

2023-Present	Moehwald GmbH Development engineer for fuel cell testing technology
2018-2022	Rheinland-Pfälzische Technische Universität Kaiserslautern-Landau Research associate & PhD student at Chair of Separation Science and Technology (Prof. Dipl.-Ing. Dr. techn. Hans-Jörg Bart); from 2021 Laboratory of Reaction and Fluid Process Engineering (Prof. Dr. Ing. Erik von Harbou)

Education

2016-2018	Technische Universität Kaiserslautern M.Sc. degree in Bio- und Chemieingenieurwissenschaften
2012-2016	Technische Universität Kaiserslautern B.Sc. degree in Bio- und Chemieingenieurwissenschaften